

The Thermal Transition of Quantum Chromodynamics with Twisted Mass Fermions

Dissertation
zur Erlangung des Doktorgrades
der Naturwissenschaften

vorgelegt beim Fachbereich Physik
der Johann Wolfgang Goethe-Universität
in Frankfurt am Main

von
Lars Zeidlewicz
aus Rheine

Frankfurt 2011
(D30)

vom Fachbereich Physik der
Johann Wolfgang Goethe-Universität als Dissertation angenommen.

Dekan: Professor Dr. M. Huth

Gutachter: Prof. Dr. O. Philipsen
Prof. Dr. G. Münster (Universität Münster)

Datum der Disputation: 01.07.2011

Zusammenfassung

Quantenchromodynamik (QCD) ist die etablierte Theorie zur Beschreibung der starken Wechselwirkung zwischen den Konstituenten der hadronischen Materie. Die elementaren Freiheitsgrade in der QCD-Wirkung sind dabei Quarks und Gluonen. Die Existenz der Quarks wurde erstmals von Gell-Mann und Zweig in den 1960er Jahren postuliert. In diesem Zusammenhang beschreibt der Begriff *confinement* die Erfahrungstatsache, dass freie Quarks nicht beobachtet werden.

Bei der QCD handelt es sich um eine nicht-Abel'sche Eichtheorie bzgl. der Gruppe $SU(3)$ und der zugehörigen Farbladung. Das bedeutet, dass die QCD eine lokale Eichinvarianz unter $SU(3)$ -Farbtransformationen aufweist. Insofern lässt sich *confinement* auch so formulieren, dass nur Farbsingulett-Zustände beobachtbar sind. Ein wesentliches Merkmal der QCD ist die asymptotische Freiheit, d.h. das Verschwinden der Kopplungsstärke, α_s , für wachsende Impulsüberträge bzw. Energieskalen,

$$\alpha_s(Q^2 \rightarrow \infty) \rightarrow 0 .$$

In Umkehrung dieser Beziehung wächst die Kopplung für große Abstände stark an, so dass eine perturbative Beschreibung auf Basis der ursprünglichen Freiheitsgrade zusammenbricht, was letztlich Voraussetzung für das Auftreten von *confinement* ist.

Während gerade der störungstheoretische Zugang bei sehr hohen Energien erfolgreiche Tests der Theorie gegenüber Experimenten an Teilchenbeschleunigern erlaubt, sind weite Energiebereiche nicht perturbativ zugänglich. Dies trifft neben der Vorhersage des Hadronspektrums insbesondere auf die Untersuchung des thermischen Übergangs, d. h. des Übergangs von der hadronischen Phase in ein stark wechselwirkendes Plasma, und der Materieeigenschaften oberhalb dieses Übergangs zu. Dieser Bereich des QCD-Phasendiagramms wird durch Schwerionenkollisionsexperimente an modernen Teilchenbeschleunigern (RHIC, LHC) untersucht. In den Schwerionenkollisionen entsteht Materie sehr hoher Energiedichte, die dann in einen thermalisierten Zustand oberhalb des thermischen Übergangs mündet. Während bei tieferen Temperaturen die beobachteten Hadronen — Mesonen (wie z. B. Pionen und Kaonen) und Baryonen (z. B. Protonen und Neutronen) — die relevanten Freiheitsgrade bilden, ist dies oberhalb des Übergangs nicht mehr der Fall. Dort interagieren die ursprünglich in der Wirkung auftretenden Quarks und Gluonen als Teilchen in einem stark gekoppelten Plasma. Tatsächlich hat sich gezeigt, dass dieses Quark-Gluon-Plasma (QGP) zumindest in der Nähe des thermischen Übergangs durch ideale Hydrodynamik beschrieben werden kann. Das tatsächliche Aufbrechen der Beschreibung hin zu wirklich freien Teilchen wird erst bei sehr viel höheren Temperaturen als Folge der asymptotischen Freiheit erwartet.

Durch die Einführung der Gitterregularisierung durch Wilson 1974 wurde eine Möglichkeit geschaffen, jenseits der Störungstheorie die QCD nicht-perturbativ zu untersuchen. Dazu werden die Minkowski-Raumzeit durch Wick-Rotation in eine Euklid'sche Metrik überführt und das kontinuierliche Raumzeitvolumen durch ein vierdimensionales hyperkubisches Gitter mit Gitterabstand a ersetzt. Diese Regularisierung der Theorie

mit einem Abschneiden der Impulse bei $1/a$ bricht die Lorentz-Invarianz und führt zu einer komplizierten Behandlung in Störungstheorie. Der eigentliche Grund, die Gitterformulierung der QCD zu verwenden besteht vielmehr darin, dass für endliches Volumen numerische Berechnungen unter Zuhilfenahme von leistungsfähigen Computern bzw. Großrechnern durchgeführt werden können. Der dabei typischerweise verwendete hybride Monte-Carlo Algorithmus erzeugt eine Markov-Kette von Eichfeldkonfigurationen, die gegen die entsprechende Gleichgewichtsverteilung konvergieren. Derart lassen sich statistische Mittelwerte für primäre Observablen, die als Funktion des Eichfeldes aufgefasst werden können, bestimmen.

Auf diese Weise werden im Rahmen der Gitter-QCD, bzw. allgemeiner in Gittereichtheorie, Vakuumenerwartungswerte und auch thermische Gleichgewichtserwartungswerte berechnet. In thermischen Systemen wird über die Länge der (Euklid'schen) Zeitrichtung mit N_τ Gitterpunkten eine Temperatur eingestellt, d. h. $T = 1/(aN_\tau)$. Dabei sind die entsprechenden Randbedingungen der Felder in Zeitrichtung zu beachten.

Während die Diskretisierung der reinen Eichtheorie keine weiteren konzeptionellen Probleme aufweist, ist die Situation für Fermionen wesentlich komplizierter. Eine naive Diskretisierung der fermionischen Ableitungsterme führt dazu, dass sich die Anzahl der Freiheitsgrade im Kontinuumslimit für jede Raumdimension verdoppelt. Diesem Dopplerproblem wird durch verschiedene Methoden der Fermiondiskretisierung entgegen getreten, die jeweils andere Vor- und Nachteile besitzen.

Gegenstand dieser Dissertation ist die Anwendung einer speziellen Variante gitterregularisierter Fermionen mit sogenanntem chiraler verdrehtem Massenterm (*twisted mass*) für Studien der thermischen Eigenschaften der Quantenchromodynamik. Während diese Fermionen zur Berechnung von Vakuumeigenschaften der QCD bereits erfolgreich durch die *European Twisted Mass Collaboration* (ETMC) eingesetzt worden sind, ist die erstmalige Anwendung auf physikalische Fragestellungen bei endlichen Temperaturen in dieser Arbeit enthalten. Neben konkreten physikalischen Problemen geht es also insbesondere darum, die spezifischen Eigenschaften der *twisted mass*-Formulierung jenseits des Vakuums zu untersuchen und ein Simulationskonzept zu erstellen.

Dabei liegt der Fokus im Wesentlichen auf der einfachsten Formulierung der *twisted mass* QCD (tmQCD), die ein massenentartetes leichtes Quarkdublett berücksichtigt. Dies ist der natürliche Anfangspunkt für Untersuchungen mit *twisted mass* Fermionen, da diese Fermiondiskretisierung auf Basis solcher *flavour*-Dubletts konstruiert wird. Die Grundlage für die Massenverdrehung bilden Gitterfermionen vom Wilson-Typ. Dieser Typus vermeidet das Dopplerproblem, indem die chirale Symmetrie durch einen zusätzlichen Term in der Wirkung explizit gebrochen wird. Dies führt neben einer additiven Massenrenormierung insbesondere dazu, dass Gitterartefakte bereits in einer Ordnung früher als bei anderen Fermionen auftauchen, d. h. in $\mathcal{O}(a)$. Derartige Probleme haben andere Arten der Fermiondiskretisierung nicht. Insbesondere *staggered* Fermionen sind sehr oft für thermische Studien verwendet worden. Allerdings ist die Gültigkeit der *staggered* Fermionformulierung jenseits der Störungstheorie umstritten, so dass weitestgehend anerkannt ist, dass die *staggered*-Ergebnisse durch Untersuchungen mit alternativen Fermiontypen kontrolliert werden müssen.

Die Modifikation der Wilson'schen Fermionen durch den chiralen verdrehten Massenterm erlaubt nun, zumindest die führende Ordnung der Diskretisierungsartefakte wieder zu $\mathcal{O}(a^2)$ zu korrigieren, wenn man den unverdrehten Anteil der Quarkmasse zu Null einstellt. Diese spezielle Wahl, die letztlich zu einer Verdrehung um $\pi/2$ korrespondiert,

bezeichnet man üblicherweise als maximale Verdrehung bzw. *maximal twist*. Maximal verdrehte Wilson-Fermionen bilden damit — neben den auch benutzten *clover* Fermionen — eine vielversprechende Wahl für die Anwendung auf thermische Systeme, die typischerweise stark durch Diskretisierungseffekte beeinträchtigt sind.

Diese Dissertation ist wie folgt strukturiert. Die bisherigen einleitenden Erläuterungen entsprechen den Kapiteln 1 bis 3, wobei dort natürlich in weit größerem Maße auf die theoretischen Grundlagen eingegangen wird. Dies schließt insbesondere die Diskussion der laufenden Kopplung und chiraler Symmetrien in Kapitel 2 ein. Bei den Erläuterungen der Gitter-QCD wird insbesondere die tmQCD mit ihren besonderen Eigenschaften betrachtet. Neben der automatischen $\mathcal{O}(a)$ -Verbesserung bei maximalem *twist* umfasst dies auch die ETMC-Untersuchungen zu der nicht-trivialen Vakuumstruktur im Raum der unrenormierten Parameter κ , β und μ_0 . $\kappa = (2am_0 + 8)^{-1}$ ist dabei der Hoppingparameter, $\beta = 6/g^2$ die Gitterkopplung und μ_0 der *twisted mass*-Parameter.

In Kapitel 4 werden anschließend einige generelle Eigenschaften der tmQCD bei nicht-verschwindender Temperatur behandelt. Dies betrifft zum einen die zuvor genannte Phasenraumstruktur. Bei endlichen Temperaturen kommt als neues Element der thermische Übergang hinzu. Tatsächlich konnten wir basierend auf einer Vermutung von Creutz den thermischen Übergang als Fläche im Phasendiagramm ausmachen, die sich kegelartig um den kritischen Hoppingparameter windet und zu größeren Temperaturen — sprich β — immer größer wird. Die entsprechenden Simulationen wurden vor dieser Dissertation begonnen. Allerdings machen wir deutlich, welche wesentlichen Aspekte tatsächlich Teil dieser Arbeit sind. Alles in allem ist es wichtig anzumerken, dass die unphysikalischen Phasen verstanden sind und für den eigentlich interessanten Kontinuumsimes kein bedeutendes Hindernis darstellen.

Der zweite Zugang, der in Kapitel 4 verfolgt wird, besteht in störungstheoretischen Berechnungen des Drucks. Hierbei extrahieren wir die Abhängigkeit von den führenden Ordnungen in a explizit für den freien Druck und finden, dass sich die verschiedenen Diskretisierungen im a^2 -Skalierungsbereich nicht stark unterscheiden. Allerdings bleibt festzuhalten, dass a^2 -Verhalten nicht vor $N_\tau \sim 10$ beobachtet wird. Qualitativ gleiche Schlussfolgerungen lassen sich auch aus der nächsten Ordnung, den Zweischleifendiagrammen, ziehen.

Kapitel 5 enthält unsere Untersuchung des $N_f = 2$ thermischen Übergangs. N_f bezeichnet hierbei die Anzahl der Quark-Arten bzw. *flavours*. Während sowohl für den $N_f = 3$ chiralen Limes als auch für die reine Eichtheorie klar ist, dass der thermische Übergang ein echter Phasenübergang erster Ordnung ist, bleibt die Situation für den thermischen Übergang im chiralen Limes zweier Quark-Arten unklar. Es gibt zwei mögliche Szenarien, die von Pisarski und Wilczek identifiziert wurden. Das erste Szenario sieht einen Übergang zweiter Ordnung im chiralen Limes vor. Dieser würde in der dreidimensionalen $O(4)$ -Universalitätsklasse liegen. Die zweite Möglichkeit ist ein Übergang erster Ordnung gerade so wie in den zuvor genannten zwei anderen Grenzfällen. Entscheidend ist hier die Stärke der $U_A(1)$ -Anomalie, die stark genug durch thermische Effekte unterdrückt sein muss, damit es zu einem Übergang erster Ordnung kommen kann.

Im ersten Teil von Kapitel 5 präsentieren wir unsere Simulationsläufe. Dabei handelt es sich um Läufe mit verschiedenen Werten der Gitterkopplung β bei konstanter Pionmasse und maximaler chiraler Verdrehung. Durch die Veränderung von β verändern wir über den Gitterabstand letztlich die Temperatur $T = 1/(aN_\tau)$. Für die Analyse relevant

sind vier Datensätze bei drei verschiedenen Pionmassen, $300 \text{ MeV} \leq m_\pi \leq 500 \text{ MeV}$. Viel kleinere Massen, womöglich sogar die physikalische Pionmasse, sind mit Fermionen vom Wilson-Typ derzeit nicht zu erreichen. Die einzelnen Datensätze werden von uns mit A12, B10, B12 und C12 benannt; die Zahl gibt die Anzahl der Gitterpunkte in Zeitrichtung N_τ an, so dass bei physikalisch konstanten Bedingungen größere N_τ in den Kontinuumsmlimes führen. Die Pionmassen sind im Einzelnen $316(16) \text{ MeV}$ (A12), $398(20) \text{ MeV}$ (B10, B12) und $469(24) \text{ MeV}$ (C12). Die Ausdehnung des Gitters in die räumlichen Richtungen beträgt in allen Fällen $L = aN_\sigma$ mit $N_\sigma = 32$ Gitterpunkten.

Für die mittlere Masse gibt es zwei Gitterabstände, so dass sich die Größe der Diskretisierungseffekte abschätzen lässt. Es zeigt sich, dass diese klein sind im Vergleich zu den Unsicherheiten, die durch Statistik und Skalensetzung auftreten.

Um den Gitterabstand und die Pionmasse für unsere Simulationsläufe zu bestimmen sowie um den kritischen Hoppingparameter als Bedingung für maximalen *twist* einzustellen, haben wir auf die Daten zurückgegriffen, die ETMC publiziert hat. Basierend auf den β -Werten von ETMC, $\beta \in \{3.8, 3.9, 4.05, 4.2\}$, können wir so die für uns interessanten Größen zuverlässig interpolieren.

Die betrachteten Observablen sind das chirale Kondensat, die Plakette und der Polyakov-*loop* (Wilson-Linie). Letzterer ist in der reinen Eichtheorie der Ordnungsparameter für den Phasenübergang von *confinement* zu *deconfinement*. Von weiterem besonderen Interesse ist das chirale Kondensat, das im Grenzfall masseloser Quarks den Ordnungsparameter des chiralen Phasenübergangs darstellt.

Die Kategorisierung der verschiedenen Möglichkeiten von Phasenübergängen zweiter Ordnung in Universalitätsklassen erfolgt nach Spinmodellen. Im chiralen Limes der zwei-*flavour*-Theorie könnte die dreidimensionale $O(4)$ -Universalität vorliegen, wenn die Anomalie genügend stark ist. Andererseits könnte es zum Phasenübergang erster Ordnung kommen, der sich zu endlichen Quarkmassen erstrecken würde. Dann müsste ein Endpunkt zweiter Ordnung in der 3d-Ising Universalitätsklasse existieren. Da unsere Simulationen deutliches Verhalten eines analytischen Überganges aufweisen, erwartet man folglich für die Annäherung an den chiralen Limes entweder $O(4)$ - oder $Z(2)$ - (Ising) Verhalten, wobei der $Z(2)$ -Punkt bei endlicher Pionmasse zu finden wäre.

Diese Beobachtung der Universalitätsklasse macht sich zu Nutze, dass Skalenverhalten schon in einem kritischen Bereich um den eigentlichen Übergangspunkt vorherrschend ist. Die erste von uns angewandte Extrapolationsmethode basiert auf dem Verhalten der pseudokritischen Temperatur als Funktion der Pionmasse,

$$T_c(m_\pi) = T_c(0) + A(m_\pi)^{2/(\beta\delta)},$$

wobei β und δ die für die Universalitätsklasse charakteristischen kritischen Exponenten sind. Ein Fit mit freien Exponenten erweist sich als nicht aussagekräftig. Tatsächlich sind die Exponenten zu nah bei einander, um die verschiedenen Szenarien zu trennen. Allerdings finden wir aufgrund der Größe der extrapolierten Temperatur im Vergleich zu anderen existierenden Untersuchungen eine leichte Präferenz für $O(4)$ -Verhalten. Zu beachten ist, dass das Quadrat der Pionmasse als Argument die Quarkmasse ersetzt, die dem eigentlichen symmetriebrechenden äußeren Feld entspricht. Die verwendete Beziehung, $m_\pi^2 \sim m_q$, stellt allerdings nur die führende Ordnung in der sogenannten chiralen Störungstheorie dar, weshalb die Gültigkeit der obigen Formel für Massen $m_\pi \gtrsim 500 \text{ MeV}$ nicht erwartet werden kann. Dies begründet insbesondere unsere Wahl der oberen Grenze der betrachteten Pionmassen.

Eine zweite Möglichkeit, Skalenverhalten zu untersuchen, ist die magnetische Zustandsgleichung,

$$\langle \bar{\psi}\psi \rangle = h^{1/\delta} f(x) ,$$

mit der Skalenvariablen $x = (\beta - \beta_{\text{chiral}})/h^{1/(\delta\beta)}$, wobei der kritische Exponent von der Gitterkopplung im Zähler zu unterscheiden ist. Die obige Gleichung setzt den Ordnungsparameter, das chirale Kondensat, mit einer Skalenfunktion in Verbindung, die für $O(4)$ bekannt ist. Das die Symmetrie explizit brechende äußere Feld ist hier wiederum durch die Quarkmasse gegeben, die aber nicht wie zuvor durch die Pionmasse ersetzt wird. Insgesamt erlaubt die magnetische Zustandsgleichung die Betrachtung etwas größerer Temperaturbereiche und ist nicht unmittelbar auf die Bestimmung der pseudokritischen Temperatur bei gegebener Pionmasse angewiesen.

Wir stellen fest, dass wir die beiden leichteren Massen durch die magnetische Zustandsgleichung unter Zuhilfenahme führender Skalenverletzungen für $O(4)$ -Verhalten beschreiben können. Aufgrund der Ähnlichkeit der Exponenten führt dies aber keineswegs zu einem Ausschluss der anderen möglichen Szenarien. Jedoch können wir feststellen, dass wir ein selbstkonsistentes Bild mit $O(4)$ -Verhalten im chiralen Limes erhalten.

Einen direkten Zugang, die Stärke der Anomalie zu untersuchen, bieten sogenannte *screening*-Massen. Diese schirmen Mediuamanregungen mit entsprechenden Quantenzahlen räumlich ab. Neben den Massen bietet es sich auch an, das Integral über die Korrelatoren, aus denen die Massen bestimmt werden, zu betrachten, da hier ohne die Notwendigkeit eines Fits weniger systematische Effekte auftreten können. Tatsächlich zeigt sich, dass wir auf dieses Vorgehen angewiesen sind, da auf Basis der uns zur Verfügung stehenden Datenmenge die *screening*-Massen selbst nicht genau genug bestimmt werden können. Wir verwenden die Korrelatoren, die den geladenen *flavour*-Multipllett-Teilchen entsprechen. Dies erleichtert die Auswertung, da keine unverbundenen Beiträge vorkommen, die sehr stark durch numerisches Rauschen beeinträchtigt sind.

Neben der Analyse auf Grundlage der in unseren o. g. Simulationen erzeugten Eichfeldkonfigurationen betrachten wir außerdem den freien Limes der Theorie. In diesem Grenzfall lassen sich Diskretisierungs- und Volumeneffekte untersuchen. Zumindest für diese Theorie ohne Wechselwirkungen finden wir, dass Korrekturen durch den Gitterabstand die Massen verringern, während Volumeneffekte zu einer Vergrößerung führen.

Die Aufspaltung der pseudoskalaren und skalaren *screening*-Observablen ist ein Maß für die Anomalie, da es sich um Partner unter Transformationen der $U_A(1)$ handelt. Zum chiralen Limes hin beobachten wir sogar eine anwachsende Stärke der Anomalie, was wiederum auf das $O(4)$ -Szenario hinweist, ohne dass letztgültige Schlüsse gezogen werden könnten, da keine absolute Skala für die Anomaliestärke zur Verfügung steht.

In Kapitel 6 diskutieren wir die Erweiterung auf den Fall $N_f = 2 + 1 + 1$, d. h. die Berücksichtigung von dynamischen *strange* und *charm* Quarks. Dies ist von theoretischer Seite kein Problem, da sich ein massenaufspaltender Term in die tmQCD-Wirkung integrieren lässt. Gerade das *strange* Quark hat eine Masse im Bereich der Übergangstemperatur, so dass man generell einen starken Einfluss vermuten kann. Wir betrachten wiederum den freien Druck, für den wir die freie, in diesem Fall allerdings aufgespaltene Dispersionsrelation in Ordnungen des Gitterabstandes entwickeln. Die zusätzlichen Gitterartefakte durch die Aufspaltung erweisen sich als sehr klein.

Letztlich geben wir mögliche Parameterwerte für einen ersten Simulationslauf im $N_f = 2 + 1 + 1$ Rahmen an. Aufgrund der Erfahrung für $N_f = 2$ und basierend auf

den Daten, die bereits von ETMC publiziert worden sind, ist die Wahl eines vielversprechenden Bereichs möglich.

Zusammenfassung und Ausblick geben wir in Kapitel 7. Diese Dissertation stellt die erste Anwendung von gitterregularisierten Fermionen mit chiral verdrehtem Massenterm auf physikalische Fragestellungen im Rahmen der thermischen QCD dar. Unsere Untersuchungen liefern erste Ergebnisse, die untermauern, dass die tmQCD einen vielversprechenden Ansatz für diese Art physikalischer Probleme zur Verfügung stellt. Darüber hinaus erlauben die hier vorgestellten Resultate die Vertiefung und Erweiterung der bisherigen Studien in zukünftigen Projekten.

Angeführt sind noch einige Anhänge, in denen wir zusätzliche Informationen zur verwendeten Notation (A) und Details für Rechnungen im Grenzfall der freien Theorie (C) sowie Simulationsdetails (B, D) sammeln.

Contents

1. Introduction	1
2. Quantum Chromodynamics in the Continuum	5
2.1. QCD and the Standard Model	5
2.1.1. Action of QCD	6
2.1.2. Running Coupling	7
2.2. Chiral Symmetry	8
2.3. Thermal Systems	11
2.3.1. Thermal Field Theory	11
2.3.2. Heavy Ion Collisions and the Quark-Gluon-Plasma	13
3. Quantum Chromodynamics on the Lattice	15
3.1. Lattice Gauge Theory	16
3.2. Wilson Fermions	18
3.3. Twisted Mass Fermions	20
3.3.1. Twisted Mass Formulation	20
3.3.2. Automatic Improvement	21
3.3.3. Phase Diagram	23
3.4. Alternative Fermion Discretisations	25
3.5. Numerical Simulations	26
3.5.1. Hybrid Monte-Carlo	27
3.5.2. Data Analysis	28
4. Properties of Twisted Mass QCD at Finite Temperature	31
4.1. Phase Diagram	31
4.1.1. Theoretical Expectations	31
4.1.2. Comparison to Simulations	32
4.2. Weak Coupling Limit	34
4.2.1. Ideal Gas	35
4.2.2. Two-loop Contribution	38
5. Thermal Transition for Two Quark Flavours	41
5.1. Scaling Properties	42
5.2. Observables	44
5.2.1. Chiral Condensate	44
5.2.2. Gauge Observables	46
5.3. Simulations	47
5.3.1. Setup	48
5.3.2. Signal Extraction	49
5.4. Transition in the Chiral Limit	53

5.5. Strength of the Anomaly	57
5.5.1. Screening Correlators	57
5.5.2. Free Screening Masses	59
5.5.3. Large Mass Regime	62
5.5.4. Towards the Chiral Limit	63
5.6. Summary and Discussion	67
6. Including Strange and Charm Quarks	69
6.1. Twisted Mass Action with Four Flavours	69
6.2. Four Flavours at Finite Temperature	70
6.2.1. Cutoff Effects for the Non-Interacting Pressure	70
6.2.2. Simulation Setup	72
7. Conclusions and Research Perspectives	75
A. Notations and Conventions	79
A.1. Natural Units	79
A.2. Dirac Matrices and Euclidean Spacetime	79
B. Thermal Transitions in the Bare Phase Diagram	81
C. Calculations in the Non-Interacting Limit	83
C.1. Integrals for the Free Pressure	83
C.2. Free Lattice Screening Masses	85
D. Simulation Details	89
D.1. Interpolation of κ_c	89
D.2. Monte-Carlo Data	89
D.3. Gaussian Fits	93
D.3.1. Run A12	93
D.3.2. Run B10	94
D.3.3. Run B12	94
D.3.4. Run C12	95
D.4. Results of Screening Mass Fits	97
D.4.1. Run A12	97
D.4.2. Run B10	98
D.4.3. Run B12	98
D.4.4. Run C12	98
Bibliography	99
Danksagung	113
Lebenslauf	115

1. Introduction

Since the rapid development of quantum field theories in the 1960's and 1970's and the discovery of asymptotic freedom in 1973 [1, 2] quantum chromodynamics (QCD) has been established as the theory of strong interaction. The main source of confidence for the validity of QCD is the high energy regime in which collider experiments can be compared to perturbative calculations. The outcome of these experiments can be described to very high accuracy by QCD together with the electroweak theory forming the so-called Standard Model of particle physics; for a collection of those results see e. g. [3].

For lower energies perturbation theory is not applicable due to the increasing coupling strength. This prohibits, for instance, perturbative calculations of hadron masses. The coupling as a function of temperature is already too large for temperature scales that are relevant to studies of thermal QCD systems. Moreover, perturbation theory at finite temperature beyond the leading orders is in general obstructed by infrared divergences. This phenomenon is known as the Linde problem [4]. Thermodynamics of strongly interacting matter is experimentally studied at the colliders RHIC ¹ and LHC ². The heavy ion collisions at those colliders are meant to produce a very hot state of matter in which quarks and gluons are at least partially deconfined, the so-called quark-gluon plasma (QGP). Of course, since the evolution of the universe is a history of decreasing temperature, at some early stage the QCD transition from a QGP-like state to the hadronic phase as we observe it in today's universe must have occurred and thus knowledge about that transition is important for cosmology. A second family of experiments, especially FAIR at GSI ³, addresses matter with higher density. This regime, too, is not accessible for perturbation theory. Model studies suggest a phase structure similar to the one depicted in figure 1.1, which is based on the review in [5].

Lattice gauge theory was introduced in the 1970s and early 1980s as a tool that allows to investigate QCD non-perturbatively by numerical means [6, 7, 8, 9]. This applies to both zero and non-vanishing temperature but is restricted to small baryon density or equivalently small chemical potential. The latter is the more appropriate quantity in terms of the grand canonical partition function usually used in lattice QCD. The restriction is due to the so far unsolved sign-problem, see e. g. [10]. This thesis focuses on the first application of a particular formulation of lattice fermions with a so-called chirally twisted mass term to simulations addressing questions of finite temperature QCD. Twisted mass fermions overcome some problems of ordinary (unimproved) Wilson fermions and offer a theoretically sound continuum limit. We demonstrate that twisted mass fermions are well applicable to study thermal problems.

The physical object of interest for this work is the thermal transition itself. The transition between the deconfined and confined phase is, as explained above, under in-

¹See the RHIC website, www.bnl.gov/rhic .

²See the LHC website, lhc.web.cern.ch/lhc .

³See the FAIR portrait on the GSI homepage, <http://www.gsi.de/portrait/fair.html> .

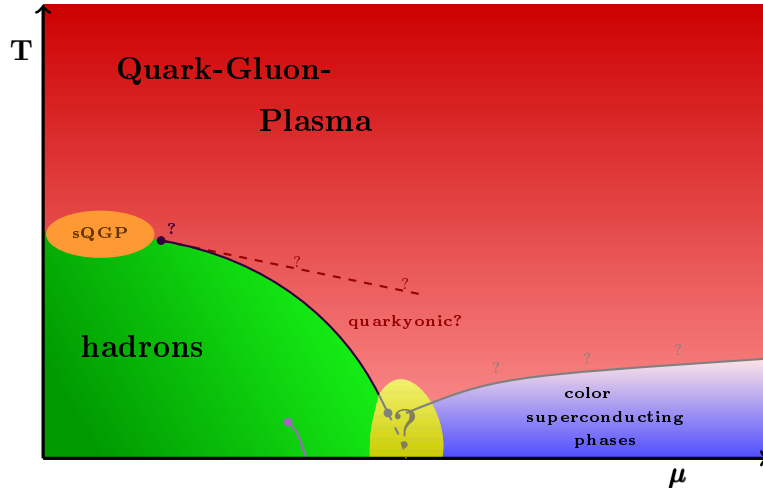


Figure 1.1.: Conjectured phase diagram of QCD. The axis of vanishing chemical potential is accessible by non-perturbative lattice simulations. Most features of the phase structure are expected from model studies. This visualisation is based on the review by Fukushima and Hatsuda [5].

investigation in modern collider experiments. Its apparent entanglement with chiral symmetry breaking poses further questions to theoretical research. The thermal transition has been studied in lattice simulations utilising different types of fermion discretisations, the most detailed studies relying on the staggered fermion formulation by Kogut and Susskind [11] as well as improved versions thereof. Exhaustive reviews can be found in the proceedings of the annual Lattice conferences, e. g. [12]. Various attempts to go to finite chemical potential based on different techniques have been made and are currently being pursued [10, 13]. Whereas in principle those methods are applicable to twisted mass fermions as well as to any other fermion discretisation, this thesis is only concerned with vanishing chemical potential pioneering the use of twisted mass fermions at finite temperature.

Particularly important is to know the nature of the phase transition depending on the quark mass. That is because computational cost varies with a negative exponent for the quark mass and for a long time the point of physical quark masses has only been accessible by extrapolations [14]. For Wilson type fermions physical quark masses are still beyond reach for practical purposes whereas staggered fermions are a lot cheaper in terms of computing time. However, the computational advantage of staggered fermions comes with an on-going dispute about their validity [15, 16].

The current understanding of the nature of the phase transition in the plane spanned by the mass of up and down quarks m_{ud} — taken to be degenerate — and the strange quark mass m_s is sketched in figure 1.2 in the popular way. It has been demonstrated that the transition at the physical point is really an analytical crossover [17, 18] that takes place in a temperature interval $T \sim 150 - 200$ MeV [19, 20, 21]. On the other hand, the temperature of the first order transition for infinite quark masses, i. e. in pure SU(3) gauge theory, is about 280 MeV [22]. We give more details with focus on the two-flavour limit later when discussing our results in chapter 5.

Twisted mass fermions have been used successfully by the European Twisted Mass

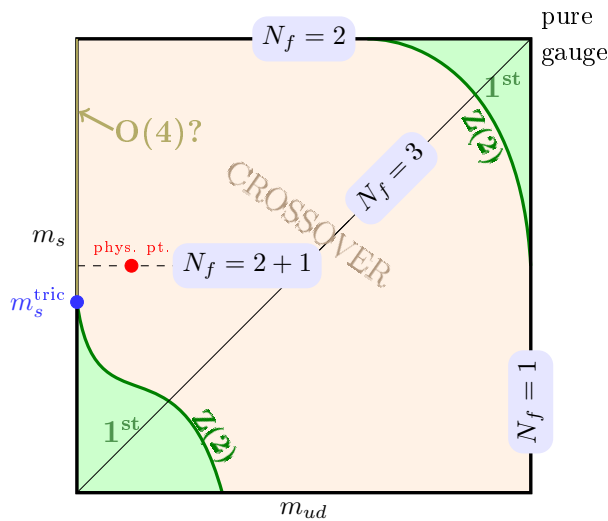


Figure 1.2.: The nature of the phase transition in the $m_{ud} - m_s$ plane as it is often shown in reviews, see e. g. [12]. The upper right corner corresponds to $SU(3)$ pure gauge theory with a first order deconfinement transition. The massless limit in the lower left corner exhibits the first order transition due to chiral symmetry breaking. The situation for the two flavour chiral limit, i. e. the upper left corner, is not completely clear. One possibility is shown in the plot with the second order transition of the 3d $O(4)$ universality class that extends down to some tricritical strange quark mass. But also a first order transition with a $Z(2)$ boundary as in the two previously mentioned cases is not ruled out.

Collaboration (ETMC) to calculate vacuum properties of QCD such as hadron masses or decay constants [23, 24]. Application of these fermions to finite temperature systems has been pursued by the twisted mass finite temperature (tmfT) collaboration [25, 26, 27, 28, 29, 30] as part of which the work for this thesis has predominantly been performed. The properties of twisted mass fermions at finite temperature and the physical results obtained and presented here can serve for further research relying on this particular type of fermions.

This thesis is structured as follows. The next chapter contains a presentation of Quantum Chromodynamics as a part of the Standard Model. This includes the continuum action, chiral symmetries and the treatment in thermal field theory. We also give a short overview about the relevant heavy ion collision experiments.

Chapter 3 is used to introduce the lattice discretisation of fermions and in particular Wilson type fermions with twisted mass term. The following chapter 4 continues the discussion of twisted mass QCD by presenting our studies of the non-trivial phase structure in bare parameter space [29] and of the perturbative properties of improvement [31].

Chapter 5 is devoted to simulations with two flavours of mass degenerate quarks. For this setup the nature of the transition in the chiral limit is still an open question that we discuss in the light of our results. We assess the potential of possible approaches to solve that question, viz. extrapolations of the pseudo-critical temperature as a function of pion mass and comparison of the chiral condensate to universal scaling. Moreover, we investigate the splitting in the spectrum of screening masses that gives indirect information on the nature of the transition by the strength of the axial anomaly. We

spend part of the chapter to discuss possible systematic errors in the determination of screening masses by looking at the infinite temperature limit.

In a short chapter 6, we consider the extension of twisted mass QCD to strange and charm quarks in the so-called $N_f = 2 + 1 + 1$ setup. Although so far no numerical simulations are available, we present some thoughts on possible strategies and the expected size of cutoff effects. Finally, conclusions are drawn and perspectives for future research are given in chapter 7.

2. Quantum Chromodynamics in the Continuum

This chapter serves to present Quantum Chromodynamics (QCD) as a quantum field theory in its continuum formulation. We begin in the following section by introducing the action of QCD, being part of the Standard Model. The crucial concept of chiral symmetry is then discussed in section 2.2. Section 2.3 contains the treatment of thermal QCD systems and is used to give a short overview about the heavy ion collider experiments complementing the theoretical study of hot nuclear matter.

For the basics of quantum field theory and the Standard Model, we refer to the textbook by Peskin and Schroeder [32], additional inspiration has been taken from [33]. Our presentation of thermal field theory is based on Kapusta's book [34].

2.1. QCD and the Standard Model

The Standard Model of elementary particle physics combines the strong, weak and electromagnetic interactions into the common framework of quantum field theory. The fourth fundamental interaction, gravity, stands apart because a comparable quantisation has not been accomplished up to the present.

The key concept that renders quantum field theory interacting is the principle of local gauge invariance. The gauge groups are characteristic for the particular type of interaction, i. e. $SU(3)$ for the strong interaction and $SU_w(2) \times U_Y(1)$ for the electroweak sector. The latter symmetry group is broken to the electromagnetic $U_{em}(1)$ allowing the W^\pm and Z bosons to be massive. It is hoped that the outcome of the current LHC experiments will shed light on the mechanism of this symmetry breaking, which can be described by introducing the so-far unobserved Higgs particle into the theory, cf. e. g. [35]. In the following, we concentrate on QCD which this thesis is concerned with.

An early stage in the development of QCD as theory of the strong interaction was the identification of quarks as constituents of hadronic matter by Gell-Mann [36] and Zweig [37] motivated by the classification of hadron multiplets that are at least approximately mass degenerate. The dynamical description of strong interaction is then obtained in terms of a Yang-Mills theory [38] with a gauge group $SU(N_c)$ for three so-called colour degrees of freedom, $N_c = 3$. Although Yang-Mills theories had been known since the 1950s, their true relevance only became clear due to the discovery of asymptotic freedom by Politzer [1], Gross and Wilczek [2]. Asymptotic freedom describes a decreasing interaction strength for large momentum transfer, i. e. on small length scales. Accordingly, interactions become stronger and stronger for large distances. This property of the non-Abelian Yang-Mills theory allows for confinement, i. e. the experimental fact that quarks are never observed as free particles.

2.1.1. Action of QCD

We begin the discussion of QCD by giving its action functional,

$$S[\bar{\psi}, \psi, A_\mu] = \int d^4x \left(\sum_f \bar{\psi}_f(x) (i\gamma^\mu D_\mu - m_f) \psi_f(x) - \frac{1}{4} F_{\mu\nu}^a(x) F^{a,\mu\nu}(x) \right). \quad (2.1)$$

In more detail, we can identify the integrand to consist of fermionic and pure gauge (Yang-Mills) Lagrangian densities,

$$\mathcal{L}_F = \sum_f \bar{\psi}_f(x) (i\gamma^\mu D_\mu - m_f) \psi_f(x), \quad (2.2a)$$

$$\mathcal{L}_{YM} = -\frac{1}{4} F_{\mu\nu}^a(x) F^{a,\mu\nu}(x). \quad (2.2b)$$

Concentrating on the fermionic part first, we see that the quarks as elementary fermions are expressed by the continuous spinor fields $\psi_f(x)$, one for each quark flavour f . The Dirac γ -matrices act in spinor space and have to fulfil

$$\{\gamma_\mu, \gamma_\nu\} = 2g_{\mu\nu}, \quad (2.3)$$

with the Minkowski metric $g_{\mu\nu}$. Note that the right hand side is really proportional to the unit matrix in spinor space on which also the Dirac matrices act. However, we follow the common convention and usually suppress the explicit appearance of such unit matrices in our formulae.

Interactions are mediated by the gluons which are described by means of the gauge fields $A_\mu^a(x)$, $a = 1, \dots, N_c^2 - 1$. The coupling appears in terms of the covariant derivative,

$$D_\mu = \partial_\mu - igA_\mu^a T^a. \quad (2.4)$$

The generators of $SU(N_c)$, T^a , form a Lie algebra with the proper commutation relations,

$$[T^a, T^b] = if^{abc} T^c. \quad (2.5)$$

The second part of the QCD action — corresponding to the Yang-Mills Lagrangian density given in equation (2.2b) — accounts for the pure gauge dynamics. The field strength $F_{\mu\nu}^a$ can be defined by the covariant derivative,

$$[D_\mu, D_\nu] = -igF_{\mu\nu}^a T^a. \quad (2.6)$$

Since the gauge group is non-Abelian, the Yang-Mills action contains three- and four-gluon self-interactions. This is the essential difference between the Abelian Quantum Electrodynamics and the non-Abelian QCD.

The spinor fields transform in the fundamental representation of colour $SU(3)$. The gauge fields, A_μ^a , ensure local gauge invariance through the covariant derivative and have to transform themselves in the adjoint representation of $SU(3)$. Correspondingly, the infinitesimal gauge transformations read

$$\psi(x) \rightarrow (1 + i\alpha^a(x)T^a)\psi(x), \quad (2.7a)$$

$$A_\mu^a(x) \rightarrow A_\mu^a(x) + \frac{1}{g}\partial_\mu\alpha^a(x) + f^{abc}A_\mu^b(x)\alpha_\mu^c(x), \quad (2.7b)$$

corresponding to a global transformation matrix $\exp(i\alpha^a(x)T^a) \in SU(3)$.

Once the action is given, the expectation value for some primary observable, K , can be expressed as a path integral, i. e. as an integral that is defined on the space of all possible field configurations,

$$\langle K \rangle = \frac{1}{Z} \int \mathcal{D}[\bar{\psi}, \psi, A_\mu] K[\bar{\psi}, \psi, A_\mu] e^{iS[\bar{\psi}, \psi, A_\mu]} , \quad (2.8)$$

with the normalisation given by

$$Z = \int \mathcal{D}[\bar{\psi}, \psi, A_\mu] e^{iS[\bar{\psi}, \psi, A_\mu]} . \quad (2.9)$$

For later purposes it is useful to note that the fermionic part of the action can be rewritten by means of a fermion kernel, the Dirac operator, M_F ,

$$S_F[\bar{\psi}, \psi, A_\mu] = \int d^4x \left(\sum_f \bar{\psi}_f(x) (i\gamma^\mu D_\mu - m_f) \psi_f(x) \right) =: (\psi, M_F[A_\mu] \psi) . \quad (2.10)$$

Since the fermionic path integral is quadratic in the fields, it can be evaluated explicitly, rendering

$$\int \mathcal{D}[\bar{\psi}, \psi] e^{i(\psi, M_F[A_\mu] \psi)} = \text{Det } M_F[A_\mu] . \quad (2.11)$$

2.1.2. Running Coupling

It is possible to perform perturbative QCD calculations for a small coupling strength $\alpha_s = g^2/(4\pi)$. However, one has to take into account the running of the coupling which is governed by the renormalisation group equation with respect to some renormalisation scale μ_R ,

$$\mu_R^2 \frac{d}{d\mu_R^2} \alpha_s = \beta(\alpha_s) , \quad (2.12)$$

where we use the notation as in the review on QCD by the Particle Data Group [39]. In this context, asymptotic freedom corresponds to a negative β -function. If Q^2 denotes the scale of momentum transfer in some process of interest, then $\alpha_s(\mu_R^2 \approx Q^2)$ determines the effective interaction strength and the negative β -function leads to a stable fixed point for $Q^2 \rightarrow \infty$,

$$\alpha_s(Q^2 \rightarrow \infty) = 0 . \quad (2.13)$$

In case of QCD with $N_c = 3$ and N_f fermions, the β -function to leading order,

$$\beta(\alpha_s) = -\frac{\alpha_s^2}{12\pi} (11N_c - 2N_f) , \quad (2.14)$$

ensures asymptotic freedom as long as $N_f < 17$. Solving equation (2.12) explicitly to leading order,

$$\alpha_s = \frac{1}{\frac{1}{6\pi} (11N_c - 2N_f) \ln(\mu_R/\Lambda)} , \quad (2.15)$$

the coupling approaches its asymptotic value logarithmically for large scales. On small scales, the divergence for $\mu_R/\Lambda \rightarrow 1$ indicates that the leading order approximation

becomes insufficient. The integration constant Λ introduces a typical scale into the theory, for QCD $\Lambda_{\text{QCD}} \approx 200 \text{ MeV}$ (see e. g. [32]).

In particular, $\alpha_s(M_Z^2) \sim 0.12$ with a Z boson mass $M_Z \approx 91 \text{ GeV}$ [39]. This already indicates that calculations of hadron masses and related quantities on much lower scales fall in the non-perturbative regime of QCD with couplings too large for an expansion in α_s to be valid and thus necessitating a non-perturbative approach as we pursue in this thesis by means of lattice QCD.

2.2. Chiral Symmetry

In this section, we discuss the chiral symmetries of QCD. The notion of chiral symmetry will be important for the later analyses in chapter 5. Our compilation concentrates on well established properties of QCD, an extensive review that goes far beyond the scope of this introduction was given by Gasser and Leutwyler [40]. Additionally, we continue to use the book by Peskin and Schroeder [32] as the standard reference. For the following, we consider the spinor fields ψ to be vectors in flavour space with $N_f = 2$ or 3 components, i. e. we concentrate on the light quarks — up, down and strange — relevant in this context.

Introducing left and right handed projection operators,

$$P_L = \frac{1}{2}(1 - \gamma_5) \quad \text{and} \quad P_R = \frac{1}{2}(1 + \gamma_5) , \quad (2.16)$$

we can rewrite the fermionic part of the QCD action from equation (2.1) for $\psi_L = P_L\psi$ and $\psi_R = P_R\psi$, obtaining a separation of ψ_L and ψ_R for massless fermions,

$$S_F[\bar{\psi}, \psi, A_\mu] = \int d^4x \left(\bar{\psi}_L(x) i\gamma^\mu D_\mu \psi_L(x) + \bar{\psi}_R(x) i\gamma^\mu D_\mu \psi_R(x) \right) . \quad (2.17)$$

The massless action possesses a global $SU_L(N_f) \times SU_R(N_f) \times U_L(1) \times U_R(1)$ symmetry. However, this symmetry is not completely realised by the QCD vacuum as the corresponding order parameter, the chiral condensate $\langle \bar{\psi}\psi \rangle$, does not vanish. This breaks the symmetry for separate left and right handed transformations of the fermion fields. For the following discussion it is thus advantageous to identify the relevant subgroups,

$$SU_L(N_f) \times SU_R(N_f) \times U_L(N_f) \times U_R(1) \cong SU_A(N_f) \times SU_V(N_f) \times U_A(1) \times U_V(1) , \quad (2.18)$$

where $\langle \bar{\psi}\psi \rangle \neq 0$ induces spontaneous breaking of the subgroup $SU_A(N_f)$. The corresponding symmetry breaking pattern reads

$$SU_L(N_f) \times SU_R(N_f) \rightarrow SU_V(N_f) . \quad (2.19)$$

To discuss the symmetries and in particular the special situation of $U_A(1)$ in more

detail, we begin by stating the related symmetry transformations.

$$SU_A(N_f) : \begin{cases} \psi & \rightarrow e^{i\alpha^j \tau^j \gamma_5} \psi \\ \bar{\psi} & \rightarrow \bar{\psi} e^{i\alpha^j \tau^j \gamma_5} \end{cases}, \quad (2.20a)$$

$$SU_V(N_f) : \begin{cases} \psi & \rightarrow e^{i\alpha^j \tau^j} \psi \\ \bar{\psi} & \rightarrow \bar{\psi} e^{-i\alpha^j \tau^j} \end{cases}, \quad (2.20b)$$

$$U_A(1) : \begin{cases} \psi & \rightarrow e^{i\alpha \gamma_5} \psi \\ \bar{\psi} & \rightarrow \bar{\psi} e^{i\alpha \gamma_5} \end{cases}, \quad (2.20c)$$

$$U_V(1) : \begin{cases} \psi & \rightarrow e^{i\alpha} \psi \\ \bar{\psi} & \rightarrow \bar{\psi} e^{-i\alpha} \end{cases}. \quad (2.20d)$$

The matrices τ^j generate $SU(N_f)$.

Explicit breaking of chiral symmetry due to finite quark masses can be investigated by means of the chiral currents,

$$j_V^\mu = \bar{\psi} \gamma^\mu \psi, \quad (2.21a)$$

$$j_A^\mu = \bar{\psi} \gamma^\mu \gamma_5 \psi, \quad (2.21b)$$

$$j_V^{\mu,a} = \bar{\psi} \gamma^\mu \tau^a \psi, \quad (2.21c)$$

$$j_A^{\mu,a} = \bar{\psi} \gamma^\mu \gamma_5 \tau^a \psi. \quad (2.21d)$$

From the classical Dirac equation,

$$i\partial_\mu \gamma^\mu \psi = M\psi, \quad (2.22)$$

where we now allow the mass, M , to be a matrix in flavour space, we have

$$\partial_\mu j_V^\mu = 0, \quad (2.23a)$$

$$\partial_\mu j_A^\mu = 2i\bar{\psi} M \gamma_5 \psi, \quad (2.23b)$$

$$\partial_\mu j_V^{\mu,a} = i\bar{\psi} [M, \tau^a] \psi, \quad (2.23c)$$

$$\partial_\mu j_A^{\mu,a} = i\bar{\psi} \{M, \tau^a\} \gamma_5 \psi. \quad (2.23d)$$

As can be seen from (2.23a), $U_V(1)$ is always conserved which corresponds to baryon number conservation. Although (2.23b) indicates $U_A(1)$ symmetry for vanishing quark masses, this is only true on the classical level. The interacting theory explicitly breaks $U_A(1)$ by quantum corrections even in the chiral limit,

$$\partial_\mu j_A^\mu = -\frac{g^2 N_f}{32\pi^2} \varepsilon^{\alpha\beta\mu\nu} F_{\alpha\beta}^c F_{\mu\nu}^c. \quad (2.24)$$

This is known as the Adler-Bell-Jackiw anomaly of QCD. This anomaly is expected to be restored at high temperatures [41] with possible implications on the $N_f = 2$ chiral transition that are discussed in chapter 5.

Such an anomaly does not exist for the flavour-multiplet axial current (2.23d) since the corresponding calculation is proportional to $\text{Tr} \tau^a = 0$. In fact, $SU_A(N_f)$ is spontaneously broken by the non-vanishing chiral condensate. The explicit symmetry breaking for $SU_A(N_f)$ sets in as soon as the quark mass is non-zero. This is different from the

situation for the vector symmetry and its current, (2.23c), which is conserved even for non-vanishing quark masses as long as the quark mass matrix is proportional to $\mathbf{1}$, i. e. as long as all considered flavours are mass degenerate.

In nature neither condition is realised. We have non-zero, non-degenerate quark masses, viz.

$$m_u \approx (1.7\text{--}3.3) \text{ MeV} , \quad (2.25a)$$

$$m_d \approx (4.1\text{--}5.8) \text{ MeV} , \quad (2.25b)$$

$$m_s \approx (80\text{--}130) \text{ MeV} \quad (2.25c)$$

$$\approx (22\text{--}30) \cdot \frac{m_u + m_d}{2} , \quad (2.25d)$$

where we quote the numbers as given by the Particle Data Group [39] in the $\overline{\text{MS}}$ scheme at a renormalisation scale of 2 GeV. One can still consider the symmetries to be approximately realised with the masses introducing relatively small corrections. This is in particular true for $N_f = 2$ with $m_u, m_d, m_d - m_u \ll \Lambda_{\text{QCD}}$. From this point of view, the three pions are the almost massless pseudo-Goldstone bosons for the spontaneously broken $SU_A(2)$ symmetry with

$$m_\pi^2 = B(m_u + m_d) . \quad (2.26)$$

To a lesser accuracy this also holds for $SU_A(3)$ augmenting the set of pseudo-Goldstone bosons by the pseudo-scalar mesons with strange valence quarks, $K_0, \overline{K}_0, K^\pm, \eta$. Accordingly, we can expect the kaon mass to be determined via

$$m_K^2 = B(m_u + m_s) ; \quad (2.27)$$

also cf. the discussion on chiral symmetry breaking in [42]. Note that in later parts of this thesis we will always consider the light up and down quarks to be mass degenerate so that it is not necessary to further distinguish their masses in the above formulae.

The approximate $SU_V(2)$ and $SU_V(3)$ symmetries allow to classify the hadrons according to multiplets in the sense of Gell-Mann and Ne'eman. We show as an example the multiplet of pseudo-Goldstone bosons in figure 2.1. The isospin triplet of pions for $SU_V(2)$ is realised to a good accuracy, with $m_{\pi^\pm} = 139.57018(35) \text{ MeV}$ and $m_{\pi^0} = 134.9766(6) \text{ MeV}$, whereas the difference to the other particles in the enlarged $SU_V(3)$ multiplet, with masses of the order of 500 MeV, is much larger. The experimental values have been taken from [39].

Finally, we mention that equations (2.26) and (2.27) can be understood in the context of a systematic approach. This is achieved by means of a low energy effective theory, viz. chiral perturbation theory (χPT). For an extensive review, also including lattice regularisation, we refer to the lectures by Sharpe [43]. The effective theory is built according to the chiral symmetry of QCD utilising the fields $\Sigma(x) \in SU(N_f)$ that transform as

$$\Sigma \rightarrow U_L \Sigma(x) U_R^\dagger , \quad (2.28)$$

where $U_L, U_R \in SU(N_f)$. Those fields are related to the (pseudo-)Goldstone particles,

$$\Sigma(x) = \exp(2i\pi^a(x)T^a/f) , \quad (2.29)$$

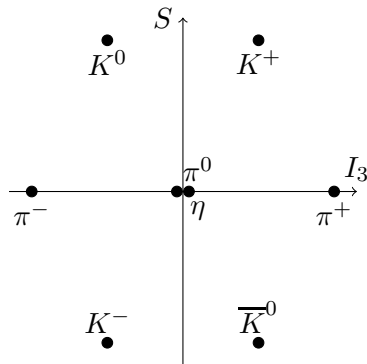


Figure 2.1.: Pseudo-scalar meson multiplet. The horizontal axis marks the third component of $SU(2)$ isospin, I_3 , for the (u, d) quark doublet. Along the vertical axis, the strangeness S of the particles increases. The particular visualisation chosen here is commonly found in textbooks, see e. g. figure 4.14a in [3].

following the notation in [43] for a field with vacuum expectation value $\langle \Sigma \rangle = 1$. The constant f balances dimensions and can eventually be associated with the pion decay constant. To construct the Lagrangian density that determines the low energy effective theory, one has now to consider all terms that are allowed by the symmetries of QCD to a given order in the power counting for derivatives and masses, $\partial^2 \sim M$. To leading order one obtains

$$\mathcal{L}_\chi = \frac{f^2}{4} \text{Tr} \left(\partial_\mu \Sigma \partial_\mu \Sigma^\dagger \right) - \frac{f^2}{4} \text{Tr} \left(\chi \Sigma^\dagger + \Sigma \chi^\dagger \right), \quad (2.30)$$

with $\chi = 2B_0 M$. Expanding the above Lagrangian density for the Goldstone fields, equation (2.29), leads to the relations between quark and Goldstone masses, i. e. the previously mentioned equations (2.26) and (2.27).

We rely on results obtained in χ PT several times later on. This includes in particular the discussion of the structure of bare parameter phase space for twisted mass fermions in section 4.1 and the crucial determination of the pion mass from the simulation parameters as explained in section 5.3.1.

2.3. Thermal Systems

Section 2.3.1 contains a summary of thermal field theory for QCD, based on [34], as far as we need it for this thesis. Connections to experiment are then drawn in section 2.3.2.

2.3.1. Thermal Field Theory

To describe thermal systems in equilibrium, we start with the grand-canonical partition function,

$$Z = \text{Tr} e^{-\beta(H - \mu_j N_j)}, \quad (2.31)$$

where μ_j are the chemical potentials for conserved particle numbers $n_j = \langle N_j \rangle$. However, for numerical simulations the inclusion of a non-zero chemical potential is a very intricate task due to the so-called sign problem of hybrid Monte-Carlo simulations. A

number of possible approaches to include at least small values of μ/T for the quark- or baryon-chemical potential have been pursued, for reviews see [10, 13]. Since this thesis concentrates on the first application of twisted mass fermions to thermodynamics of QCD, we will from now on work with zero chemical potential.

It is necessary to connect equation (2.31) to quantum field theories and in particular to QCD. This relation is known from textbooks [34]. The partition function is then written as a path integral over all degrees of freedom,

$$Z = \int \mathcal{D}[\psi, \bar{\psi}, A_\mu] e^{-S_E[\bar{\psi}, \psi, A_\mu]} . \quad (2.32)$$

The time direction which is meaningless to systems in equilibrium is traded for an additional Euclidean dimension of finite extent, $\beta = 1/T$, defining the temperature. The Euclidean action S_E can be obtained from its Minkowski counterpart in equation (2.1) by means of a Wick rotation from real to imaginary time, i. e. $\tau = -it$, where we identify the Euclidean time τ to be the fourth component of a four dimensional Euclidean vector $x_E = (x_1, x_2, x_3, x_4)$, see appendix A.2. Finally, the Euclidean action reads

$$S_E = \int d^3x \int_0^{1/T} d\tau \left(\sum_f \bar{\psi}_f(x) (\gamma_\mu D_\mu + m_f) \psi_f(x) + \frac{1}{4} F_{\mu\nu}^a(x) F_{\mu\nu}^a(x) \right) . \quad (2.33)$$

The finite extent in time direction leads to discrete energy levels determined by the so-called Matsubara frequencies,

$$\omega_n = \begin{cases} 2\pi n T & \text{(bosons)} \\ (2n + 1)\pi T & \text{(fermions)} \end{cases} , \quad n \in \mathbb{Z} . \quad (2.34)$$

Correspondingly, integrals in time direction are turned into discrete Matsubara sums. The difference between bosons and fermions is introduced by the boundary conditions for the fields in temporal direction. Whereas bosonic fields are periodic, fermions obey antiperiodic boundary conditions, i. e.

$$\psi(x + 1/T \hat{e}_4) = -\psi(x) . \quad (2.35)$$

This difference is ultimately related to the different statistics of the two types of particles leading to Fermi-Dirac and Bose-Einstein occupation numbers respectively.

Given the path integral representation of the grand canonical partition function, the thermal expectation value for a primary observable, K , is obtained as

$$\langle K \rangle = \frac{1}{Z} \int \mathcal{D}[\bar{\psi}, \psi, A_\mu] K[\bar{\psi}, \psi, A_\mu] e^{-S_E[\bar{\psi}, \psi, A_\mu]} . \quad (2.36)$$

Moreover, basic thermodynamic quantities can be calculated from the standard relations. For instance, the pressure of a homogeneous system is related to the partition function by

$$p = \frac{T}{V} \ln Z . \quad (2.37)$$

Note however, that in particular for numerical calculations in lattice QCD the overall normalisation of the partition function is not known. This poses no problem to expectation values as in equation (2.36). But to calculate the pressure or similar thermodynamic

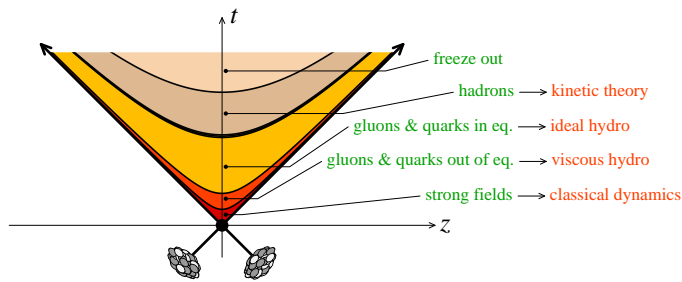


Figure 2.2.: Time evolution of relativistic heavy ion collisions (from [50]). The heavy nuclei can collide with different centrality. Shown is the evolution of the collision region. The first two stages refer to the early out-of-equilibrium situation before the Quark-Gluon Plasma is formed. With decreasing temperature the QGP undergoes a transition or crossover to the hadronic phase which finally freezes out.

quantities, a detour via derivatives and subsequent integration has to be followed since those derivatives can then be expressed in terms of standard expectation values which are accessible by the numerical simulations.

For the perturbative treatment of thermal systems, the relevant scale for the running coupling is set by the temperature [34, 44], $\mu_R \sim T$. According to equation (2.15) the coupling becomes temperature dependent, vanishing in the infinite temperature limit. This is the reason to expect a free gas of quarks and gluons for very high temperatures. However, close to the thermal transition the coupling is still large. Perturbative behaviour is not expected before temperatures many times larger than the transition temperature. Moreover, due to the Linde problem [4], a straightforward expansion into small couplings is in general not possible to arbitrary orders. Therefore, perturbation theory at finite temperature needs more sophisticated techniques to lead to results away from asymptotically large temperatures such as dimensional reduction or hard thermal loop calculations. For recent perturbative calculations of the pressure, see e. g. [45, 46, 47].

2.3.2. Heavy Ion Collisions and the Quark-Gluon-Plasma

Heavy ion collisions studied at the large colliders, RHIC and LHC, provide experimental insight — among others — into the physics accessible to lattice QCD simulations at vanishing chemical potential. Here we collect some information on heavy ion collisions in order to sketch the connection of these experiments and the related physics to this thesis. We base our collection mainly on the reviews by Braun-Munzinger and Stachel [48] as well as by Braun-Munzinger and Wambach [49].

In collisions of heavy ions, such as gold or lead, the overlapping parts of the nuclei create some intermediate partonic matter of high energy density far from equilibrium. The physics of this stage is not very well understood but there are models such as the colour glass condensate that are capable to provide initial conditions for the subsequent evolution (see e. g. [50]). For an illustration, see figure 2.2. It is supposed that shortly after the collision this matter reaches the (locally) equilibrated state of a quark-gluon plasma (QGP), i. e. a thermal system with quarks and gluons as relevant degrees of freedom. Note that this does not imply that the system can be described by a weakly coupled theory. In fact, the opposite is true and in the QGP just above the transition non-perturbative effects must not be neglected. Lattice simulations — which are at least

in their standard version restricted to thermal equilibrium — are capable to describe properties of this stage of evolution. The QGP formed in the collision is rapidly expanding and the description by hydrodynamic evolution has been successful, assuming an ideal fluid, i. e. vanishing viscosity.

The most prominent input of lattice QCD to the study of QGP so far has been the equation of state that is needed for a complete hydrodynamical treatment. The difficulties that can arise for mapping lattice results to the experiment are illustrated by another quantity, the transition temperature T_c . Lattice simulations allow to calculate this temperature associated with the thermal transition or crossover. The latter case is already ambiguous in itself since a crossover temperature necessarily depends on the chosen observable. In any case, experiments actually measure something different, the so-called freeze-out temperature T_{ch} . The freeze-out temperature can be determined from particle multiplicities by applying a statistical model that assumes chemical equilibrium has been reached after entering the hadronic phase [51]. Due to the close agreement between the range of lattice values for T_c and experimental results on T_{ch} , at least for small chemical potential where lattice QCD is most reliable, it has hence been argued that $T_c \gtrsim T_{\text{ch}}$ should indeed be expected for general reasons [52].

Since neither lattice QCD nor perturbative techniques can be used to investigate the phase transition of QCD for smaller temperatures but larger chemical potential, this regime can only be studied from models that have common symmetries with QCD or from some kind of generalisation such as the limit of large N_c . For a collection of results, we refer to the review by Fukushima and Hatsuda [5]. Whereas for vanishing chemical potential the thermal transition seems to combine the deconfinement of quarks and the restoration of chiral symmetry, there could be separate transitions at larger values of the chemical potential, possibly exhibiting different orders of phase transitions. For instance, based on calculations at large N_c it has been speculated that the parting of the two transitions introduces a new, chirally restored but still confined phase into the phase diagram of QCD [53, 54].

3. Quantum Chromodynamics on the Lattice

In this chapter we collect the necessary pieces to describe thermal systems of QCD by means of numerical simulations in the lattice framework. The introduction of lattice gauge theory dates back to the 1970s. The milestone work is credited to Wilson [6]. The application of numerical Monte-Carlo methods started some years later with the work of Creutz et al. [7, 8, 9]. Today a number of textbooks on the topic are available [55, 56, 57, 58]. For a presentation of lattice QCD at finite temperature, see [59].

Concerning the quark content of our study, we restrict ourselves to the up and down quarks as dynamical ingredients of our simulations. Eventually, dynamical strange as well as charm quarks should also be taken into account. We discuss the possible extension to four quark flavours in twisted mass QCD in chapter 6. In general, one can state that including quarks is numerically very expensive. Moreover, if one tried to consider all quark flavours, one would run into trouble to accommodate the large range of scales from a few MeV for the up and down quarks up to $m_t \sim 170$ GeV on the lattice. Therefore all lattice simulations so far are restricted to a relevant subset of quark flavours, usually up, down and possibly strange assuming heavier flavours to be dynamically irrelevant. Furthermore, for our two flavour case we adopt the general approach to take the quark masses to be degenerate $m_u = m_d =: m_{ud}$. This assumption is justified since the scale of mass splitting is much smaller than the one set by the temperature.

To illustrate the potential of lattice simulations, one can for instance refer to the agreement between lattice results and experimental values for the hadron spectrum in the light quark sector, see e. g. [61] for a recent review. As an example, we show the result by the Budapest-Marseille-Wuppertal collaboration in figure 3.1.

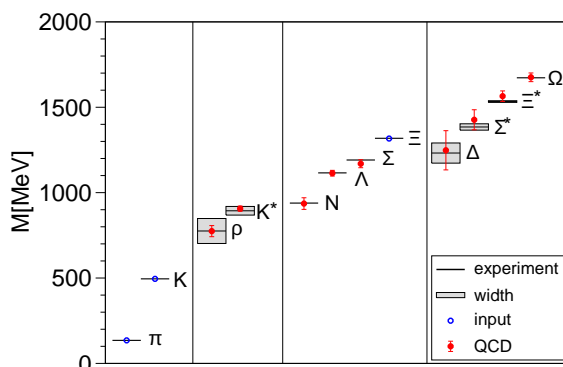


Figure 3.1.: Hadron spectrum determined by the BMW collaboration. The blue points have been used to set the scale, the red ones are lattice predictions. The gray entries are the experimentally determined masses. (from [60])

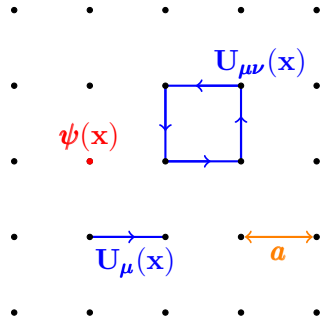


Figure 3.2.: Sketch of the lattice framework. The continuous Euclidean spacetime is replaced by a hypercubic lattice (here represented in two dimensions). The fermion fields $\psi(x)$ live on the lattice sites whereas the link variables $U_\mu(x)$ connect one site to another. The closed loop of links represents a plaquette.

We introduce the lattice discretisation for the pure gauge theory in the following section. The three sections that follow serve to discuss lattice fermions: Section 3.2 is devoted to general aspects of Wilson type fermions before we give a detailed overview on twisted mass fermions in section 3.3. In section 3.4 we include a short summary of alternative fermion discretisations. Afterwards, section 3.5 is used to explain the realisation of non-perturbative calculations in lattice QCD by means of computer simulations as well as the statistical analysis of the resulting numerical data.

3.1. Lattice Gauge Theory

To put QCD into the lattice framework, the rotation to Euclidean spacetime is mandatory even for calculating vacuum expectation values. Then the four-dimensional spacetime \mathbb{R}^4 with Euclidean metric can be replaced by a hypercubic lattice $\Gamma = a\mathbb{Z}^4$ with lattice spacing a as sketched in figure 3.2. Here we always consider a lattice spacing which is the same for all four directions.

The lattice works as a momentum cutoff $1/a$ that regulates the theory. The relation between coupling and lattice spacing is governed by the renormalisation group equation

$$a \frac{dg}{da} = -\beta(g) \quad (3.1)$$

where $\beta(g)$ is the QCD β -function. Since QCD is asymptotically free, we have thus a fixed point $g^*(a=0) = 0$ that determines the continuum limit of the lattice theory.

Since the cutoff imposes a minimal distance, local gauge invariance can no longer be an infinitesimal concept as in equation (2.4). Instead a finite parallel transport between neighbouring lattice sites x and $x + \hat{\mu}$ has to be used (where $\hat{\mu}$ denotes the vector of minimal length a along the μ -th direction). The corresponding link variables are members of the fundamental representation of $SU(N_c)$ and are connected to the gauge fields A_μ via

$$U_\mu(x) = e^{iagT^a A_\mu^a(x)} . \quad (3.2)$$

The simplest gauge invariant quantity that can be built out of the link variables is the trace of the plaquette. The plaquette itself is defined to be the product of link variables

along one square of lattice sites, i. e.

$$U_{\mu\nu}(x) = U_\mu(x)U_\nu(x + \hat{\mu})U_\mu^\dagger(x + \hat{\nu})U_\nu^\dagger(x) . \quad (3.3)$$

Therefore $U_{\mu\nu}$ can be used to construct the Wilson gauge action,

$$S_G = \beta a^4 \sum_x \sum_{\mu < \nu} \left(1 - \frac{1}{N_c} \text{ReTr} U_{\mu\nu}(x) \right) . \quad (3.4)$$

It is important to note that the path integral calculations for the determination of expectation values, such as equation (2.8) for zero temperature or equation (2.36) for thermal systems, have now to be performed using the group measure $\mathcal{D}U$ with the link variables instead of the continuum form $\mathcal{D}A_\mu$.

Expanding all links in powers of the lattice spacing yields the continuum Yang-Mills action as leading order,

$$S_G = \frac{1}{4} F_{\mu\nu}^a F_{\mu\nu}^a + \mathcal{O}(a^2) , \quad (3.5)$$

if the lattice gauge coupling is set to

$$\beta = \frac{2N_c}{g^2} . \quad (3.6)$$

To avoid confusion between the β -function, inverse temperature and the lattice coupling we use β only in its meaning of the gauge coupling for the rest of this work.

In thermal systems, the temporal extent, aN_τ , determines the temperature,

$$T = \frac{1}{aN_\tau} , \quad (3.7)$$

which ultimately defines a relation between lattice spacing and number of sites in temporal direction for a fixed physical situation. This is important as we adopt the common point of view for finite temperature lattice QCD that the lattice spacing is set by N_τ whereas a change in a , induced by a variation of the lattice coupling β , amounts to a change of temperature. The continuum limit is then reached as $1/N_\tau \rightarrow 0$ for fixed temperature.

As for any other type of regularisation, it is possible though cumbersome to perform perturbative calculations with the lattice regulator. The expansion is performed for small couplings, i. e. around the continuum limit so that the relevant degrees of freedom are once again the gauge fields A_μ . However, the crude momentum cutoff breaks Lorentz symmetry and is by no means intended to provide a simple scheme for perturbative calculations. It especially causes momenta to enter embedded into trigonometric functions so that one has to identify lattice momenta,

$$\hat{p} = 2 \sin \left(\frac{ap}{2} \right) \quad \text{and} \quad \bar{p} = \sin(ap) , \quad (3.8)$$

which can complicate calculations severely. Note that we use dimensionless lattice momenta which we find more convenient for later calculations. Alternatively, they are often dressed by an extra factor a^{-1} to have the mass dimension of continuum momentum. Besides the more complicated momentum dependence, the expansion of the link variables leads to vertices with any number of gluon lines. Finally, the need to resubstitute

the measure $\mathcal{D}U$ by $\mathcal{D}A_\mu$ introduces a non-trivial Jacobian that also adds new vertices. An extensive review on perturbation theory on the lattice is available from Capitani [62] where it is also clarified that perturbative lattice calculations are needed for at least two reasons. The first one is the assessment of lattice artefacts which can be worked out explicitly in perturbative calculations, see also section 4.2. The second one is the need to obtain matching coefficients between continuum renormalisations schemes such as $\overline{\text{MS}}$ and the lattice scheme.

We now discuss the possibility for improvement of the continuum approach. If lattice artefacts are known exactly, one can try to remove them a priori. The gauge action, equation (3.4), can be improved by adding higher dimension operators in the spirit of a Symanzik expansion [63], for details see [62]. The simplest terms that can be added are constructed from links along a rectangle, i. e. a closed planar path of length six. Indeed at tree-level these are the only relevant leading order operators to be added and the corresponding action can be expressed as

$$S_G = \beta a^4 \sum_x \left(c_0 \sum_{\mu < \nu} \left(1 - \frac{1}{N_c} \text{ReTr } U_{\mu\nu}(x) \right) + c_1 \sum_{\mu \neq \nu} \left(1 - \frac{1}{N_c} \text{ReTr } U_{\mu\nu}^{1 \times 2} \right) \right). \quad (3.9)$$

One has to set $c_0 = 1 - 8c_1$ in order to have the correct continuum limit. At tree-level all $\mathcal{O}(a^2)$ terms are removed if $c_1 = -1/12$. The corresponding action is called tree-level Symanzik improved (tlSym) [64, 65]. Relying on other arguments than tree-level improvement different choices for c_1 have been considered. Based on renormalisation group arguments, the Iwasaki action is obtained for $c_1 = -0.331$ [66, 67].

3.2. Wilson Fermions

Much more problematic than the treatment of the pure gauge sector is the discretisation of fermions. The core of the problem is sketched straightforwardly if one attempts a naive discretised version of the continuum derivative, cf. [62] for the following discussion,

$$\nabla_\mu \psi(x) = \frac{1}{2a} (\psi(x + \hat{\mu}) - \psi(x - \hat{\mu})) = \partial_\mu \psi(x) + \mathcal{O}(a^2). \quad (3.10)$$

The above relation provides the correct continuum limit but leads to a massless propagator in momentum space,

$$S_F = \left(\frac{i}{a} \sum_\mu \gamma_\mu \sin ap_\mu \right)^{-1}, \quad (3.11)$$

which has zeroes at the origin and in the edges of the first Brillouin zone which correspond to 2^4 fermions instead of the one originally intended. These fermions come in pairs of opposite chirality which is due to the fact that the Dirac equation, unlike those for scalar or vector particles, is of first order. Therefore in each direction the resulting first order zero of the inverse propagator needs to be accompanied by another zero with opposite slope.

The theoretical basis for understanding this so-called doubler problem is given by the no-go theorem by Nielsen and Ninomiya [68, 69] which can be summarised such that it

is impossible to find a lattice version of the Dirac matrix that is at the same time local, has the correct continuum limit, is free of doublers and respects chiral symmetry. The last condition can be expressed by the equation

$$\{D, \gamma_5\} = 0 . \quad (3.12)$$

Therefore, in order to remove the doublers from dynamical simulations, one has to violate one of the prerequisites of the theorem in one way or the other. The route taken by Wilson type fermions is to add an extra term to the fermion matrix,

$$-\frac{1}{2}ar\Box\psi(x) = -\frac{r}{2a}\sum_{\mu}(\psi(x+\hat{\mu})+\psi(x-\hat{\mu})-2\psi(x)) , \quad (3.13)$$

the so-called Wilson term. This operator is irrelevant in the continuum limit but gives an extra mass to the doublers which is proportional to $2r/a$ so that they decouple from the physical content of the theory for $a \rightarrow 0$. However, the Wilson term acts as a coupling dependent mass term so that chiral symmetry is explicitly broken for Wilson fermions at finite lattice spacing.

The complete Wilson lattice action including covariant derivatives reads

$$S_F[U, \psi, \bar{\psi}] = \sum_x \bar{\psi}(x) (1 - \kappa D_W[U]) \psi(x) \quad (3.14)$$

with the Wilson derivative acting as

$$D_W[U]\psi(x) = \sum_{\mu} \left((r - \gamma_{\mu})U_{\mu}(x)\psi(x + \hat{\mu}) + (r + \gamma_{\mu})U_{\mu}^{\dagger}(x - \hat{\mu})\psi(x - \hat{\mu}) \right) . \quad (3.15)$$

In the above formulae we have already used the field normalisation with hopping parameter κ that is commonly used for numerical simulations. It is connected to the notation based on the standard quark mass via

$$\psi \rightarrow \sqrt{2\kappa a^{-3/2}}\psi , \quad (3.16a)$$

$$\kappa = \frac{1}{2am_0 + 8r} . \quad (3.16b)$$

Explicit chiral symmetry breaking for Wilson fermions has some inconvenient consequences for practical applications. First of all, since the Wilson term acts like a mass that depends on the gauge coupling there is an additive mass renormalisation so that the chiral theory is realised for some non-vanishing value $m_c(g^2)$ of the bare quark mass. Furthermore, via the Wilson term discretisation artefacts that are linear in the lattice spacing are introduced. This complicates the continuum approach considerably and is the reason for the development of improved Wilson fermion formulations such as the maximally twisted mass fermions, which is discussed in the following section, and clover improved fermions.

Clover improvement works by adding a counterterm in the sense of Symanzik's expansion to the fermion action, the so-called Sheikholeslami-Wohlert term [70],

$$S_{\text{SW}} = c_{\text{sw}} \frac{ia\kappa}{4} \sum_x \sum_{\mu\nu} \sigma_{\mu\nu} F_{\mu\nu}(x) , \quad (3.17)$$

where $\sigma_{\mu\nu} = i/2[\gamma_\mu, \gamma_\nu]$ and $F_{\mu\nu}$ is the clover-leaf representation of the gluon field strength,

$$F_{\mu\nu}(x) = \frac{1}{8iga^2} \sum_{\mu\nu=\pm} \left(U_{\mu\nu}(x) - U_{\mu\nu}^\dagger(x) \right). \quad (3.18)$$

In order to achieve full improvement, i.e. remove all cutoff effects of $\mathcal{O}(a)$, besides the action each operator has to be modified by the appropriate higher order terms. Then, finally it is necessary to adjust the parameters of the action, m_0 , m_c , g_0 , c_{sw} as functions of the quark mass and the coupling. These relations have been worked out perturbatively [71, 72, 73, 74]. The relations for the quark mass and bare coupling read

$$m_R = Z_m(g^2)(m_0 - m_c(g^2))(1 + b_m(g^2)am), \quad (3.19a)$$

$$g_{\text{sw}}^2 = g^2(1 + b_g(g^2)am_q). \quad (3.19b)$$

It must be noted that even the limit of a free theory needs a shift in the bare quark mass in order to be improved, $m_R(g=0) = m_0(1 + b_m(g=0)am)$.

The clover coefficient needed to improve the theory is known in perturbation theory. In leading order it is $c_{\text{sw}} = 1 + \mathcal{O}(g^2)$. However, more appropriate for actual simulations is the non-perturbative determination by Jansen and Sommer [75]. Recent studies of thermal QCD with clover improved Wilson fermions can be found in [76, 77, 78, 79, 80].

3.3. Twisted Mass Fermions

The modification of Wilson type fermions by a chirally twisted mass term has been introduced about a decade ago [81, 82]. Some years later Frezzotti and Rossi realised that the theory is automatically $\mathcal{O}(a)$ -improved if the original untwisted mass is set to its critical value [83]. Our presentation of twisted mass lattice fermions is based on the review by Shindler [84].

3.3.1. Twisted Mass Formulation

The central key to the introduction of twisted mass fermions is the transformation

$$\psi = e^{i\omega\gamma_5\tau^3/2}\chi \quad \text{and} \quad \bar{\psi} = \bar{\chi}e^{i\omega\gamma_5\tau^3/2} \quad (3.20)$$

which is a symmetry of the continuum action if the mass term is reinterpreted appropriately. ψ , in the so-called physical basis, and χ , in the twisted basis, are flavour doublets and the third Pauli matrix τ^3 acts in the according flavour space. It is then possible to reformulate the QCD action as

$$S_F = \int d^4x \bar{\chi}(x) (\gamma_\mu D_\mu + m_0 + i\mu_0\gamma_5\tau^3) \chi(x). \quad (3.21)$$

The bare quark mass is related to the untwisted and twisted components,

$$\mu_0 = m_q \sin \omega, \quad (3.22a)$$

$$m_0 = m_q \cos \omega, \quad (3.22b)$$

$$m_q = \sqrt{m_0^2 + \mu_0^2}, \quad (3.22c)$$

with the corresponding twist angle ω ,

$$\tan \omega = \frac{\mu_0}{m_0} . \quad (3.23)$$

The twist angle obviously changes under renormalisation as the untwisted and twisted mass components do not share the same renormalisation factor. The renormalised quark mass is determined as

$$m_R = \sqrt{Z_m^2(m_0 - m_c)^2 + Z_\mu^2 \mu_0^2} . \quad (3.24)$$

Only if the untwisted quark mass is set to its critical value, the angle, $\omega = \pi/2$, is independent of renormalisation. This case is called maximal twist.

Applying the Wilson discretisation to the continuum action with twisted mass term, we obtain

$$S_F[U, \psi, \bar{\psi}] = \sum_x \bar{\chi}(x) (1 - \kappa D_W[U] + 2i\kappa a \mu_0 \gamma_5 \tau^3) \chi(x) . \quad (3.25)$$

A particular feature of the twisted mass fermion matrix,

$$M_{\text{tm}} = 1 - \kappa D_W[U] + 2i\kappa a \mu_0 \gamma_5 \tau^3 , \quad (3.26)$$

that was important for the original motivation to introduce this modification of Wilson fermions is that the twisted mass parameter acts as a regulator protecting simulations from zero modes. These zero modes have been a source of concern in the untwisted theory [82]. This property can be seen when evaluating the flavour determinant explicitly,

$$\text{Det}_{\text{flavour}} M_{\text{tm}} = M_W M_W^\dagger + (a\mu_0)^2 , \quad (3.27)$$

where M_W denotes the standard Wilson fermion matrix for one flavour.

Inversion of equation (3.26) in momentum space for a free field leads to the determination of the propagator,

$$S_{\text{tm}}(p) = a \frac{-i \sum_\nu \gamma_\nu \bar{p}_\nu + \frac{1}{2} \hat{p}^2 + am_0 - ia\mu_0 \gamma_5 \tau^3}{\bar{p}^2 + (\frac{1}{2} \hat{p}^2 + am_0)^2 + (a\mu_0)^2} , \quad (3.28)$$

which is important for the later analytical calculations in the free and weakly coupled limits.

3.3.2. Automatic Improvement

Since the twist rotations (3.20) are no more a symmetry of the lattice action due to the Wilson term, the fermion discretisation provides different regularisations depending on the twist angle. That means in particular that the cutoff effects are functions of the twist. It has been shown that the leading $\mathcal{O}(a)$ effects vanish in most relevant quantities if the action is tuned to maximal twist. More precisely, this statement applies to parity even quantities as can be derived from the symmetries of the Symanzik expansion [84, 85]. This feature is known as automatic $\mathcal{O}(a)$ -improvement and is the crucial property for current applications of twisted mass fermions.

We now briefly sketch the main idea for the proof of automatic $\mathcal{O}(a)$ improvement following the review by Shindler [84]. The starting point is the Symanzik expansion for the lattice action,

$$S_{\text{eff}} = S_0 + aS_1 + \dots , \quad (3.29)$$

where S_0 is the continuum action. The higher order contributions,

$$S_n = \int d^4y \mathcal{L}_n, \quad (3.30)$$

are constructed from all possible counterterms. Especially, we have in next-to-leading order

$$\mathcal{L}_1 = \sum_{k=1}^5 c_k \mathcal{O}_k. \quad (3.31)$$

We do not give the explicit form of the operators \mathcal{O}_k here but refer to [84] where the complete set is given. The coefficients c_k have then to be tuned such that continuum calculations with S_{eff} reproduce the lattice theory up to the chosen order of a . A similar expansion holds for any field observable,

$$\phi_{\text{eff}} = \phi_0 + a\phi_1 + \dots. \quad (3.32)$$

With the above expansions, one can identify the possible discretisation effects to $\mathcal{O}(a)$ for an arbitrary expectation value,

$$\begin{aligned} \langle \phi(x_1) \dots \phi(x_n) \rangle &= \frac{1}{Z} \int \mathcal{D}[\bar{\psi}, \psi, A_\mu] \phi(x_1) \dots \phi(x_n) e^{-S_0} (1 - aS_1 + \dots) \\ &= \langle \phi_0(x_1) \dots \phi_0(x_n) \rangle_0 \\ &\quad - a \int d^4y \langle \phi_0(x_1) \dots \phi_0(x_n) \mathcal{L}_1(y) \rangle_0 \\ &\quad + a \sum_{k=1}^n \langle \phi_0(x_1) \dots \phi_1(x_k) \dots \phi_0(x_n) \rangle_0 + \mathcal{O}(a^2), \end{aligned} \quad (3.33)$$

where contact terms can be absorbed into a redefinition of the fields. For the proof of automatic improvement one can utilise the following symmetry of the lattice action,

$$R_5^1 \times \mathcal{D} \times [\mu \rightarrow -\mu], \quad (3.34)$$

where \mathcal{D} multiplies all terms by $(-1)^{d_m}$ according to their mass dimension d_m . R_5^1 transforms the fields as

$$\chi \rightarrow i\gamma_5 \tau^1 \chi, \quad (3.35a)$$

$$\bar{\chi} \rightarrow \bar{\chi} i\gamma_5 \tau^1. \quad (3.35b)$$

This symmetry holds for the lattice action even in the infinite volume limit. Therefore all terms on the right hand side of equation (3.33) have to respect the symmetry. This necessitates the absence of $\mathcal{O}(a)$ terms for any field ϕ that respects R_5^1 since then both contributions to that order in equation (3.33) are odd under the above symmetry. For the first part, $\phi_0(x_1) \dots \phi_0(x_n) \mathcal{L}_1(y)$, this is true because of the operator insertions in \mathcal{L}_1 . The second part, $\phi_0(x_1) \dots \phi_1(x_k) \dots \phi_0(x_n)$ is odd because of the mass dimension of ϕ_1 that has to be different by 1 from that of ϕ_0 so that all terms in equation (3.32) possess the same symmetries. Introducing an untwisted quark mass to the lattice action explicitly breaks the crucial symmetry (3.34) and therefore there is no automatic

improvement except for maximal twist. Note that according to the above arguments also quantities with vanishing expectation value can have discretisation effects in $\mathcal{O}(a)$.

A possible caveat is posed by pion poles, i. e. by cutoff effects that are of $\mathcal{O}(a^{2k}/m_\pi^{2h})$ with $2k \geq h \geq 1$. These poles can be avoided by a suitable definition of maximal twist. For this reason ETMC have adopted the condition of a vanishing PCAC (partially conserved axial current) quark mass [86],

$$m_{\text{PCAC}} = \frac{\sum_{\mathbf{x}} \langle \partial_4 A_4^a(\mathbf{x}, t) P^a(0) \rangle}{2 \sum_{\mathbf{x}} \langle P^a(\mathbf{x}, t) P^a(0) \rangle}, \quad (3.36)$$

where $P^a = \bar{\psi} \gamma_5 \tau^a / 2\psi$, $A_\mu^a = \bar{\psi} \gamma_\mu \gamma_5 \tau^a / 2\psi$. From the numerical side a quenched test of a^2 -scaling with this condition has been presented in [87, 88, 89].

On the level of free lattice fermions the improvement can be observed easily, for instance, for the dispersion relation that is obtained from the pole of the propagator, $S_F(\mathbf{p}, p_4 = iE)$,

$$E(\mathbf{p}) = \sqrt{\mathbf{p}^2 + m_q^2} - a \frac{m_q^3}{2} \frac{\cos(\omega)}{\sqrt{\mathbf{p}^2 + m_q^2}} + \mathcal{O}(a^2). \quad (3.37)$$

The improvement for maximal twist, $\omega = \pi/2$ is apparent. Note that for a theory without spontaneous breaking of chiral symmetry, like in the free limit, the linear cutoff effects have to be proportional to the quark mass. This is not necessarily the case in the presence of spontaneous chiral symmetry breaking [85].

Automatic improvement also holds at finite temperature. This is expected since the relevant symmetries do not mix spatial and temporal directions so that the finite time extent which characterises simulations at finite temperature does not interfere with the improvement. A report of observed a^2 -scaling at finite temperature in the quenched case has been given by our tmfT collaborators [90]. Our perturbative analysis of the pressure, discussed in section 4.2, finds improvement at maximal twist as well.

Another possible drawback of twisted mass fermions is the breaking of flavour symmetry. Flavour singlet and doublet quantities such as m_π^0 and m_π^\pm may show large splittings for finite lattice spacing. Indeed in case of the pion these large splittings have been observed [91]. A theoretical analysis in the Symanzik expansion scheme allows to identify the leading orders of cutoff effects [92],

$$(m_\pi^0)^2 = m_\pi^2 + a^2 \zeta_\pi + \mathcal{O}(a^2 m_\pi, a^4), \quad (3.38a)$$

$$(m_\pi^\pm)^2 = m_\pi^2 + \mathcal{O}(a^2 m_\pi^2, a^4). \quad (3.38b)$$

The leading order of the splitting, ζ_π , originates solely in the neutral sector and turns out to be large. Important to note is that the large size of splitting cutoff effects is restricted to the pion mass and related quantities.

3.3.3. Phase Diagram

As for all Wilson type fermions, twisted mass fermions can exhibit unphysical phases in their bare parameter space that is spanned by the hopping parameter, the lattice coupling and the twisted mass. Its vacuum structure has been studied extensively [93, 94, 95, 96, 97, 98]. From ordinary Wilson fermions it is known that there is

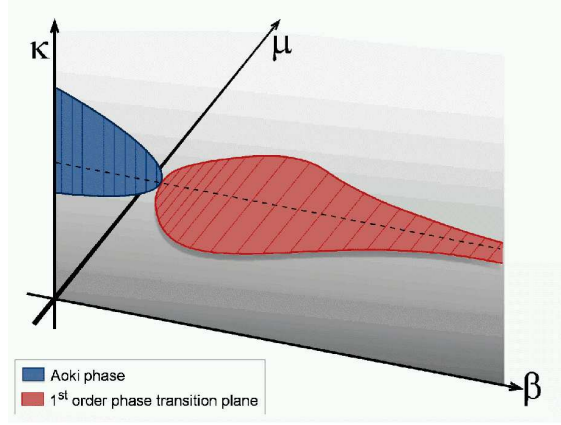


Figure 3.3.: Phase diagram in (κ, β, μ_0) parameter space, from [96]. The strong coupling region, i.e. the region of small lattice coupling β , exhibits the Aoki phase in the plane of vanishing twisted mass parameter μ_0 . For weaker couplings a surface of bulk transitions is encountered that contains the line of critical hopping parameter, $\kappa_c(\beta)$ and extends to $\mu_0 \neq 0$. The width of this surface vanishes towards the continuum limit.

the so-called Aoki phase of broken parity-flavour symmetry in the strong coupling region [99, 100]. For twisted mass fermions, that additionally have the μ_0 -axis in their bare parameters phase diagram, another unphysical phase appears for intermediate couplings that shrinks towards the continuum limit. This phase is a surface of first order transitions that incorporates the line of critical hopping parameters $\kappa_c(\beta)$. These findings are summarised in the sketch in figure 3.3.

The theoretical explanation for these two phases can be worked out in the framework of chiral perturbation theory [101, 102] which allows to investigate the vacuum structure of its effective Lagrangian by means of minimising the corresponding potential. For this purpose, the continuum Lagrangian given in equation (2.30) has, of course, to be supplemented by the leading cutoff effects,

$$\mathcal{L}_\chi = \frac{f^2}{4} \text{Tr} \left(\partial_\mu \Sigma \partial_\mu \Sigma^\dagger \right) - \frac{f^2}{4} \text{Tr} \left(\chi \Sigma^\dagger + \Sigma \chi^\dagger \right) - \frac{f^2}{4} \text{Tr} \left(\rho \Sigma^\dagger + \Sigma \rho^\dagger \right), \quad (3.39)$$

with $\chi = 2B_0(m\mathbf{1} - i\mu\tau^3)$ and $\rho = 2aW_0\mathbf{1}$, slightly adjusting the notation in [102]. ρ parametrises the cutoff effects. Note that it enters the Lagrangian in the same way as the quark mass so that the leading cutoff effects essentially lead to a shift in the bare quark mass, cf. also the discussion in [101]. The potential that can be extracted from the above Lagrangian can be expressed in terms of a unit four vector, $u = (u_0, u_1, u_2, u_3)$ [102],

$$V = -c_1 u_0 + c_2 u_0^2 + c_3 u_3. \quad (3.40)$$

This vector parametrises Σ ,

$$\Sigma = u_0 \mathbf{1} + i u_a \tau^a, \quad (3.41)$$

so that its components determine the vacuum structure, in particular,

$$u_0 \sim \langle \bar{\psi} \psi \rangle, \quad (3.42a)$$

$$u_3 \sim \langle \bar{\psi} \gamma_5 \tau^3 \psi \rangle. \quad (3.42b)$$

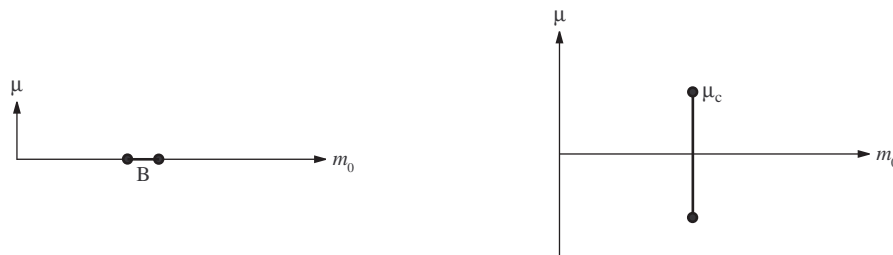


Figure 3.4.: Possible phase transition scenarios for Wilson fermions with twisted mass term. Left: Aoki phase. Right: Normal scenario, also called Sharpe-Singleton scenario. (from [102])

The coefficients $c_1 = 2f^2(B_0m_q + W_0a)$ and $c_3 = 2f^2B_0\mu_0$ are directly related to the quark mass and cutoff effects. However, the crucial observation is that the sign of c_2 is not determined from the Lagrangian. Therefore, the vacuum structure can be qualitatively different depending on that sign. The two possible scenarios have been mapped out in [102]. The first possibility, $c_2 > 0$, leads to the previously known Aoki phase of broken flavour symmetry, $\langle \bar{\psi}\gamma_5\tau^3\psi \rangle \neq 0$, if the twisted mass vanishes. The second scenario, $c_2 < 0$, corresponds to the Sharpe-Singleton plane of bulk transitions that has been found for weaker couplings numerically. This plane incorporates the critical untwisted quark mass and extends to non-vanishing twisted mass. It ends for some critical $\mu_c \sim a^2$ and thus vanishes in the continuum limit. A sketch of the two scenarios is shown in figure 3.4.

3.4. Alternative Fermion Discretisations

Although this thesis deals with Wilson type fermions only, we include a short presentation of alternative formulations for the sake of comparability. The so-called staggered fermions [11] and in particular improved versions thereof are the second major type of fermions that is frequently used for numerical simulations, for modern explanations see e. g. [57, 62]. Many results concerning QCD thermodynamics have been obtained relying on staggered fermions, for example the prediction of a crossover for the thermal transition with physical quark masses [17]. For recent work the Budapest-Wuppertal [19, 21, 103, 104] and HotQCD [20, 105, 106] collaborations should be named.

Staggered fermions are constructed from the naive action by means of a spinor transformation that untangles the four components of the spinor fields ψ . This reduces the number of doublers from 16 to 4. The remaining degrees of freedom are labeled by ‘tastes’.

The major advantage of staggered fermions is that they have a residual chiral symmetry at finite lattice spacing that protects the mass from additive renormalisation. However, in order to have individual degrees of freedom, one still has to remove the remaining four-fold degeneracy. This is usually done by adding a fourth root to the fermion determinant for staggered fermions, i. e.

$$\int \mathcal{D}[U] \text{Det} (M_{\text{stag}}[U]) e^{-S_g[U]} \longrightarrow \int \mathcal{D}[U] \text{Det} (M_{\text{stag}}[U])^{1/4} e^{-S_g[U]}, \quad (3.43)$$

where M_{stagg} represents the staggered fermion matrix. In perturbation theory this procedure works without problems since order by order the number of flavours is just divided by 4. But there is an on-going controversy on whether non-perturbative effects might hamper the correct continuum limit [15, 16, 107]. Rossi and Testa have provided a zero-dimensional example where the rooting procedure fails non-perturbatively [108]. Furthermore, staggered fermions are not free of some particular systematic effects that need to be controlled. Most prominently taste breaking has to be named, see e. g. [109] for a report that also considers thermodynamic quantities.

A possibility to avoid fermion doublers at all and to maintain some kind of chiral symmetry at the same time is to change equation (3.12) to the Ginsparg-Wilson relation [110],

$$\gamma_5 D + D \gamma_5 = \frac{a}{\rho} D \gamma_5 D , \quad (3.44)$$

This allows for a redefined chiral symmetry that holds for finite lattice spacing. Neuberger provided a solution to the Ginsparg-Wilson equation with the so-called overlap fermions [111, 112]. The drawback of this type of fermions is that they are computationally very expensive. The same is true for domainwall fermions which also satisfy the Ginsparg-Wilson relation but are constructed in five space time dimensions [113, 114]. Since chiral fermions are very expensive to simulate, there have been only few finite temperature studies so far [115, 116, 117].

An alternative to the established fermion types that has become popular recently avoids the doubler issue by changing the lattice geometry. The first action of this type goes back to Karsten and Wilczek [118, 119] but the current interest in those minimally doubled fermions is due to a suggested action by Creutz [120, 121] who proposed a four dimensional generalisation of a graphene model. Lattice cutoff effects at tree-level have been investigated early on and seem to be under control [122, 123]. However, the lack of symmetries leads to new relevant operators that have to be controlled by appropriate counterterms [124]. Progress on the way to a dynamical simulation with minimally doubled fermions has been reported recently [125, 126]. In absence of dynamical simulations there are, of course, no thermal QCD studies so far. We have calculated the free pressure for chiral fermions which indicates that lattice artefacts might be small, see figure 3.5. However, the understanding of minimally doubled actions is still developing. Especially the implications of a non-hypercubic lattice symmetry need to be carefully controlled before these fermions can be applied to large scale simulations. Note that usually the time direction is in some way special for these discretisation schemes with possible non-trivial implications for finite temperature QCD where the Euclidean time extent determines the temperature.

3.5. Numerical Simulations

In this section we present the Hybrid Monte-Carlo algorithm that we have used for our simulations and discuss important issues about the statistical analysis of the obtained data as well as sources for systematic errors.

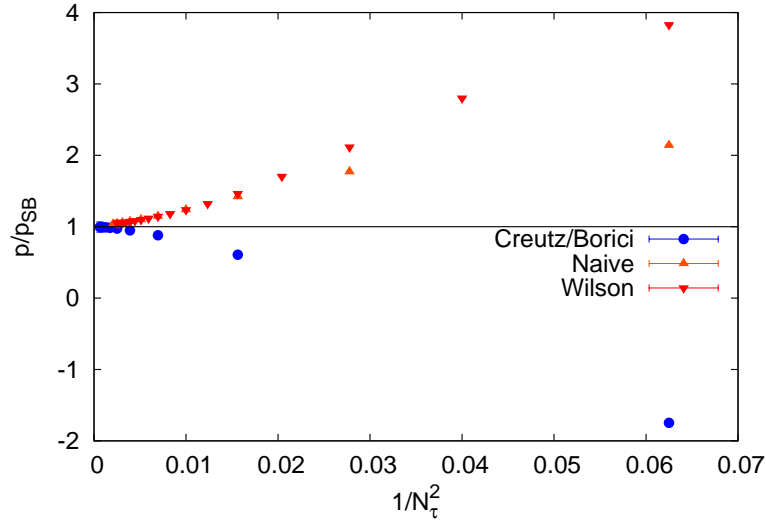


Figure 3.5.: Free pressure for massless fermions normalised to the continuum limit for naive, standard Wilson and Creutz fermions (the latter according to [120] with parameters $B = 1$ and $C = 1/\sqrt{2}$).

3.5.1. Hybrid Monte-Carlo

We now explain how actual simulations are performed, i. e. how an expectation value,

$$\begin{aligned} \langle K \rangle &= \frac{1}{Z} \int \mathcal{D}[\psi, \bar{\psi}, U] K[\psi, \bar{\psi}, U] e^{-S_g[U] - S_F[\psi, \bar{\psi}, U]} \\ &= \frac{1}{Z} \int \mathcal{D}[U] \text{Det}(M_F[U]) \tilde{K}[U] e^{-S_g[U]}, \end{aligned} \quad (3.45)$$

is calculated numerically. As indicated above, it is always possible to integrate out the fermionic fields analytically, cf. equation (2.11). For finite volume there is a high-dimensional integral left for numerical integration so that a representative subset of configuration space has to be chosen in order to reach a result in finite time. This is done by means of the so-called importance sampling, i. e. by applying an algorithm that generates a set of gauge fields $\{U_n\}$ with the correct probability measure so that for any observable the correct expectation value is obtained,

$$\frac{1}{N_{\text{meas}}} \sum_{n=0}^{N_{\text{meas}}} A[U_n] \xrightarrow{N_{\text{meas}} \rightarrow \infty} \langle A \rangle. \quad (3.46)$$

The corresponding probability measure is given by the action,

$$P[U] = \text{Det}(M_F[U]) e^{-S_g[U]}, \quad (3.47)$$

and is realised by means of a molecular dynamics evolution combined with a Metropolis accept/reject step, the so-called hybrid Monte-Carlo (HMC) algorithm [127]. Since a probability measure has to be real, it is obvious that importance sampling only works

for a real fermion determinant. That is the cause for the breakdown of HMC algorithms at finite chemical potential μ since the determinant turns complex,

$$\text{Det}M_F(\mu) = (\text{Det}M_F(-\mu^*))^* . \quad (3.48)$$

Our work is based on the algorithm described in [128]. It is improved as compared to the standard HMC, e.g. by the choice of a multiple time scale integrator and the application of mass preconditioning. This means that in order to optimise the algorithm for a particular simulation one can adjust five parameters: the preconditioning mass, the step numbers for three integrators and the trajectory length. After initial optimisation of the parameters we have kept them fixed for each simulation at one pion mass so that properties of the algorithm, especially the length of autocorrelations, can be interpreted as supplementary signals of physical criticality.

The implementation in a \mathbf{C} code is described in [129]. This is the very code we have used for our simulations on the HLRN machine in Berlin ¹. Additionally, we have performed simulation on the APEnext at INFN in Rome ². For the APE machine, we have an earlier version of the same program written specifically for APE computers.

3.5.2. Data Analysis

Since the configurations from a Monte-Carlo simulation are generated consecutively, each one based on its predecessor, the generated data form a Markov chain. The statistical analysis thus has to take into account correlations. The following summary is based predominantly on [130] but see also [55, 131].

For the following, we consider the primary observable A which can be expressed as a function of the gauge field configurations, identifying

$$A_j = A[U_j] \quad (3.49)$$

for a given configuration U_j . The estimator for the mean $\langle A \rangle$ is the average \bar{A} ,

$$\bar{A} = \frac{1}{N} \sum_{j=1}^N A_j . \quad (3.50)$$

The correct estimate for the variance of \bar{A} needs to take autocorrelations into account which can be quantified by the integrated autocorrelation time τ_{int} ,

$$\tau_{\text{int}} = \frac{1}{2\Gamma(0)} \sum_{t=-\infty}^{\infty} \Gamma(t) , \quad (3.51)$$

with the autocorrelation function

$$\Gamma(t) = \langle (A_i - \langle A \rangle)(A_{i+t} - \langle A \rangle) \rangle . \quad (3.52)$$

The above definitions allow to express the variance of \bar{A} ,

$$\sigma_{\bar{A}}^2 = \frac{2\tau_{\text{int}}}{N} \Gamma(0) . \quad (3.53)$$

¹For more information, see <https://www.hlrn.de/> .

²For more information, see <http://apegate.roma1.infn.it/APE/> .

This can be interpreted so that the effective amount of data is reduced by a factor of $2\tau_{\text{int}}$ as compared to the uncorrelated case. With our definition uncorrelated data have an integrated autocorrelation time of $1/2$.

Suitable estimators for a set of N data points are

$$\hat{\Gamma}(t) = \frac{1}{N - |t|} \sum_{i=1}^{N-|t|} (A_i - \bar{A}) (A_{i+|t|} - \bar{A}) \quad (3.54)$$

and

$$\hat{\tau}_{\text{int}} = \frac{1}{2\hat{\Gamma}(0)} \sum_{t=-M}^M \hat{\Gamma}(t). \quad (3.55)$$

The truncation M is needed since for arbitrarily large t the noise dominates the exponentially weak signal. M must be adjusted in practice by estimating a plateau behaviour as a function of this cutoff. In our later data analysis, we will supplement our set of observables by the the integrated autocorrelation time to find pseudo-critical points. This is because τ_{int} defines a length scale of the system that should clearly peak close to critical or pseudo-critical points if all algorithmic parameters are kept constant.

In order to reliably calculate the variance of our data sets, we have chosen to apply the standard method of jackknife binning, i.e. one uses prebinned block averages,

$$b_k = \frac{1}{N - N_B} \sum_{j \notin [kN_B, (k+1)N_B]} A_j, \quad (3.56)$$

that can be assumed to be free of correlations,

$$\sigma_A^2 = \frac{N_B - 1}{N_B} \sum_{k=1}^{N_B} (b_k - \bar{b})^2. \quad (3.57)$$

The number of bins N_B needs to be large enough in order to reliably allow for a Gaussian treatment based on the central limit theorem. At the same time N_B should be small so that correlations between the bins are really removed. The best value can be adjusted by searching for a plateau of the error as a function of the bin size very similar to what we have mentioned above for the integrated autocorrelation time. Actually, once N_B is fixed, one can use equation (3.53) in order to obtain τ_{int} . For an error estimate for τ_{int} , we follow [131].

We show an example in figure 3.6. The plateau behaviour is identified consistently for a bin size of 325 corresponding to $N_B = 20$. The remaining fluctuations in that region indicate the uncertainty in the determination of the error and τ_{int} estimates. Of course, alternative approaches such as Wolf's Γ -method [132] are consistent with our choice of the jackknife binning.

Aside from the statistical errors, there are two major sources of systematic effects for lattice simulations. The first one is given by the cutoff effects. Results at several values of the lattice spacing have to be extrapolated to the continuum limit relying on the assumed functional dependence of the quantity on the lattice spacing, usually $A_{\text{latt}} = A_{\text{cont}} + a^2 c_2 + \dots$. Even then, it is important that the a^2 -scaling region has already been reached for the lattice spacings under consideration, i.e. the cutoff effects need to be dominated by the leading a^2 corrections to the continuum value.

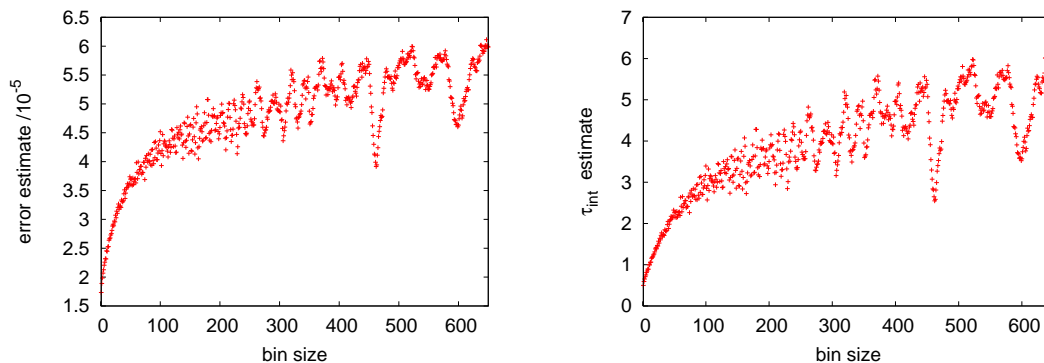


Figure 3.6.: Example of estimates of the error and the integrated autocorrelation time as a function of jackknife bin size. The data sample has a statistics of 6500 points and corresponds to the real part of the Polyakov loop of one of our scans ($\beta = 3.9675$ of A12). The chosen $N_B = 20$ corresponds to a bin size of 325.

The second source of systematic effects is due to the finite volume that is necessary for computer simulations. Often finite volume effects can be expected to be small. For instance it has been shown by Lüscher [133] that finite volume corrections to the hadron spectrum are exponentially suppressed. For these considerations to hold, the volume has to be larger than some minimal size. A quantity that can be used to assess whether this condition is fulfilled is the product of the pion mass m_π and the spatial extent L . Since the pion wavelength is determined by $1/m_\pi$ the combination $m_\pi L$ is suitable to decide if the pion — and thus any heavier particle — fits into the simulated box. A rule of thumb is that $m_\pi L$ should be larger than 3, at least.

4. Properties of Twisted Mass QCD at Finite Temperature

In this chapter we present results on properties of twisted mass fermions at finite temperature that have been obtained in direct continuation of the diploma thesis [134] and have been published in [29, 31]. The first part, section 4.1, presents the relevant contributions to [29] by this thesis, i. e. simulations scanning the space of bare parameters of twisted mass QCD — μ_0, β, κ — are compared to theoretical expectations based on chiral perturbation theory in order to develop an understanding for the implications of the non-trivial phase structure. The second part, section 4.2, summarises what we have found out about cutoff effects of twisted mass QCD at finite temperature by means of perturbative calculations of the pressure.

4.1. Phase Diagram

We sketch the theoretical expectations for the properties of the (μ_0, β, κ) -phase diagram (section 4.1.1) before we confront them with the outcome of our Monte-Carlo simulations in section 4.1.2.

4.1.1. Theoretical Expectations

Since the critical temperature depends on the quark mass, the thermal transition introduces a critical line $\kappa_t(\beta)$ into the (κ, β) -phase space of standard Wilson fermions. Furthermore, because there is also a thermal transition in pure gauge theory, i. e. at infinite quark mass, κ_t must eventually end for $\kappa = 0$ at some finite β_{qu} , cf. the qualitative discussion by Creutz [135]. This phase structure has been found along with a persisting Aoki phase in numerical investigations, cf. [136, 137] and figure 4.1.

For the enlarged phase space of twisted mass fermions, Creutz has given a prediction based on continuum limit arguments [138]. The crucial point is that the continuum theory is invariant under twist rotations. Hence, there have to be closed lines in (m, μ) -space where the thermal transition is situated, cf. figure 4.2, left. Creutz argued that this situation should also hold on the lattice when approaching the continuum limit up to some unknown distortions by lattice artefacts. This implies that the thermal line $\kappa_t(\beta)$ for vanishing twist is part of a closed conical surface that wraps around the zero temperature chiral critical line $\kappa_c(\beta)$. For a fixed lattice coupling β a slice of this surface has to form a distorted ellipse. A sketch of this conjectured phase diagram is presented in figure 4.2, right.

At tree-level, this conjecture consequently leads to lines of constant physics defined by

$$a^2 \mu_0^2 + \frac{1}{4} \left(\frac{1}{\kappa} - \frac{1}{\kappa_c} \right)^2 = \text{const} . \quad (4.1)$$

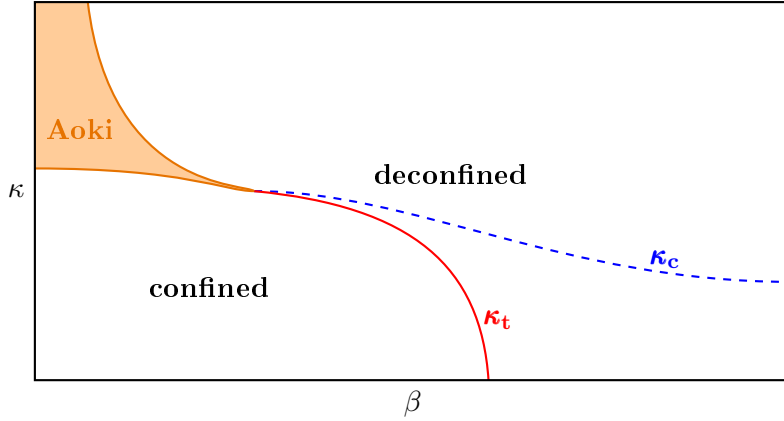


Figure 4.1.: Sketch of the Aoki phase and the finite temperature transition $\kappa_t(\beta)$ in (κ, β) space for standard Wilson fermions. $\kappa_c(\beta)$ indicates the critical hopping parameter for a massless theory.

However, since this is a tree-level prediction, it is clear that distortions due to cutoff effects might be large. Going further, one can use the corresponding formula derived in next-to-leading order chiral perturbation theory [139, 43],

$$m_{\pi^\pm}^2 = M' + \frac{16}{f^2} \left((2L_{68} - L_{45})(M')^2 + M' \hat{a} \cos(\omega)(2W - \tilde{W}) + 2\hat{a}^2 \cos^2(\omega)W' \right) + \frac{(M')^2}{2\Lambda_\chi^2} \ln \left(\frac{M'}{\Lambda_R} \right), \quad (4.2)$$

where $M' = \sqrt{\hat{\mu}^2 + (\hat{m}')^2}$, $\hat{a} = 2W_0 a$ and $\hat{\mu} = 2B_0 Z_\mu \mu_0$, $\hat{m}' = 2B_0 Z_m (m_0 - m_c)$. The W 's and L 's as well as B_0 can in principle all be fixed by fitting lattice chiral perturbation theory to zero temperature simulation results. For our purposes we can take them from literature [43, 139, 140] where they are mostly known by order of magnitude,

$$W, \tilde{W}, W' \sim 1/(4\pi)^2, \quad (4.3a)$$

$$W_0 \sim \Lambda_{QCD}^3, \quad (4.3b)$$

$$a\Lambda_\chi = 4\pi a f \approx 0.068, \quad (4.3c)$$

$$a\Lambda_R = 4\pi a f \approx 0.065, \quad (4.3d)$$

$$2L_{68} - L_{45} \approx -4 \cdot 10^{-4}. \quad (4.3e)$$

All remaining quantities, needed for renormalisation, are known from ETMC [141]. Once all parameters are fixed, equation (4.2) constitutes lines of constant mass for given pion mass and lattice spacing.

4.1.2. Comparison to Simulations

The simulation results on which we report in the following have been published in [29]. The investigations in the weak coupling regime have been performed on the APENext of INFN in Rome with a tree-level Symanzik improved gauge action and a lattice size $16^3 \times 8$. As discussed in [29] for strong couplings $\beta \lesssim 3.0$ the Aoki phase is found whereas

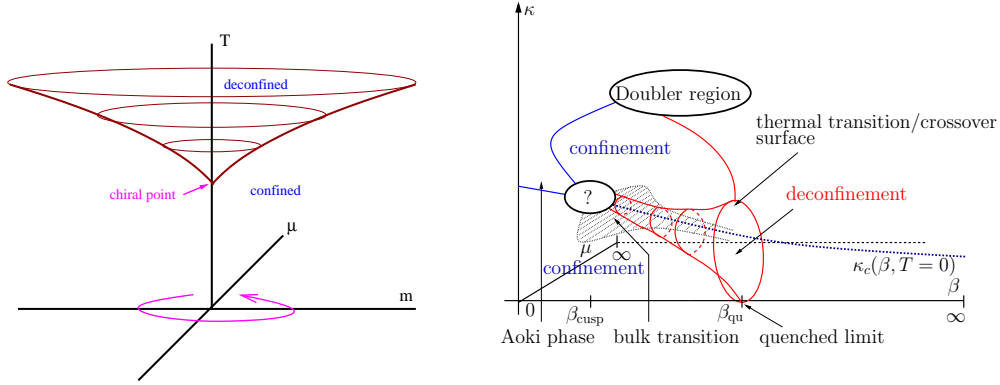


Figure 4.2.: Sketch of the thermal transition surface. Left: Thermal transition surface from a rotation in the mass plane (from [138]). Right: Schematic view of the conjectured cone. (from [29])

for intermediate couplings $\beta \approx 3.4$ metastabilities are observed that are interpreted as remainders of the zero temperature surface of unphysical bulk transitions, cf. also the zero temperature situation depicted in figure 3.3. For $\beta \gtrsim 3.65$ the phase structure is dominated by the thermal transition. We now discuss the last region in more detail as this thesis' contribution is focused there. It also is the region relevant for approaching physical questions in the context of the thermal transition and the continuum limit.

The analysis of the numerical data is based on the plaquette and real part of the Polyakov loop, their respective susceptibilities and the pion norm. For details on the observables, see section 5.2. In spite of the quite reasonable statistics of typically $\mathcal{O}(15\text{ k})$ the results remain somewhat noisy and qualitative. We interpret this as a signal of a soft crossover rather than a sharp transition. A further reason lies in the fact that for simulations close to the axis $\mu_0 = 0$ and $\kappa > \kappa_c$ the spectrum of the Dirac operator is shifted in the negative real direction, thus implying the occurrence of very small eigenvalues [142].

What we present here in detail is a set of scans in the hopping parameter κ across its critical value at fixed $\beta = 3.75$ where we have identified a slice of the conjectured cone, i. e. while varying κ we find entrance to and exit from the deconfined region inside the cone. This can be seen in figure 4.3, left, where the real part of the Polyakov loop is shown for increasing values of μ_0 . The rise and fall of the Polyakov loop indicate the change from confinement to deconfinement and vice versa. Whereas the qualitative behaviour remains unchanged, the two transitions for $\kappa < \kappa_c$ and $\kappa > \kappa_c$ should approach each other for increasing μ_0 . Finally, the ellipse's largest extent is reached and the transition accordingly lost, which can be seen in figure 4.3, left for the largest masses $a\mu_0 = 0.025, 0.035$.

For the Polyakov loop and plaquette susceptibilities as well as from the mass dependence of the pion norm we expect peak signals for the thermal transition in κ -scans. Whenever those signals are adequate, we have obtained values for κ_t , see table B.1 in the appendix. For signals from more than one observable, they are always mutually consistent. Thus we have used the best signal in each case for a rather qualitative com-

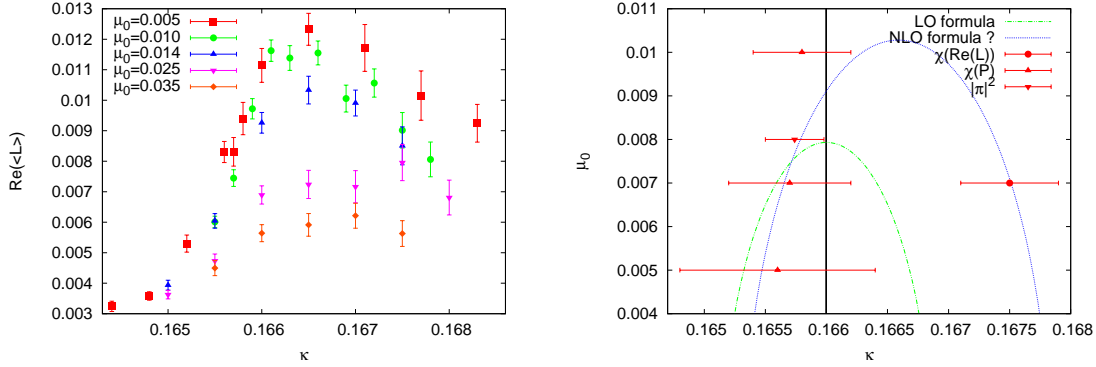


Figure 4.3.: Left: The real part of the Polyakov loop for different values of μ_0 . For $a\mu_0 \geq 0.025$ the transition is lost. Right: Data points represent the phase boundary at $\beta = 3.75$, estimated from the peaks of susceptibilities. The leading order formula equation (4.1) cannot fit the data, the NLO-formula, equation (4.2), contains constants that are only known by order of magnitude but is capable of describing the numerically found structure. The vertical line marks maximal twist. Both plots show results at $\beta = 3.75$. (as published in [29])

parison of equations (4.1) and (4.2), see figure 4.3, right. Obviously, the leading order formula (4.1) is not capable of describing the data. The generic problem lies in the fact that the tree-level formula always places the cusp of the ellipse at κ_c which does not allow for a correct description of our data.

On the other hand, making some rough assumption about the unknown constants in equation (4.2), it is possible to describe the data using that formula. This leads to our conclusions drawn in [29], that the Creutz scenario of a conical surface of thermal transitions widening towards the continuum limit as sketched in figure 4.2 is indeed realised.

As a supplement, we show scans in κ for different values of β at $a\mu_0 = 0.005$ in figure 4.4 that are published in [29] (and have been obtained previous to this thesis' work). The same double signal is repeated for the different β values, where only the range for the scan at $\beta = 3.9$ is not large enough to include the second transition. Moreover, the larger the lattice coupling the wider the deconfined region, which agrees perfectly with the expectation .

This understanding of the bare parameter phase space of finite temperature twisted mass QCD is the foundation for the simulations presented in chapter 5. On the one hand, we know how the thermal transition appears in the bare parameter phase space allowing for simulations at maximal twist by varying the lattice coupling. On the other hand, it has become clear that in the range of lattice spacings that are accessible from the ETMC vacuum information [23] finite temperature simulation are not affected by the unphysical bulk transitions.

4.2. Weak Coupling Limit

In this section, we discuss our study of the fermionic contribution to the pressure in the weak coupling limit [31]. This regime can be used to obtain information on the leading order cutoff effects and thus the degree of improvement at finite temperature.

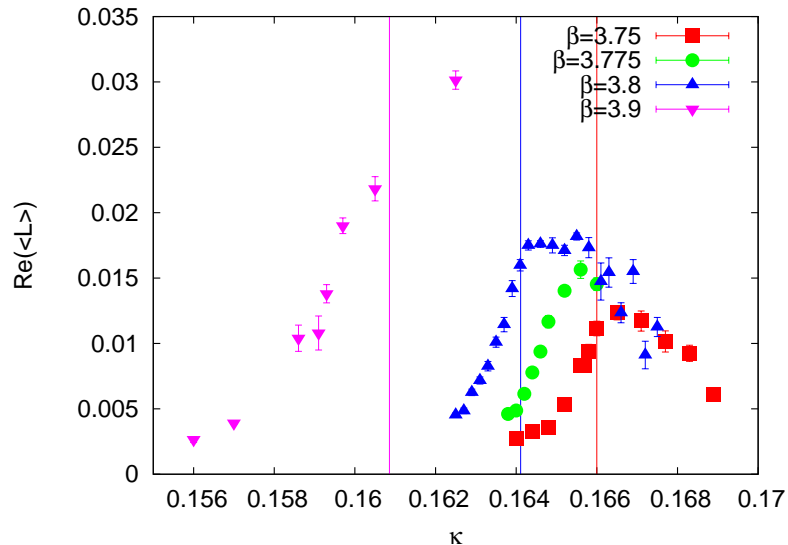


Figure 4.4.: Real part of the Polyakov loop for different values of β at $a\mu_0 = 0.005$. Rise and fall of the expectation value indicate entrance to and exit from the deconfined phase. (as published in [29])

Improvement is particularly important for studies of the QCD equation of state at finite temperatures since the pressure and related thermodynamic quantities are heavily affected by discretisation effects, $p \sim a^4$.

We start with a discussion of the free pressure and the effects due to a finite quark mass. Earlier perturbative investigations of the pressure at high temperature on the lattice had been restricted to the ideal gas and chiral limits, cf. [143] and references therein. Thus unlike in the zero temperature and tree-level case [122, 123], there are no earlier perturbative studies that consider a twisted mass at finite temperature. Most importantly, for the free pressure it is possible to disentangle the coefficients for the different contributions to the expansion in powers of the lattice spacing a .

In the second part of this section, we expand the investigation to the leading corrections due to interactions, i. e. to $\mathcal{O}(g^2)$. This second part originates mainly from work previous to this thesis and can be understood to supplement our analytical investigation at tree-level. The fermion actions that are compared are the standard, maximally twisted mass and clover improved Wilson action as well as the standard staggered action. The leading cutoff effects of the latter three should be of $\mathcal{O}(a^2)$, whereas standard Wilson fermions have $\mathcal{O}(a)$ effects introduced by finite quark mass. To compare the Wilson type fermions with staggered fermions, formulae from [144] are used.

4.2.1. Ideal Gas

As is well known, the thermodynamic pressure is determined by the logarithm of the partition function as $p = (\beta V)^{-1} \ln Z$ [34]. The contribution of $N_f = 2$ free Wilson or

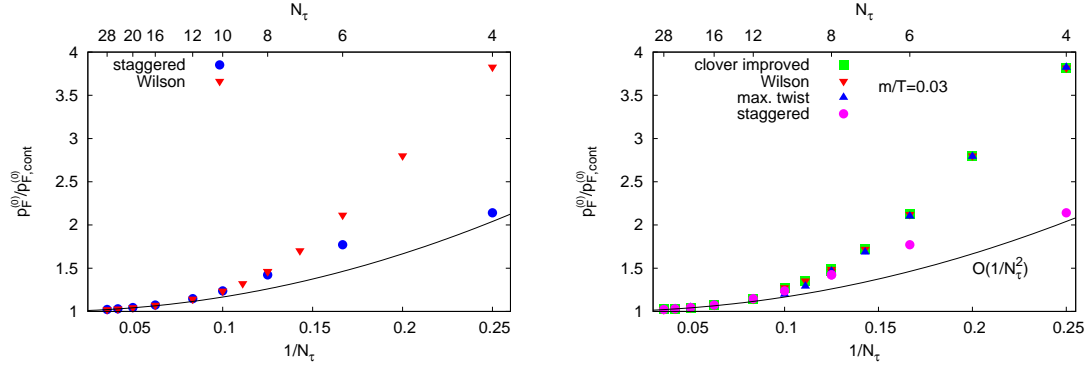


Figure 4.5.: Stefan-Boltzmann limit normalised to the continuum result. The solid line is the analytic $\mathcal{O}(1/N_\tau^2)$ prediction. Left: Massless quarks. Right: $m_R/T = 0.03$, where the quark mass is the standard mass for staggered and Wilson fermions. For maximally twisted mass fermions it is determined by the twisted mass parameter μ_0 whereas for clover improvement an $\mathcal{O}(a)$ shift in the bare mass is needed. (as published in [31])

twisted mass fermions to the ideal gas is immediately obtained as

$$\frac{p_F^{(0)}}{T^4} = 4(aN_\tau)^4 N_c \int_{[-\frac{\pi}{a}, \frac{\pi}{a}]^3} \frac{d^3 p}{(2\pi)^3} \left(\frac{1}{aN_\tau} \sum_{n=0}^{N_\tau-1} \ln (|G(\mathbf{p}, -\omega_n)|^2 + (a\mu_0)^2) - \int_{-\pi/a}^{\pi/a} dp_4 \ln (|G(\mathbf{p}, p_4)|^2 + (a\mu_0)^2) \right), \quad (4.4)$$

with the fermionic Matsubara modes $\omega_n = (2n+1)\pi/(aN_\tau)$, and the inverse propagator $|G(p)|^2 = \bar{p}^2 + (am_0 + \frac{1}{2}\hat{p}^2)^2$. As usual divergent vacuum pressure has to be subtracted. In order to evaluate the above integrals numerically, we evaluate the corresponding sums for finite volume explicitly, finding that a smooth extrapolation to the thermodynamic limit can be done.

Cutoff effects for the free gas are obtained by comparison with the continuum Stefan-Boltzmann or ideal gas limit,

$$\frac{p_{SB}}{T^4} = \frac{7N_c}{2} \left(\sum_f \frac{360}{7\pi^4} \int_{m_f/T}^{\infty} dx x \sqrt{x^2 - (m_f/T)^2} \ln(1 + e^{-x}) \right) \frac{\pi^2}{90}. \quad (4.5)$$

For massless fermions, the expression in brackets gets replaced by the number of flavours N_f (cf. also [145]).

The mere numerical integration of equation (4.4) does not allow to identify the separate contributions order by order in the lattice spacing. To achieve this, an analytical approach is mandatory. In [143] the integral (4.4) for massless quarks has been expanded into a power series in $1/N_\tau$ by means of contour integration and neglecting finite volume

effects,

$$\begin{aligned} \frac{p}{T^4} &= \frac{(aN_\tau)^3}{2\pi^3} N_c \int_{\mathbb{R}^3} d^3k \ln \left(1 + e^{-N_\tau a E(\mathbf{k}, m)} \right) \\ &= \frac{p^{(a^0)}(m)}{T^4} + \frac{p^{(a^1)}(m)}{T^4} \frac{1}{N_\tau} + \frac{p^{(a^2)}(m)}{T^4} \frac{1}{N_\tau^2} + \dots \end{aligned} \quad (4.6)$$

This establishes a direct correspondence of cutoff effects in the dispersion relation $E(\mathbf{p}, m)$ to those in the pressure. In fact, improvement in the dispersion relation, which is a vacuum quantity, directly leads to improvement for the pressure at finite temperature.

Remarkably, for massless quarks, the coefficients $\frac{p^{(a^2)}}{T^4}$ and $\frac{p^{(a^4)}}{T^4}$ can be calculated explicitly [143] and are the same for standard staggered and Wilson type fermions. Differences between these discretisation schemes are only introduced in higher orders of the lattice spacing. We have repeated this procedure for massive fermions. In this case, one is left with one-dimensional integrals for the expansion coefficients depending on the quark mass,

$$\frac{p^{(a^0)}(m)}{T^4} = \frac{2N_c}{\pi^2} \int_0^\infty dy y^2 \ln \left(1 + e^{-\varepsilon_{(0)}(y, m/T)} \right), \quad (4.7a)$$

$$\frac{p^{(a^1)}(m)}{T^4} = -\frac{2N_c}{\pi^2 N_\tau} \int_0^\infty dy y^2 \frac{\varepsilon_{(1)}(y, m/T)}{1 + e^{\varepsilon_{(0)}(y, m/T)}}, \quad (4.7b)$$

$$\begin{aligned} \frac{p^{(a^2)}(m)}{T^4} &= \frac{N_c}{\pi^2 N_\tau^2} \int_0^\infty dy y^2 \frac{\varepsilon_{(1)}^2(y, m/T) e^{\varepsilon_{(0)}(y, m/T)}}{\left(1 + e^{\varepsilon_{(0)}(y, m/T)} \right)^2} \\ &\quad - \frac{N_c}{\pi^2 N_\tau^2} \int_0^\infty dy \int_0^\pi d\vartheta y^2 \sin(\vartheta) \frac{\varepsilon_{(2)}(y, \vartheta, m/T)}{1 + e^{\varepsilon_{(0)}(y, m/T)}}, \end{aligned} \quad (4.7c)$$

where

$$\varepsilon(\mathbf{p}/T, m/T) = \varepsilon_0(|\mathbf{p}|/T, m/T) + \varepsilon_1(|\mathbf{p}|/T, m/T) \frac{1}{N_\tau} + \varepsilon_2(|\mathbf{p}|/T, \vartheta, m/T) \frac{1}{N_\tau^2} + \dots \quad (4.8)$$

can be determined from the dispersion relation $E(\mathbf{p}, m)/T = \varepsilon(\mathbf{p}/T, m/T)$. Details are explained in appendix C.1; especially equation (4.7c) can also be cast to a one-dimensional integral. The remaining integrations can easily be performed numerically, cf. figure 4.6.

We begin the discussion of results with figure 4.5, where the fermionic contribution to the free pressure on the lattice is shown normalised to the continuum one. The chiral limit is reproduced from [143] for comparison on the left. In this case there is no difference between the Wilson formulations. Even though in the chiral limit the leading cutoff effects are found to be identical for both types of discretisation, staggered fermions show a more rapid convergence to the continuum than Wilson fermions, which is caused by higher order corrections. The comparison of the numerical values to the

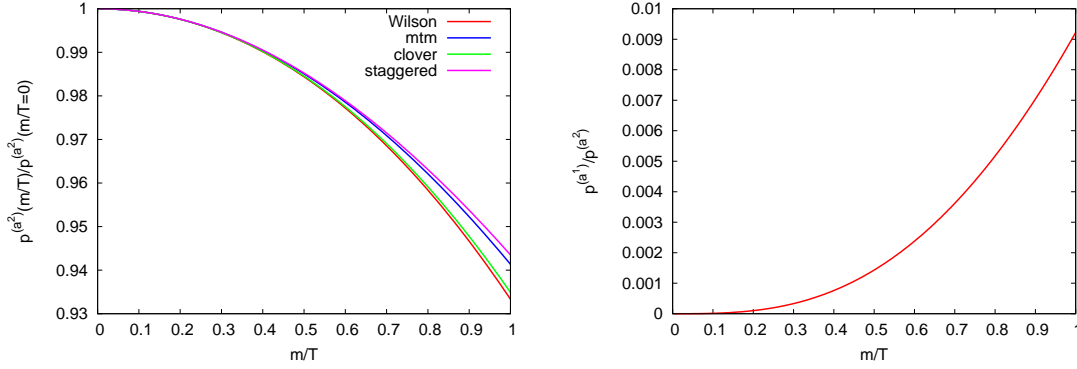


Figure 4.6.: Leading orders of cutoff effects for different types of fermions. Left: Mass dependence of the $\mathcal{O}(a^2)$ contribution to the pressure. Right: Comparison of the $\mathcal{O}(a)$ and $\mathcal{O}(a^2)$ expansion coefficients for the pressure series in $1/N_\tau$. (as published in [31])

analytical formula to $\mathcal{O}(a^2)$, which is depicted by the solid line in figure 4.5, reveals that the $\mathcal{O}(a^2)$ effects are only dominant for lattices with $N_\tau \gtrsim 12$.

As expected from the dispersion relation (3.37), switching on a mass increases the cutoff effects for Wilson fermions to $\mathcal{O}(a)$ although the effect is very weak. Massive staggered fermions keep scaling as $\mathcal{O}(a^2)$. Figure 4.5, right, shows that finite mass effects for a reasonable value of $m_R/T = 0.03$ are rather small. We use the notion of a renormalised quark mass although we are at the non-interacting level in order to account for the shift in the clover quark mass (3.19a). Note also that for maximally twisted mass fermions, m_R is solely determined by the twisted mass parameter.

In figure 4.6, we present the mass dependence of the leading order contributions obtained from the analytical approach. Up to large quark masses the differences between the $\mathcal{O}(a^2)$ contributions for the different fermion formulations as well as the deviation from the massless case are very small (see figure 4.6, left). Furthermore, the $\mathcal{O}(a)$ contribution to pure Wilson fermions is almost negligible when compared to the one of $\mathcal{O}(a^2)$ (see figure 4.6, right). This will only change on very fine lattices, $N_\tau^{-1} \lesssim 1/100$.

4.2.2. Two-loop Contribution

Turning to the interacting theory, the leading $\mathcal{O}(g^2)$ corrections to the fermionic pressure due to interactions have been calculated in the diploma thesis [134], cf. also [31]. The one-loop pressure contributes due to mass renormalisation. Twisted mass fermions and ordinary Wilson fermions can be treated simultaneously using the propagator given in equation (3.28) with identical vertices from the standard Wilson action. We use the expressions as given in [62] with the gauge propagator from the Wilson plaquette action. The resulting integrals need to be solved numerically, a task that has been achieved in our study [31] using integration routines of the CUBA-library [146]. Unfortunately, the difference between the finite N_τ and the vacuum contributions, which is the quantity of interest, shrinks rapidly $\sim 1/N_\tau^4$ and for $N_\tau = 8$ is only about 6% of the numerically evaluated integrals, rendering an accurate evaluation difficult. In any case, in order to extract cutoff effects we need the continuum corrections to the free pressure which have been calculated in [34, 147].

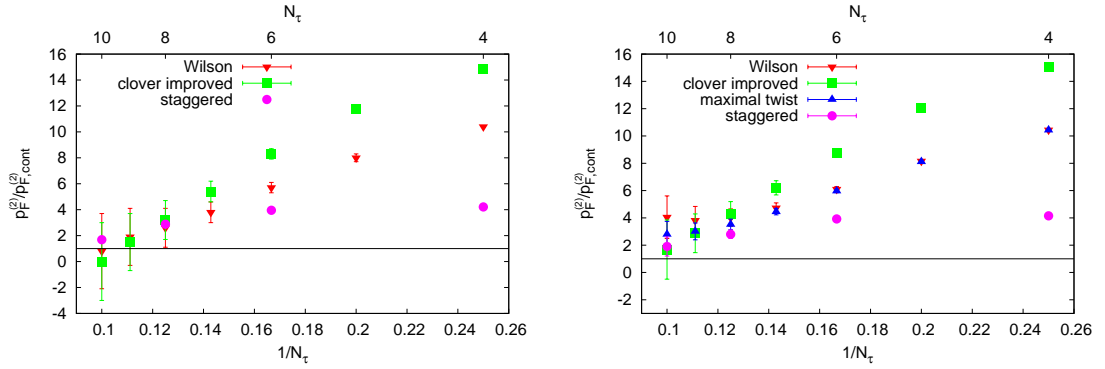


Figure 4.7.: Two-loop contribution to the pressure normalised to the continuum result. Left: Massless fermions. Right: Massive case with $m_R/T = 0.03$. (as published in [31])

The behaviour of the two-loop contribution is shown in figure 4.7, the chiral limit on the left. As in the non-interacting case, staggered fermions have smaller cutoff effects on coarse lattices. Comparing the scales of figure 4.7 and figure 4.5 interactions indeed appear to increase this difference. However, also for staggered fermions a^2 -scaling does not set in until $N_\tau \geq 8$ at least, where the cutoff effects of the Wilson discretisations are comparable.

The right panel of figure 4.7 shows the two-loop results for a non-vanishing renormalised quark mass $m_R/T = 0.03$. Despite the rather large numerical uncertainties, one finds a qualitative correspondence to the one-loop case, figure 4.5, right. This correspondence applies especially to the small dependence on the quark mass and the particular discretisation. As in the free case, on lattices $N_\tau \geq 8$ Wilson fermions are found to be competitive with staggered fermions in terms of the size of cutoff effects. However, a^2 -scaling is not observed for any of the discretisations before $N_\tau \gtrsim 10$. Up to that, $\mathcal{O}(a)$ effects for unimproved Wilson fermions are negligible as can be seen from comparison to the maximally twisted mass fermions. Note that the absolute size of the cutoff effects for the unimproved action appears smaller than for the clover action. This indicates significantly higher order contributions for the N_τ considered here.

Approaching T_c from the high temperature limit, perturbation theory will become inapplicable. However, for the perturbative expansion this indicates that higher order terms become more and more important. Therefore, given the qualitative correspondence between one-loop and two-loop results, our analysis suggests that, for simulations near T_c , $\mathcal{O}(a)$ -improved Wilson fermions scale comparably to standard staggered fermions for fine enough lattices, $N_\tau \geq 8$. However, independent of the improvement scheme chosen, a^2 -scaling appears to set in only on lattices $N_\tau > 10$.

5. Thermal Transition for Two Quark Flavours

In this chapter we present simulations with $N_f = 2$ maximally twisted mass fermions and the corresponding analysis in search for the thermal transition of QCD. We discuss the possible impact of our results on the knowledge of the transition in the two flavour chiral limit.

As already noted in the introduction, it is well established that the QCD phase transition for physical quark masses is really a continuous crossover [17]. However, for simulations of lattice QCD the nature of the transition for varying quark masses is of particular importance since a direct access to the physical point is often not feasible. This is especially true for Wilson type fermions. For our case of a degenerate quark doublet and maximally twisted mass simulation, ETMC have not reached pion masses below 280 MeV [23]. Moreover, knowledge about the phase transition in the two flavour chiral limit influences the understanding of global properties of the phase diagram in an enlarged phase space where additionally chemical potential is taken into account [148].

Despite all efforts, the nature of the transition in the two flavour chiral limit is still a question which has not been completely settled. Most investigations have concluded a second order transition [105, 149, 150, 151, 152, 153] but there are also claims for a first order scenario [154, 155, 156]. According to the prediction by Pisarski and Wilczek [41] one of the two scenarios must be realised. Their argument relies on the strength of the axial anomaly. If the anomaly remains strong enough close to the thermal transition, the symmetry breaking pattern for chiral restoration in the two flavour chiral limit corresponds to the one at zero temperature discussed in section 2.2,

$$SU_L(2) \times SU_R(2) \rightarrow SU_V(2) , \quad (5.1)$$

which would favour a second order transition in the $O(4)$ universality class. However, it is also possible for the anomaly to be sufficiently suppressed by thermal effects. In that case, the additional $U_A(1) \times U_V(1)$ symmetry has to be taken into account such that the breaking pattern turns out to be

$$U_L(2) \times U_R(2) \rightarrow U_V(2) \quad (5.2)$$

implying a first order transition similar to the three flavour chiral and pure gauge limits. For further discussion see [157].

Since it is not possible to perform simulations for zero quark mass, which is true even for staggered fermions that generally reach lighter masses than Wilson type fermions, the task for analyses based on lattice simulations is to find some way to extrapolate from relatively large pion masses in the crossover regime of thermal transitions to the chiral critical point. This is — at least in principle — possible since any critical point has some neighbourhood in which universal scaling behaviour is observable. One can

hope to access this scaling regime with the simulations and thus infer the universality class from comparison of scaling laws.

We start with a general discussion of universality in section 5.1 before we introduce our observables, section 5.2. This involves the chiral condensate as the order parameter of chiral symmetry breaking as well as gauge observables, in particular the Polyakov loop that indicates deconfinement.

In section 5.3 we present our simulation setup including the issues of scale setting and signal extraction. Section 5.4 is devoted to extracting information about the chiral limit from our data by utilising scaling properties of the order parameter. In section 5.5, we try to quantify the strength of the axial anomaly in the chiral limit. For this purpose we introduce screening masses and the corresponding integrated correlators as further observables. We also include a discussion of some of the properties of screening masses in the infinite temperature limit. Finally, section 5.6 contains a summary and discussion for our $N_f = 2$ maximally twisted mass simulations.

The presentation of our simulation setup as well as the analysis and considerations concerning the chiral limit accessed by scaling properties can also be found in a recent tmfT preprint [158].

5.1. Scaling Properties

Close to a second order critical point correlation lengths diverge so that microscopic properties of the underlying theory become unimportant and the dynamics are governed solely by some global properties such as symmetries and spatial dimension. This allows to classify very different physical systems according to their universality class. We refer to Fisher [159] for a general review on critical phenomena. A more recent overview including precise estimates for critical exponents has been given by Pelissetto and Vicari [160]. For QCD universality is important as it allows to extract some of its properties from theories such as spin models that can be treated more easily by analytical or numerical methods.

Scaling behaviour is determined by critical exponents. Important for the following analysis of $N_f = 2$ chiral QCD are in particular those that govern the order parameter M , i. e. β in the phase with broken symmetry and δ at critical temperature,

$$M \sim |\tau|^\beta, \quad (5.3a)$$

$$M \sim h^{1/\delta}. \quad (5.3b)$$

$\tau = (T - T_c)/T_c \sim \beta - \beta_c$ is the reduced temperature that can be related to the lattice coupling β as indicated and h is the external field which introduces an explicit symmetry breaking. In case of QCD it can thus be identified with the quark mass [151, 161]. Note that we now use β to name two different quantities, i. e. the lattice coupling and the critical exponent. Since both notations are well-established in the literature, we keep them here. What is really meant is clear in each case from the context.

A third exponent, γ , is important for possible future analysis based on finite size scaling, see e. g. [162], as it determines the divergence of the susceptibility $\chi = \partial M / \partial h$,

$$\chi \sim |\tau|^{-\gamma}. \quad (5.3c)$$

UNIVERSALITY	β	γ	δ	ν	Reference
3d Ising, $Z(2)$	0.3265(03)	1.2372(5)	4.789(02)	0.6301(04)	[160]
3d $O(4)$	0.3836(46)	1.477(18)	4.851(22)	0.7479(90)	[162]

Table 5.1.: Critical exponents for the two universality classes of interest.

For a finite lattice volume the partition function is completely regular being a trace over all degrees of freedom and thus a finite sum. Non-analyticities in the thermodynamic observables can only be recovered in the infinite volume limit. The approach to this limit close to critical points is known and can be used to identify the nature of the transition by means of finite size scaling. For the peak that is observed at finite volume, one has

$$\chi_{\max} \sim L^{\gamma/\nu} \quad (5.4)$$

for a second order critical point whereas the peak height for a crossover saturates to a finite value. In case of a first order transition the peak should grow linearly with the volume, $V = L^d$. A list of critical exponents for the universality classes of interest is shown in table 5.1.

The scaling of the order parameter is encoded in a universal scaling function, see e. g. [163],

$$M = h^{1/\delta} f(x), \quad (5.5)$$

with the scaling variable

$$x = \frac{\tau}{h^{1/(\delta\beta)}}. \quad (5.6)$$

An accurate numerical interpolation of the scaling function is known for the relevant case of $O(4)$ symmetry [164, 165]. From this scaling law it is possible to deduce the dependence of the pseudo-critical temperature on the field h [161]. To see this, one realises that also the susceptibility can be expressed by a scaling function,

$$\chi = \frac{\partial M}{\partial h} = h^{1/\delta-1} \left(\frac{1}{\delta} f(x) - \frac{1}{\delta\beta} x f'(x) \right) =: g(x). \quad (5.7)$$

The pseudo-critical temperature is defined to be the peak of the susceptibility as a function of temperature. Therefore, we need to find a scaling variable that satisfies

$$\frac{\partial g(x)}{\partial \tau} = g'(x) \frac{1}{h^{1/(\delta\beta)}} = 0. \quad (5.8)$$

For general h , the above relation can only be fulfilled by a constant value, i. e. $x = B$. Hence, using $\tau = \beta - \beta_c$,

$$\beta(h) = \beta_c + B h^{1/(\delta\beta)}. \quad (5.9)$$

With the proper scale setting and relying on the leading order of χ_{PT} , i. e. $m_\pi^2 \sim m_q$, the above relation can also be rewritten for the temperature $T_c(m_\pi)$ in physical units,

$$T_c(m_\pi) = T_c(0) + A m_\pi^{2/(\delta\beta)}. \quad (5.10)$$

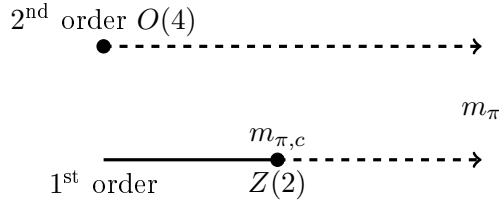


Figure 5.1.: Illustration of possible scenarios for the $N_f = 2$ chiral limit.

5.2. Observables

We present the observables relevant for our study of the thermal transition beginning with the chiral condensate in continuation of the last section. We then introduce the gauge observables, in particular the Polyakov loop that is sensitive to deconfinement.

5.2.1. Chiral Condensate

The most important observable for our analysis approaching the massless limit is the chiral condensate,

$$\langle \bar{\psi}\psi \rangle = \frac{T}{V} \frac{\partial \ln Z}{\partial m_q}, \quad (5.11)$$

that is the order parameter for chiral symmetry. Thus it can be associated with the magnetisation M of a spin model of the same universality class applying all the scaling properties presented in section 5.1.

If the anomaly is sufficiently strong to break the $U_A(1)$ symmetry, the universality class according to Pisarski and Wilczek is the three-dimensional $O(4)$. Also in case of a first order transition some kind of effective scaling behaviour can be expected [166]. More importantly, the first order scenario includes a second order endpoint in the 3d-Ising ($Z(2)$) universality class, cf. figure 5.1. In this case, one should thus encounter a situation that is dominated by $Z(2)$ -scaling for a critical point at finite quark mass when approaching the chiral limit from the crossover regime. A subtlety in the latter case is that for the critical point at finite mass no exact chiral symmetry of the action exists. Thus $\langle \bar{\psi}\psi \rangle$ is no longer an exact order parameter and the quark mass cannot be identified to be the symmetry breaking field. The induced uncertainty might be small as we could think of it as a perturbation due the small quark mass just like in chiral perturbation theory. Since our data are not accurate enough to catch such effects, we do not consider them for the rest of this work. They must, however, be kept in mind for future work with increased accuracy.

The appropriate quantity to locate the chiral phase transition is the chiral susceptibility,

$$\chi_\sigma = \frac{\partial \langle \bar{\psi}\psi \rangle}{\partial m_q}. \quad (5.12)$$

Evaluating the derivative with respect to the quark mass, one obtains two different contributions to χ_σ , see e. g. [150]. We neglect the piece that is proportional to $\langle \text{Tr } M^{-2} \rangle$, where M is the fermion determinant, and consider only the remaining part, which is

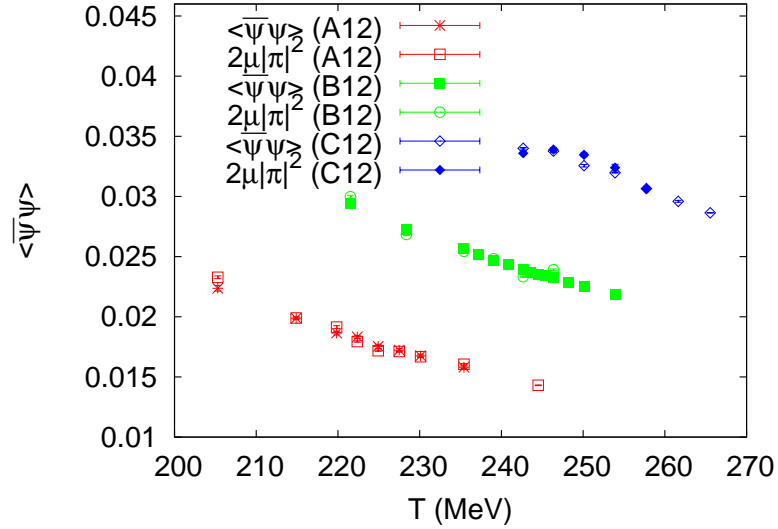


Figure 5.2.: Check for the consistency between $\langle \bar{\psi}\psi \rangle$ and $|\pi|^2$ by comparing the expectation values $\langle \bar{\psi}\psi \rangle$ and $2\mu_0|\pi|^2$ for our simulation runs.

the variance per configuration,

$$\sigma_{\bar{\psi}\psi}^2 = V/T \left(\langle (\bar{\psi}\psi)^2 \rangle - \langle \bar{\psi}\psi \rangle^2 \right). \quad (5.13)$$

This quantity shows a peak associated with the chiral transition. Moreover, it is expected to dominate the signal of χ_σ , see e. g. [167].

The pion norm,

$$|\pi|^2 = \sum_x \left\langle \bar{\psi}(x) \frac{1}{2} \gamma_5 \tau^+ \psi(x) \bar{\psi}(0) \frac{1}{2} \gamma_5 \tau^- \psi(0) \right\rangle, \quad (5.14)$$

is interesting for twisted mass simulations because its definition is independent of the twist angle. It is connected to the chiral condensate via a Ward identity,

$$2m_q |\pi|^2 = - \langle \bar{\psi}\psi \rangle, \quad (5.15)$$

which has been proven for twisted mass QCD by Frezzotti et al. [85].

The condensate that we have used for analysis has been calculated as $\langle \bar{\psi}\psi \rangle$ by our collaborators in Berlin from stochastic noisy estimators, cf. [86], on all available configurations. We have performed a double check by comparing these results to the pion norm. At least for the runs in Rome, B10 and C12 (see section 5.3), the two calculations are completely independent of each other. Most importantly, the code in Rome performs the calculation of the pion norm with point sources. In any case, pion norm and $\langle \bar{\psi}\psi \rangle$ can be used to check for consistency since they describe the same physical quantity based on different operators. We show corresponding checks in figure 5.2 and figure 5.3.

Note that we use the unrenormalised $\langle \bar{\psi}\psi \rangle$ which is related to the renormalised chiral condensate by both multiplicative and additive renormalisation [85]. The additive

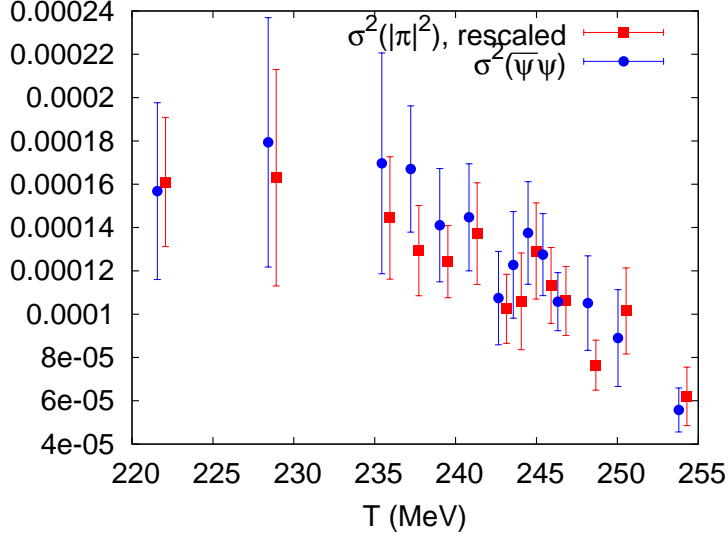


Figure 5.3.: Check with B12 data for the consistency between the variances of $\langle\bar{\psi}\psi\rangle$ and $|\pi|^2$ where the latter one has been rescaled by a constant factor.

renormalisation is proportional to the mass and affects scaling violations — if present — only quantitatively, cf. [105]. Therefore a scaling analysis based on our $\langle\bar{\psi}\psi\rangle$ is perfectly admissible if we keep N_τ fixed.

5.2.2. Gauge Observables

The gauge observables that we consider are the traced plaquette

$$P = \frac{1}{6N_c N_\tau N_\sigma^3} \text{ReTr} \sum_x \sum_{\mu > \nu} U_\mu(x) U_\nu(x + \hat{\mu}) U_\mu^\dagger(x + \hat{\nu}) U_\nu^\dagger(x) \quad (5.16)$$

and the real part of the Polyakov loop, i. e. the real part of

$$L = \frac{1}{N_c} \frac{1}{N_\sigma^3} \text{Tr} \sum_{\mathbf{x}} \prod_{x_4=0}^{N_\tau-1} U_4(\mathbf{x}, x_4) . \quad (5.17)$$

Along with the above observables, we look at their susceptibilities,

$$\chi_O = N_\sigma^3 \left(\langle O^2 \rangle - \langle O \rangle^2 \right) . \quad (5.18)$$

The Polyakov loop is of particular interest since it is the order parameter of the pure gauge deconfinement transition. This transition is related to the breaking of centre symmetry [168]. The transformation for this symmetry is given by

$$U_\mu(x) \rightarrow e^{i2\pi/3n} \mathbf{1}_{SU(N_c)} U_\mu(x) , \quad n \in \mathbb{N} , \quad (5.19)$$

where the factor multiplying the link is from the centre of $SU(N_c)$, i. e. from

$$C(SU(N_c)) = \{z \in SU(N_c) \mid \forall U \in SU(N_c) : zUz^{-1} = U\} . \quad (5.20)$$

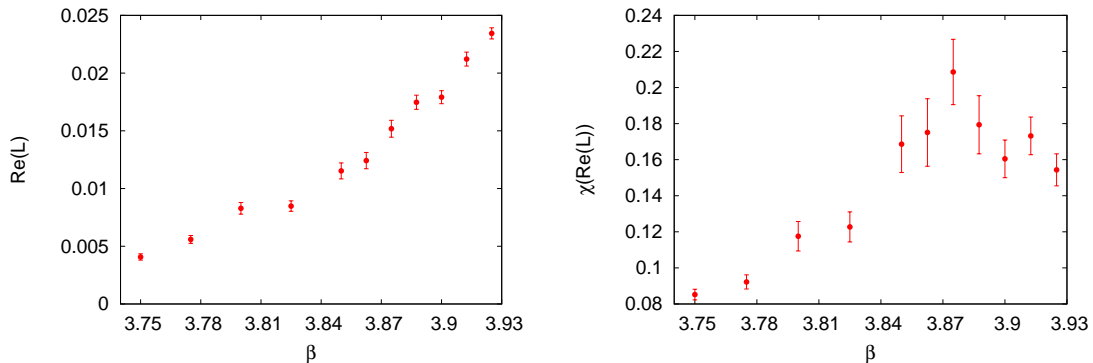


Figure 5.4.: Real part of the Polyakov loop (left) and its susceptibility (right) at $a\mu_0 = 0.040$ for $\kappa_c(\beta)$ on a lattice of extent $16^3 \times 8$.

The gauge action itself is invariant under centre transformations but the Polyakov loop picks up a phase factor. Thus for unbroken centre symmetry the Polyakov loop expectation value has to vanish, which corresponds to confinement. In the high temperature phase where the Polyakov loop is non-zero, centre symmetry is accordingly broken. The connection to confinement can be read off easily from the relation to the quark free energy,

$$\langle |L| \rangle \sim e^{-\beta(F_q - F_0)}. \quad (5.21)$$

F_0 is the necessary vacuum subtraction. In case of perfect confinement, a single quark acquires an infinite free energy such that $\langle |L| \rangle = 0$. Note that the explicit centre symmetry breaking for small quark masses is so severe for the volumes relevant to our studies that out of the three possible phases for L only the one on the real axis as dictated by the quark mass persists. Therefore it is sufficient to use the real part of the Polyakov loop as the quantity signalling confinement for our simulations.

5.3. Simulations

Our dynamical $N_f = 2$ simulations of twisted mass fermions at maximal twist have been performed on lattices with temporal extent $N_\tau = 10, 12$ and spatial size $N_\sigma = 32$. The lattice spacings were in the range $0.06 - 0.08$ fm. With pion masses between 300 and 500 MeV we have thus $m_\pi L \sim 3 - 5$. The gauge action was tree-level Symanzik improved and all necessary vacuum information have been taken from ETMC [23].

Our strategy is based on scans in β which amount to a variation of temperature $T = (a(\beta)N_\tau)^{-1}$ for a pion mass that is determined solely by the twisted mass parameter μ_0 . We have tested this strategy on smaller lattices with $N_\tau = 8, N_\sigma = 16$ and larger masses $a\mu_0 = 0.025, 0.040$ [90]. These masses correspond to pion masses of roughly 800 MeV – 1 GeV. For $a\mu_0 = 0.040$ we show the Polyakov loop and its susceptibility in figure 5.4. The resulting pseudo-critical point can be identified very well from the peak of $\chi(\text{Re}(L))$ and gives a temperature in the range of the pure gauge transition, $T_c \lesssim 300$ MeV.

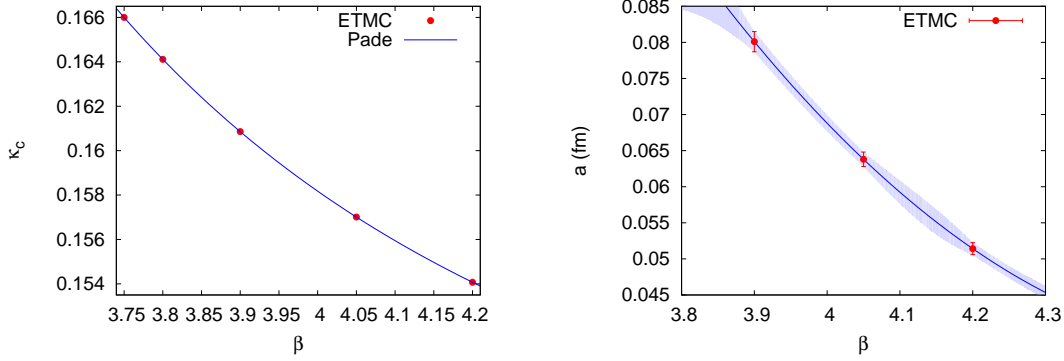


Figure 5.5.: Left: Interpolation for the critical hopping parameter, $\kappa_c(\beta)$. Right: Interpolation of the lattice spacing as a function of the coupling

5.3.1. Setup

In order to be able to perform β -scans at maximal twist, we need to interpolate the values of κ_c given by ETMC, see figure 5.5, left. We have resorted to a Padé approximation that is rather robust in the sense that it can be replaced by different Padés or even a polynomial without changing the resulting values. The Padé for κ_c can be found in appendix D.1 along with the ETMC values.

For the interpolation of the lattice spacing we use the values ETMC give based on the combined fits to their data [23],

$$a(\beta = 3.90) = 0.0801(14) \text{ fm} , \quad (5.22a)$$

$$a(\beta = 4.05) = 0.0638(10) \text{ fm} , \quad (5.22b)$$

$$a(\beta = 4.20) = 0.05142(83) \text{ fm} . \quad (5.22c)$$

The interpolation is done using a quadratic polynomial. The error bars are determined from the according interpolations of upper and lower bounds, see figure 5.5, right. There are also estimates for lattice spacings available at $\beta = 3.8$ (0.0998(19) fm) and at 3.75 (~ 0.1 fm, from personal communication with K. Jansen) which can be used to check the reliability of our formula even for somewhat coarser lattices. However, any smaller value of β can only be related to a lattice spacing in physical units by a very crude extrapolation.

Finally, the pion mass is needed. Calculating m_π from the twisted mass parameter $a\mu_0$ at the couplings used by ETMC can be done using their χ PT formulae. For a β -scan these points need to be interpolated. We have chosen the ansatz to use one of the existing values of $a\mu_0(\beta)$ to fix the only free parameter in the one-loop relation,

$$a\mu_0(\beta) = C \exp\left(-\frac{\beta}{12\beta_0}\right) , \quad (5.23)$$

and determine the line $a\mu_0(\beta)$ for the given pion mass from it. Since our simulations are always restricted to a relatively small range of lattice couplings in the regime close to T_c this approach works very well. Figure 5.6 shows a check for $m_\pi = 316$ MeV. The starting point is $\beta = 3.9$, the simulations are performed for $3.9 \lesssim \beta < 4.05$.

RUN	$N_\sigma^3 \times N_\tau$	RANGE	m_π (MeV)
A12	$32^3 \times 12$	$3.900 \leq \beta \leq 4.015$	316(16)
B12	$32^3 \times 12$	$3.950 \leq \beta \leq 4.050$	398(20)
C12	$32^3 \times 12$	$4.010 \leq \beta \leq 4.090$	469(24)
B10	$32^3 \times 10$	$3.850 \leq \beta \leq 3.930$	398(20)

Table 5.2.: Naming scheme for our scans in β . See text for further explanations.

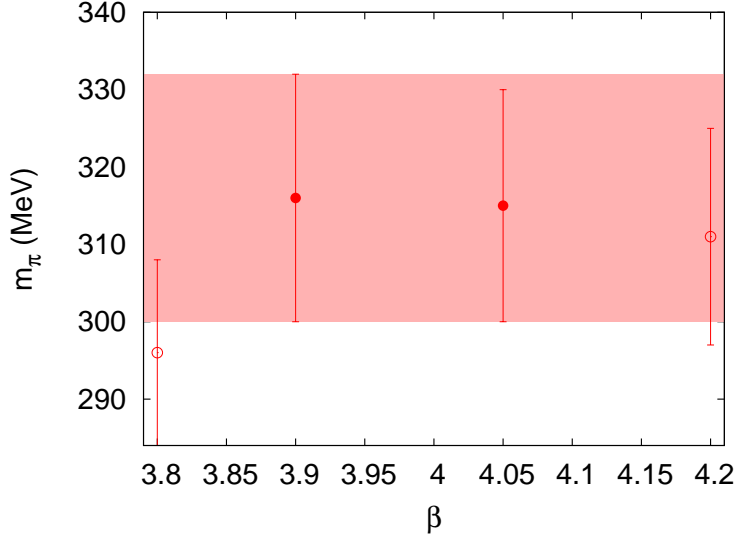


Figure 5.6.: Check of estimated values of $a\mu_0$ for a line of constant pion mass $m_\pi = 316(16)$ MeV. Our line $a\mu_0(\beta)$ is based on the point at $\beta = 3.9$ according to equation (5.23). The pion masses at $\beta = 3.8, 4.05$ and 4.2 have been calculated using the corresponding $a\mu_0(\beta)$ as input for the relation given by ETMC at these couplings.

Altogether, we have simulated with three different pion masses. For the sake of simplicity we have introduced the naming scheme presented in table 5.2. The masses 316(16), 398(20) and 369(24) MeV have been labelled A, B, C respectively. For all masses we have results on $N_\tau = 12$, for the intermediate mass there is also a simulation at $N_\tau = 10$ available.

5.3.2. Signal Extraction

For the susceptibilities and variances of our data, we find the signals for the transition to be rather weak and noisy, which is probably related to the fact that we are merely probing a very soft crossover in our range of pion masses. To illustrate this assumption, we show a set of scatter plots for the Polyakov loop along with histograms of $\text{Re}(L)$ in figure 5.7 for run A12 that indicate a very smooth transition. Scatter plots and histograms for the remaining runs as well as additional information are collected in appendix D.2.

In order to get an estimate for the pseudo-critical coupling β_c , we fit the peak of the susceptibilities to Gaussians. Although the shape of the critical region for the different

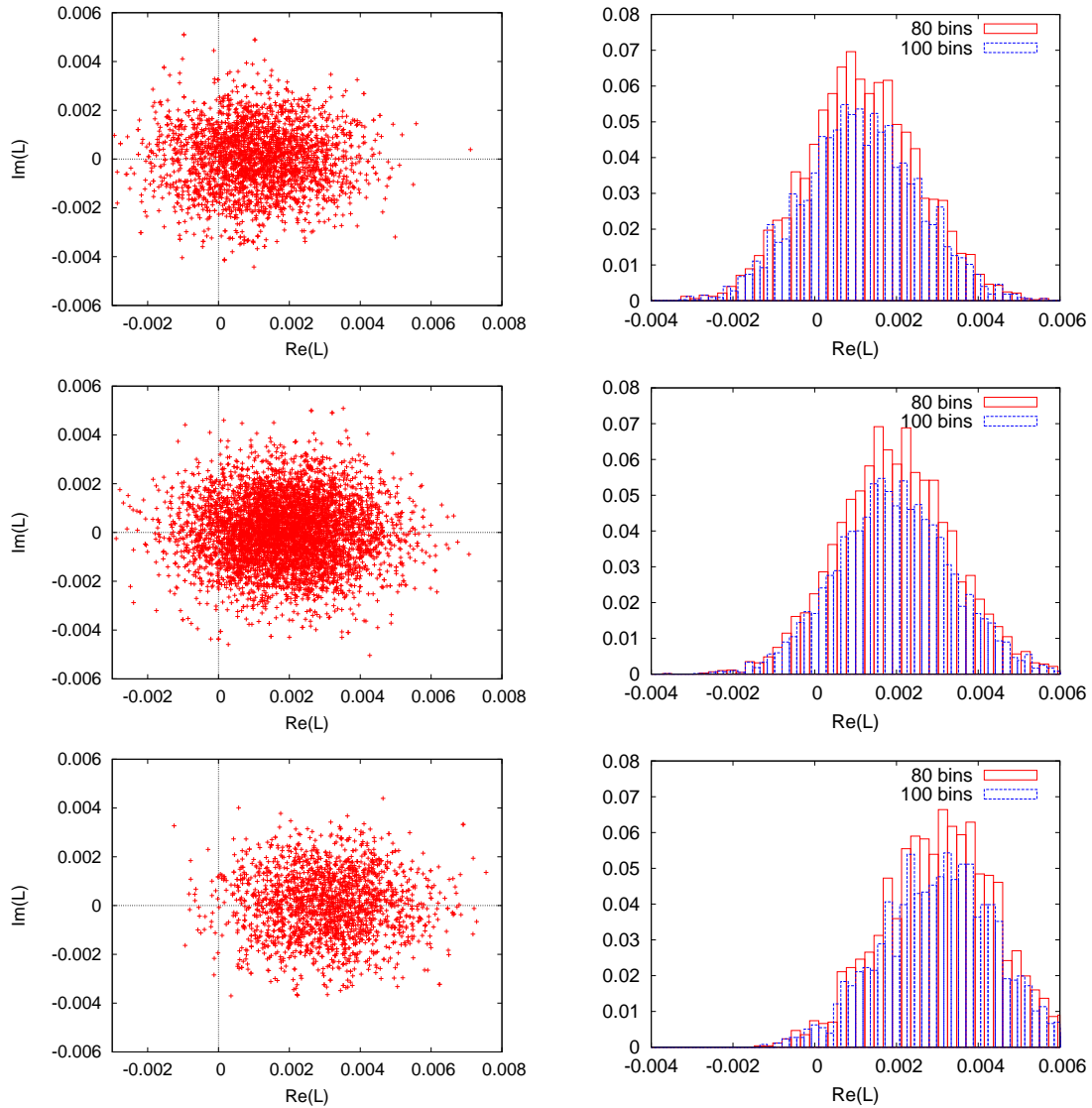


Figure 5.7.: Scatter plots for $\text{Im}(L)$ vs. $\text{Re}(L)$ (left) and histograms for $\text{Re}(L)$ (right) from run A12. From top to bottom we show the plots for the smallest value of β in our simulation, 3.900, one close to the identified transition, 3.960 and the largest value, 4.015.

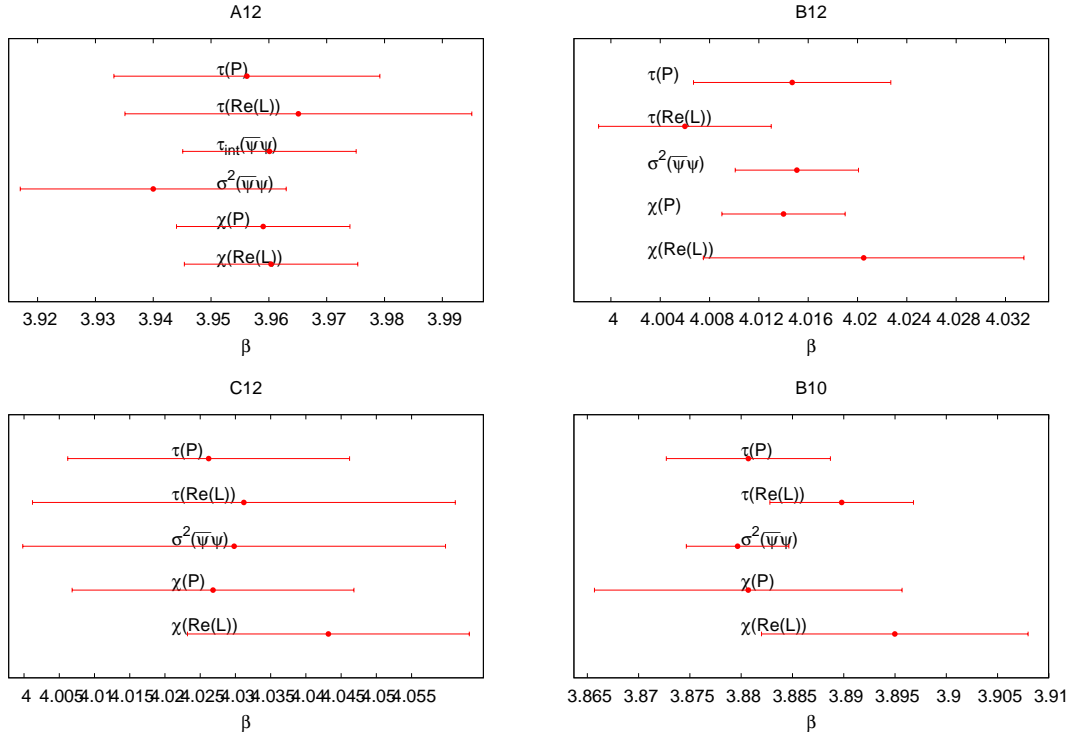


Figure 5.8.: Comparison of pseudo-critical couplings obtained from the various observables and autocorrelation times for runs with different pion masses.

observables cannot be expected to be Gaussian, we have chosen this procedure in order to provide a clear definition of the peak position. The fitted error on β_c definitely underestimates the true uncertainty. Neither is the Gaussian width a good estimate which is due to the background. In order to still get conservative error estimates from our data, we use the width of the fitted region in each case. In this context it is important to note that the scale setting causes the major fraction of the final error on T_c . This is because of the interpolation of the lattice spacing rather than employing dedicated zero temperature runs at the given β_c . In practice, we have included between 3 and 8 points for the fits. The quality of the signals differs strongly for the different quantities and simulation runs. We crosscheck the values that we obtain from the observables by corresponding fits to their integrated autocorrelation times, which similarly show peaks in the transition region due to maximal fluctuations of the system.

All plots for real part of Polyakov loop and $\langle\bar{\psi}\psi\rangle$ are collected in appendix D.3. The obtained pseudo-critical couplings and corresponding temperatures have been collected in table 5.3. Although we are testing a crossover so that the signals cannot be expected to agree among each other, we find a good agreement between our different estimates for the pseudo-critical couplings, see also figure 5.8.

Since the runs B10 and B12 share a common pion mass and differ only by N_τ , they can be used in order to assess the magnitude of cutoff effects. We show the obtained pseudo-critical temperatures in figure 5.9. For better visibility, the points from different observables at the same lattice spacing are slightly shifted. The N_τ -dependence of T_c appears to be contained within the rather large error bars. This indicates that the size

QUANTITY	RUN	N_τ	β_c	T_c (MeV)
$\chi(\text{Re}(L))$	A12	12	3.960(15)	225(7)
$\chi(P)$	A12	12	3.959(15)	225(7)
$\tau_{\text{int}}(\text{Re}(L))$	A12	12	3.965(30)	227(12)
$\tau_{\text{int}}(P)$	A12	12	3.956(23)	224(9)
$\sigma_{\psi\psi}^2$	A12	12	3.940(23)	218(9)
$\tau_{\text{int}}(\overline{\psi}\psi)$	A12	12	3.960(15)	225(7)
$\chi(\text{Re}(L))$	B10	10	3.893(13)	244(7)
$\chi(P)$	B10	10	3.881(15)	239(9)
$\tau_{\text{int}}(\text{Re}(L))$	B10	10	3.890(13)	243(8)
$\tau_{\text{int}}(P)$	B10	10	3.881(05)	239(7)
$\sigma_{\psi\psi}^2$	B10	10	3.880(05)	239(7)
$\chi(\text{Re}(L))$	B12	12	4.021(13)	247(7)
$\chi(P)$	B12	12	4.014(05)	244(5)
$\tau_{\text{int}}(\text{Re}(L))$	B12	12	4.006(07)	241(5)
$\tau_{\text{int}}(P)$	B12	12	4.015(08)	244(5)
$\sigma_{\psi\psi}^2$	B12	12	4.015(05)	245(5)
$\tau_{\text{int}}(\overline{\psi}\psi)$	B12	12	4.018(08)	246(5)
$\chi(\text{Re}(L))$	C12	12	4.043(20)	255(9)
$\chi(P)$	C12	12	4.027(20)	249(9)
$\tau_{\text{int}}(\text{Re}(L))$	C12	12	4.031(30)	251(13)
$\tau_{\text{int}}(P)$	C12	12	4.026(20)	249(9)
$\sigma_{\psi\psi}^2$	C12	12	4.030(20)	250(9)

Table 5.3.: List of all pseudo-critical points from our data.

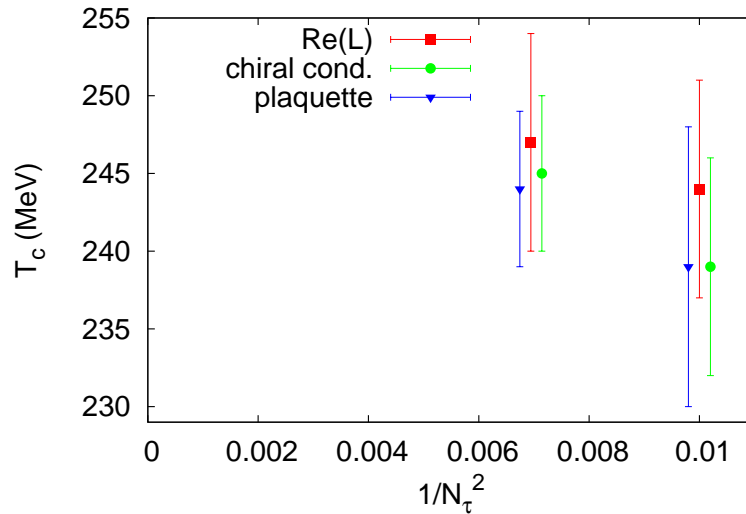


Figure 5.9.: N_τ -dependence of pseudo-critical temperature obtained from the fluctuations of the three observables for B10 and B12. The points for the chiral condensate and the plaquette have been shifted by ± 0.0002 .

of cutoff effects in our simulations is small compared to the combined uncertainties from statistics and scale setting.

5.4. Transition in the Chiral Limit

We now turn to the analysis of our data with respect to the nature of the phase transition in the two flavour chiral limit. We check whether our data are consistent with any of the possible transition scenarios. Note however, that chiral symmetry for Wilson type fermions is broken explicitly so that any universal behaviour that we can hope to observe is continuum behaviour modified by lattice artefacts. This immediately emphasises the need for fine lattices. Moreover, our lattice simulations are performed with finite volume and thus outside the thermodynamic limit in which the universal scaling description strictly holds. Nevertheless, with box sizes $L \gtrsim 2\text{fm}$, we have reason to expect finite volume corrections to be subleading. In any case, one will finally need to accompany our study by finite size scaling analyses and more severe checks on the size of discretisation errors. All this is beyond the scope of our present study which offers a first access to this field of research with maximally twisted mass fermions.

In a first attempt, one can try and fit ¹ the values of $T_c(m_\pi)$ to the scaling form, equation (5.10). It has proven to be infeasible to determine the critical exponents from a fit, see e.g. [79, 171]. This is true for our data as well so that we have to fix the exponents to the given values and check the results for consistency. For $1/(\beta\delta)$ we have used 0.54 for the $O(4)$ scenario, 0.64 for $Z(2)$ and 1 for the first order case. For a first order transition, there is no scaling in a strict sense, but $1/(\beta\delta) = 1$ has been deduced to

¹For the fits in this section which go beyond straight lines, we rely on the implementation of the Levenberg-Marquardt algorithm by `gnuplot` [169]. For a general summary of least square fitting we refer to [170].

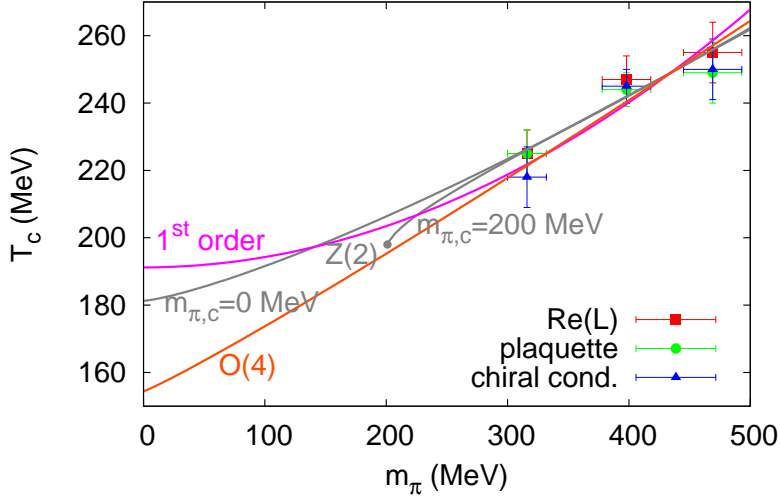


Figure 5.10.: Chiral extrapolation for $T_c(m_\pi)$. The fits assuming second order $O(4)$ or first order exponents are based on the critical temperatures from the chiral condensate. The $Z(2)$ fit is based on all available data points.

mimic the correct behaviour [79, 171]. For the possible critical $Z(2)$ point at finite quark mass, we have to replace $m_\pi \rightarrow m_\pi^2 - m_{\pi,c}^2$. Since the value of $m_{\pi,c}$ is not restricted by our fits either, we have looked at two extremal situations: $m_{\pi,c} = 0$ and 200 MeV.

The resulting extrapolations for all scenarios are shown in figure 5.10. Obviously our data are not capable of a clear separation of the different scenarios. Assuming $O(4)$ universality, we obtain a chiral critical temperature $T_c = 154(38)$ MeV. The other possible universality classes lead to slightly different values. Most importantly, the value for the first order fit, $T_c = 191(23)$ MeV, seems to be slightly above the values expected in other investigations [12]. But the extrapolation relying on the “first order exponents” that we have applied for the sake of comparison since it has also been introduced elsewhere [79, 171] should really be questioned as we have — based on the smoothness of our signals — strong reason to think that our pion masses fall into the crossover regime and thus, before entering the first order region, the critical end point has to be encountered. Note that the existence of a critical point at finite mass also renders a chiral extrapolation impossible.

For fixed $N_\tau = 12$, assuming to be close enough to the continuum, we can also apply equation (5.9) with external field $h = 2a\mu_0$, see figure 5.11. A fit to all three masses is not feasible with $O(4)$ coefficients indicating large scaling violations in the heaviest mass. Restricting to the two lighter masses, there are as many data points as fit parameters. However, we can still estimate

$$\beta_{\text{chiral}}(N_\tau = 12) \approx 3.63. \quad (5.24)$$

This corresponds to $T_c(m_\pi = 0) \approx 138(54)$ MeV where the errors are due to the extrapolation of the scale setting to very small values of β . In any case, this value of T_c is consistent with the one obtained from the previous fit. We use that estimate for β_{chiral} to compare our data with the magnetic equation of state (5.5), where we follow previous

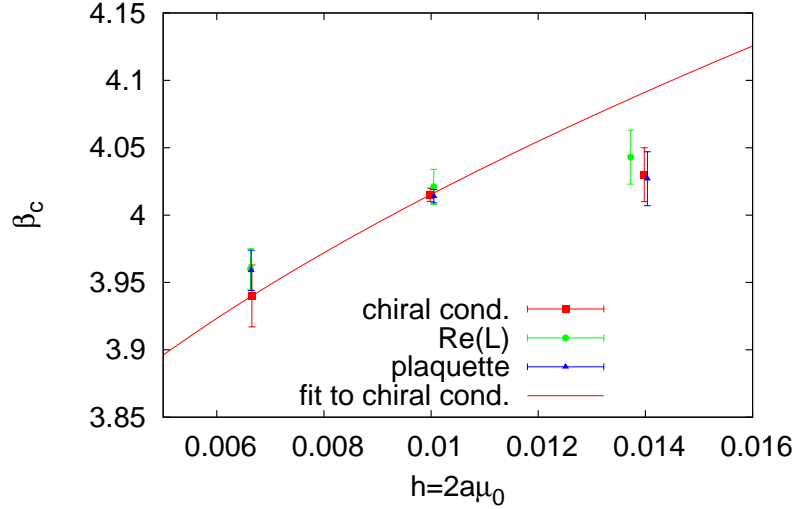


Figure 5.11.: Critical couplings β as function of the external field $h = 2a\mu_0$ at $N_\tau = 12$. The fit includes the couplings obtained from the variance of $\langle \bar{\psi}\psi \rangle$ for the two lightest masses, A12 and B12.

studies [161, 151, 105]. Including possible scaling violations [105] and printing all fit parameters explicitly, we have

$$\langle \bar{\psi}\psi \rangle = h^{1/\delta} c f(d\tau/h^{1/(\delta\beta)}) + a_t \tau h + b_1 h + \dots \quad (5.25)$$

We have fitted our data by using either one or both violation terms. The data set C12 cannot be accommodated by any of these possibilities, leading to large values of χ^2 . On the other hand, fits to A12+B12 are feasible in all combinations, giving a β_{chiral} consistent with our previous determination. The fits work with either correction term alone, but when both are admitted $a_t \approx 0$ within errors, see table 5.4. In figure 5.12, we show a combined fit to A12 and B12 fixing $\beta_{\text{chiral}} = 3.63$ from our independent determination and $a_t = 0$ with $\chi^2/\text{dof} = 0.52$. The fact that these fits are not able to include the C12 data indicates a mass which is outside the regime where the leading corrections, equation (5.25), are applicable. This is in agreement with figure 5.11, where also the heaviest point cannot be included in the scaling description. Furthermore, the relation for the pseudo-critical coupling, $\beta(h)$, has been derived using a double derivative,

$$\frac{\partial^2 \chi_\sigma(x(h, \tau))}{\partial h \partial \tau} = 0, \quad (5.26)$$

and thus from the leading corrections of equation (5.25) only the term proportional to a_t contributes to violations in $\beta(h)$. As we expect a small a_t from our fits, this observation strengthens the confidence that the two lighter masses are properly described by the scaling fit as shown in figure 5.11, and that the point for the heaviest mass, C12, suffers from higher order violations.

Since we are in a range of the scaling variable $\tau/h^{1/(\delta\beta)}$ where the scaling function is rather flat, judgement on whether there are additional violations of the $O(4)$ behaviour or not is difficult. Repeating this exercise for the first order scenario with endpoint does

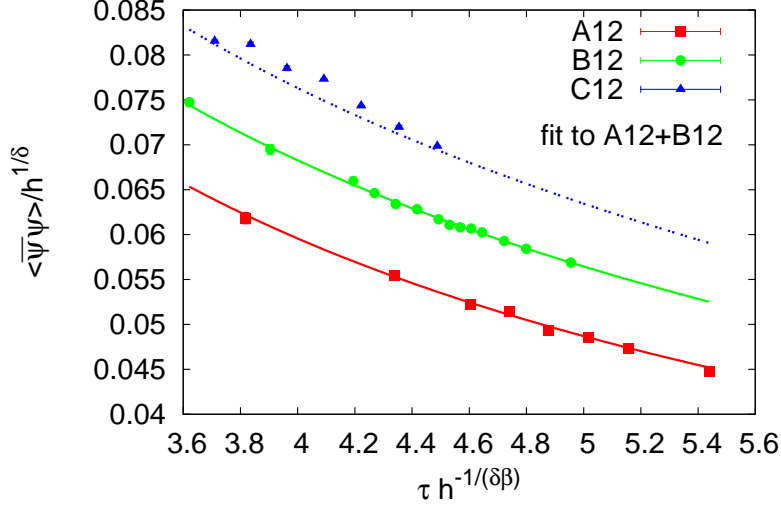


Figure 5.12.: Scaling for the bare $\langle \bar{\psi}\psi \rangle$ for the data at $N_\tau = 12$ and modelling of scaling violations. The fit shown is for the combined A12 and B12 data.

ID	data	β_{chiral}	c	d	a_t	b_1	χ^2/dof
1	A12	3.53(13)	0.149(72)	0.354(45)	0	0	0.44
2	B12	3.38(19)	0.24(20)	0.38(14)	0	0	0.98
3	C12	4(18)	0.2(18.1)	0.5(12.2)			4e+8
4	A12+B12	3.29(2)	1(2)	1.0(1.3)	0	0	1.8
5	A12+B12	3.63(4)	0.37(62)	1.5(1.7)	0	1.2(2)	0.55
6	A12+B12	3.55(4)	0.8(1.6)	1.6(2.1)	1.2(3)	0	0.8
7	A12+B12	3.67(7)	0.4(1.3)	2(5)	-0.79(99)	1.8(7)	0.52
8	A12+B12	3.63	0.6(1.3)	2.1(3.4)	-0.3(5)	1.4(3)	0.52
9	A12+B12	3.63	0.4(4)	1.6(1.2)	0	1.19(2)	0.52
10	A12+B12	3.63	0.7(1.7)	2(3)	1.97(4)	0	1.3
11	A12+B12+C12	3.63			0		5e+7
12	A12+B12+C12	3.63					5e+7
13	A12+B12+C12						5e+7

Table 5.4.: Fits for the (violated) scaling function $cf(dx) + a_t\tau h^{1-1/\delta} + b_1h^{1-1/\delta}$. Numbers in bold face have been fixed before fitting. The C12 data cannot be brought into agreement with the scaling function. If the violating terms b_1 and a_t are omitted, the scaling violations seem to be absorbed by β_{chiral} that becomes considerably smaller (see fits 1,2,4). We cannot disentangle the terms b_1 and a_t but the fits 7 and 8 where both parameters are free seem to suggest $a_t \approx 0$.

not give further insight as the combinations of exponents are too close. Therefore our data are fully consistent with the $O(4)$ scenario, but do not rule out the possibility of the first order case. This would require drastically smaller pion masses combined with finite size studies, as the chiral scaling seems to be valid if $m_\pi \lesssim 300$ MeV.

5.5. Strength of the Anomaly

Pisarski and Wilczek argued that the strength of the anomaly is driven by the instanton density which vanishes for infinite temperature [41]. Thus the temperature scale at which the axial symmetry is effectively restored needs not to be the same as for the deconfinement or chiral transition. This interconnection between the nature of the two flavour chiral transition and the strength of the anomaly has been demonstrated in a model study [172]. As an indicator for the strength of the anomaly, a recent work [173] has calculated the parametric form of the splitting of pseudo-scalar and scalar screening masses at asymptotically large temperatures, $\Delta M/M \sim (\Lambda_{\text{QCD}}/T)^{b_0}$, with $b_0 = (11N_c - 2N_F)/3$.

In any case, it is not known a priori whether the axial anomaly in the range of T_c is effectively restored or not. Existing investigations [150, 174, 175] find a non-restoration of the axial symmetry near T_c . However, none of these studies has complete control of systematic effects.

Screening masses have been used as an observable for finite temperature QCD for a long time [176]. Our findings are in agreement with different recent studies on the subject [177, 178, 179, 180, 181, 182] that usually focus on the behaviour in a larger temperature interval extending into the QGP phase. Here we look at the screening masses and their splittings close to T_c . We start by introducing the screening mass correlators and corresponding quantum numbers. We then continue with a discussion of the properties of free screening masses in section 5.5.2 before we turn to the results from the β -scan at large mass, $m_\pi \approx 1$ GeV. Finally, we present the results from our simulations with lighter pion masses aiming to identify the strength of the anomaly towards the chiral limit in section 5.5.4.

5.5.1. Screening Correlators

Screening masses are defined as the inverse length scale controlling the spatial damping of corresponding medium excitations, i.e. they are determined from the asymptotic behaviour of suitable meson correlators,

$$C_\Gamma(z) \sim e^{-M_{\text{scr}}z} , \quad (5.27)$$

for large enough spatial separation z . Because of the periodicity of the lattice, this expression can be related to a hyperbolic cosine via

$$C_\Gamma(z) \sim e^{-M_{\text{scr}}z} + e^{-M_{\text{scr}}(L-z)} = 2e^{-M_{\text{scr}}L/2} \cosh(M_{\text{scr}}(z - L/2)) . \quad (5.28)$$

From equation (5.27) one can define an effective mass,

$$m_{\text{eff}}(z) = \frac{1}{a} \log \left(\frac{C(z)}{C(z+a)} \right) , \quad (5.29)$$

with

$$m_{\text{eff}}(z \rightarrow \infty) = M_{\text{scr}} . \quad (5.30)$$

For lattice simulations at finite volume, one also has to consider the periodic boundary conditions for the effective mass. Therefore, a suitable definition for a local effective mass,

$$\frac{C(z+a)}{C(z)} = \frac{\cosh(m_{\text{eff}}(z)(z+a-L/2))}{\cosh(m_{\text{eff}}(z)(z-L/2))} , \quad (5.31)$$

needs to be inverted numerically.

We consider flavour non-singlet correlators in this work, i. e. all correlators are of the form

$$\begin{aligned} C_{\Gamma}(z) &= \langle \bar{\psi}(x)\Gamma\tau^{-}\psi(x)\bar{\psi}(0)\Gamma\tau^{+}\psi(0) \rangle \\ &= \langle \bar{u}(x)\Gamma d(x)\bar{d}(0)\Gamma u(0) \rangle , \end{aligned} \quad (5.32)$$

which correspond to the charged mesons formed by up and down valence quarks. The computational advantage of flavour-multiplet correlators is the absence of quark-disconnected contributions. These disconnected pieces render a numerical evaluation very difficult due to large statistical noise. For details of the correlator calculation, we refer to [86]. The correlators can be related to the up-quark propagator S_u alone rather than to both up and down propagator,

$$C_{\Gamma}(z) = \text{Tr} \left(S_u(0, x)\Gamma\gamma_5 S_u^{\dagger}(0, x)\gamma_5\Gamma \right) , \quad (5.33)$$

where we have made use of the relation $S_d(x, y) = \gamma_5 S_u^{\dagger}(y, x)\gamma_5$ as suggested in [86]. The \dagger refers to the spinor and colour components.

The naming scheme for correlators — together with the experimentally determined vacuum mass — is given in table 5.5 including flavour singlets. The scalar and pseudo-scalar quantities of the same flavour content are partners by means of axial $U(1)$ transformations. Therefore, their non-degeneracy signals the axial anomaly, i. e. the breaking of $U_A(1)$.

NAME	OPERATOR	$I^G(J^{P[C]})$	MASS (MeV)
π^{\pm}	$\gamma_5\tau^{\pm}$	$1^-(0^-)$	139.57018(35)
π^0	$\gamma_5\tau^3$	$1^-(0^{-+})$	134.9766(6)
η	γ_5	$0^+(0^{-+})$	547.853(24)
$\sigma, f_0(600)$	$\mathbf{1}$	$0^+(0^{++})$	(400-1200)
(a^0, a^{\pm})	(τ^3, τ^{\pm})	$1^-(0^+)$	980(20)
ρ^{\pm}	$\gamma_j\gamma_4\tau^{\pm}$	$1^+(1^{--})$	775.11(34)
b_1	$\gamma_j\gamma_4\gamma_5\tau^{\pm}$	$1^+(1^{+-})$	1229.5(3.2)

Table 5.5.: Naming scheme for meson states. The operators are to be understood in the physical basis. The masses are the lightest masses in the corresponding channels, taken from [39].

Besides the screening masses, extracted from asymptotic behaviour, also the correlators themselves are indicative of the axial anomaly. In order to avoid systematic uncertainties from the screening mass fits, it is thus advantageous to take the susceptibilities

or integrated correlators into account as well,

$$\chi_\Gamma = \sum_{z \neq 0} C_\Gamma(z), \quad (5.34)$$

where we neglect the contribution at zero distance which is dominated by contact terms.

5.5.2. Free Screening Masses

Screening masses from the free theory are expected to be realised for asymptotic temperatures $T \rightarrow \infty$. Besides providing a limiting value they can also be looked at to learn about volume and cutoff dependence.

As for infinite temperature there are no interactions, screening masses from all channels are expected to be degenerate. This is illustrated by figure 5.13, where free correlators for the pseudo-scalar and scalar flavour non-singlet channels are shown. They have been calculated by a numerical inversion of the propagator with respect to the free gauge field, $U = 1$.

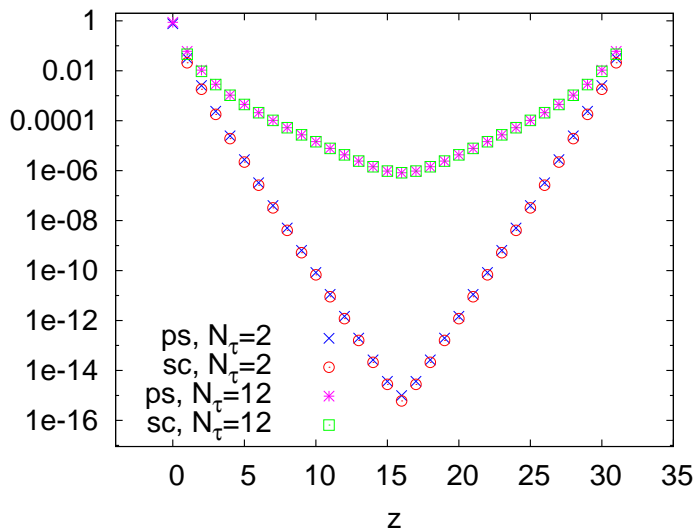


Figure 5.13.: Free pseudo-scalar and scalar correlators for $N_\sigma = 32$, $N_\tau=2,12$.

The value for the free continuum meson screening mass was first conjectured by Eletsky and Ioffe [183]. A complete continuum calculation was then given in [184]. Accordingly, the free screening mass is defined by

$$D(p_1 = p_2 = 0, p_3 = iM_{\text{scr}}/2, p_4 = \pi T) = 0, \quad (5.35)$$

where $D(p)$ is the propagator's denominator for the respective fermion formulation under consideration. The factor 2 in the above relation can be interpreted physically from the fact that the screened mesonic degrees of freedom are constituted by two valence quarks. We give a calculation for the lattice in appendix C.2 which is based on mapping the integration variables onto a unit circle. By inspection of the pole structure, we can then relate the correlator to an exponential decay governed by a screening mass in accordance with equation (5.35).

For free staggered fermions, the leading order cutoff effects must be of $\mathcal{O}(1/N_\tau^2)$. Accordingly, the screening mass has the form

$$\frac{(M_{\text{scr}})^{\text{stagg}}}{T} = 2\sqrt{\pi^2 + \frac{m_q^2}{T^2}} - \frac{1}{3} \frac{2\pi^4 + \frac{m_q^4}{T^4} + 2\pi^2 \frac{m_q^2}{T^2}}{\sqrt{\pi^2 + \frac{m_q^2}{T^2}}} \frac{1}{N_\tau^2} + \dots, \quad (5.36)$$

where m_q is the free quark mass. Wilson fermions, on the other hand, suffer from $\mathcal{O}(a)$ effects that are introduced by a finite mass. Taking into account a possibly twisted mass with $m_q^2 = \mu_0^2 + m_0^2$, the screening mass is given by

$$\begin{aligned} \frac{(M_{\text{scr}})^{\text{tm}}}{T} &= 2\sqrt{\pi^2 + \frac{m_q^2}{T^2}} - \left(\pi^2 + \frac{m_q^2}{T^2}\right)^{-1/2} \frac{m_0 m_q^2}{T^3} \frac{1}{N_\tau} \\ &\quad - \left(\frac{1}{4} \left(\pi^2 + \frac{m_q^2}{T^2}\right)^{-3/2} \frac{m_0^2 m_q^4}{T^6}\right. \\ &\quad \left. + \left(\pi^2 + \frac{m_q^2}{T^2}\right)^{-1} \left(\frac{7}{12}\pi^4 + \frac{\pi^2}{48} + \frac{m_q^2}{48T^2} + \frac{m_q^2 \pi^2}{2T^2} - \frac{m_0^2 m_q^2}{T^4}\right)\right) \frac{1}{N_\tau^2} + \dots \end{aligned} \quad (5.37)$$

Thus at maximal twist, i. e. $m_0 = 0$, the quantity is $\mathcal{O}(a)$ -improved,

$$\begin{aligned} \frac{(M_{\text{scr}})^{\text{mtm}}}{T} &= 2\sqrt{\pi^2 + \frac{m_q^2}{T^2}} \\ &\quad - \left(\pi^2 + \frac{m_q^2}{T^2}\right)^{-1} \left(\frac{7}{12}\pi^4 + \frac{\pi^2}{48} + \frac{m_q^2}{48T^2} + \frac{m_q^2 \pi^2}{2T^2}\right) \frac{1}{N_\tau^2} + \dots \end{aligned} \quad (5.38)$$

From the above formulae it can be seen that the leading discretisation artefacts of all considered lattice formulations are negative, i. e. — at least in leading order and non-interacting limit — the lattice screening mass underestimates its continuum counterpart. Contrary to that, perturbative continuum calculations [185, 186] indicate a positive contribution introduced by interactions.

Another source of deviation from the continuum interacting value stems from the finite volume used in lattice simulations. To get an estimate for this effect, we have obtained values for the free screening mass on lattices of different extent with a maximally twisted mass propagator using $\mu_0/T = 0.006$, see figure 5.14. In this case we have used the effective mass as defined in equation (5.29) at $z = L/4$ to determine the screening mass. Whereas we do not find prominent plateau behaviour for small lattices, we find agreement between the effective masses from equation (5.29) and equation (5.31) at the given position. From Florkowski and Friman [184] we know that the asymptotic behaviour of the massless meson correlator at high temperatures is given by

$$C(z) \simeq \frac{1}{z^2} e^{-2\pi T z} (1 + 2\pi T z). \quad (5.39)$$

This ensures the correct infinite distance behaviour, i. e. $m_{\text{eff}}(z \rightarrow \infty) = 2\pi T$. However, for actual simulations, one has to deal with a finite extent in z -direction. If the

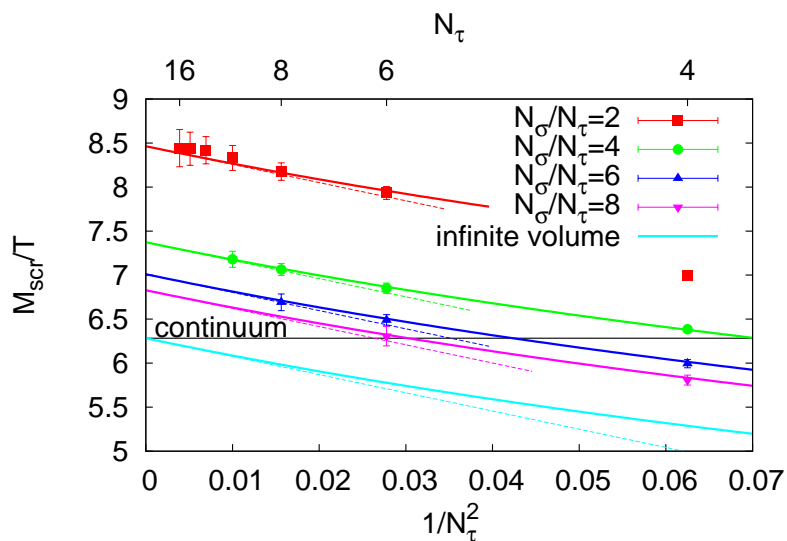


Figure 5.14.: Free screening mass as a function of the lattice spacing squared, $\sim 1/N_\tau^2$, for four values of the aspect ratio. The data have been obtained by numerical inversion of the free propagator, the solid lines consider all cutoff effects whereas the dashed lines only consider the leading $1/N_\tau^2$ contributions.

screening mass is obtained from the effective mass at a given distance, $z = L/n$, the discrepancy can be calculated, cf. [177]. For this purpose, one has to expand the difference $m_{\text{eff}}(L/n) - 2\pi T$ for a small inverse spatial extent finding

$$\frac{M_{\text{scr}}}{T} = \frac{M_{\text{scr}}}{T} \Big|_{V \rightarrow \infty} + n \frac{N_\tau}{N_\sigma} \quad (5.40)$$

for massless quarks.

In figure 5.14 and 5.15 we show corresponding fits to the free screening masses. Figure 5.14 shows the N_τ -dependence at fixed aspect ratio. For the lattice spacing dependence we use the complete functional form as implicitly defined by equation (5.35) in order to take points at all lattice spacings into account. The thinner dashed lines correspond to the formula up to $\mathcal{O}(1/N_\tau^2)$. They seem to be an appropriate description of the data points for lattices with $N_\tau \gtrsim 6$. This situation is somewhat better than for the free pressure, discussed in section 4.2, where finer lattices are needed to achieve a^2 -scaling. The only free fit parameter left is the coefficient of the contribution linear in $1/N_\sigma$, see equation (5.40). According to the above considerations, this parameter should be equal to 4, we actually fit 4.362(22). For this fit we have included all points but the one at $N_\tau = 4$ with aspect ratio 2 that is clearly out of the range of any approximation.

The discrepancy of approximately 9% between the expected value and the fitted one might be explained by finite mass effects which are not included in equation (5.40). However, modifications due to a finite mass $\mu_0/T \ll \pi$ should be rather small. Therefore, it is more likely that we see higher orders of the double expansion in $1/N_\tau$ and the aspect ratio.

Figure 5.15 shows the volume dependence at fixed lattice spacing $N_\tau = 4$. As before, the point with an aspect ratio of 2 has been omitted from the fit. The remaining points

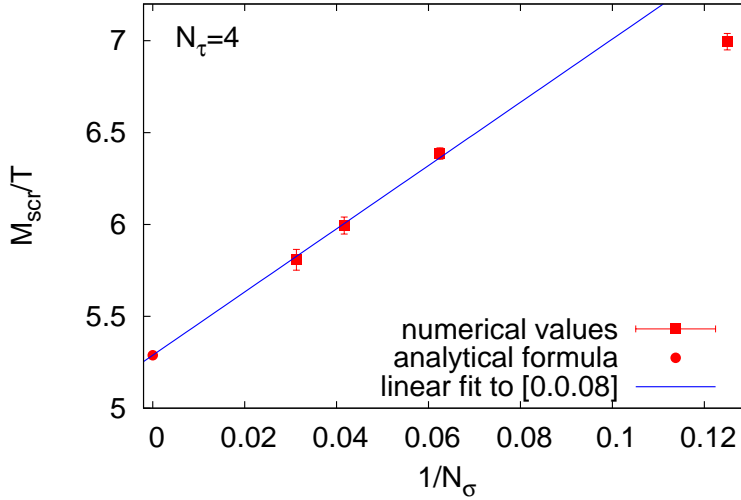


Figure 5.15.: Free screening mass as a function of the inverse spatial extent for $N_\tau = 4$ and linear fit to all points except the one for the smallest volume.

give a linear behaviour with fitted ordinate $5.28812(21)$ and slope $4.30(11) \cdot N_\tau$. The slope is off the naive prediction of 4 but is in fine agreement with the previously obtained value for the data at fixed aspect ratio.

In conclusion the leading order cutoff and finite volume effects for free screening masses can be modelled,

$$M_{\text{scr}}\left(\frac{1}{N_\tau}, \frac{1}{N_\sigma}\right) = M_{\text{scr}}(0,0) + c_{(L)} \frac{N_\tau}{N_\sigma} - c_{(a)} \frac{1}{N_\tau^2}, \quad (5.41)$$

with positive coefficients $c_{(L,a)}$ that depend solely on the fermions' discretisation scheme — that needs to be $\mathcal{O}(a)$ -improved, of course.

Note that contrary to the above findings, one expects exponentially suppressed finite volume effects for the zero temperature interacting spectrum [133]. However, the corresponding proof is based on the calculation of zero temperature scattering amplitudes. The linear dependence of free screening masses has also been found in [177] where also a restoration of the exponential behaviour is observed when approaching T_c from above. Therefore we do not expect finite volume effects as severe as in the free case for our dynamical screening masses at $T \sim T_c$.

5.5.3. Large Mass Regime

We have obtained first results for dynamical screening masses from our simulations at larger masses, $m_\pi \sim 1 \text{ GeV}$, where simulations are rather cheap, cf. [28]. Due to the large quark mass, the estimate for the conversion to physical units using ETMC data is not very reliable. For $a\mu_0 = 0.04$ the transition is found at $\beta_c = 3.875(13)$ which roughly corresponds to a pion of 1 GeV and a temperature slightly below 300 MeV. For the lighter $a\mu_0 = 0.025$ the determination of β_c is more difficult because of lower statistics. However, the transition appears to happen in the same β -regime.

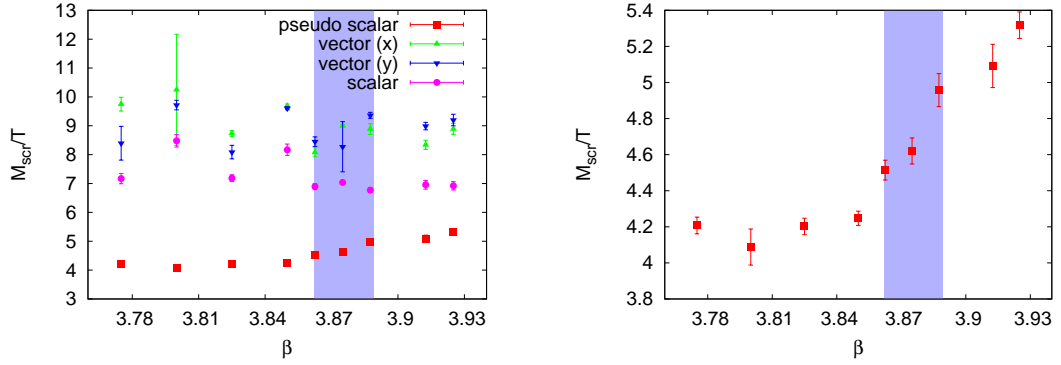


Figure 5.16.: Left: Behaviour of screening masses on a $16^3 \times 8$ lattice for $a\mu = 0.04$ at critical hopping parameter. Right: Same as before for pseudo-scalar screening mass only. The transition is located at $\beta_c = 3.875(13)$.

Note that the determination of screening masses from the asymptotic behaviour at such small volumes is not expected to work very well. However, we have found the cosh-fits to give quite reliable results. Figure 5.16 shows the resulting behaviour of the screening masses for $a\mu_0 = 0.04$. As can be seen, the spin zero mesons behave quite smoothly whereas the vector meson is rather affected by noise. Especially the charged pion mass, which is shown in the right panel, indicates the transition very well.

Figure 5.17 shows the difference of scalar and pseudo-scalar flavour multiplet screening masses for $a\mu_0 = 0.025$ and $a\mu_0 = 0.04$, i. e. a measure for the $U_A(1)$ splitting. As expected, the symmetry splitting is lowered for rising temperature. However, in the transition regime it is clearly non-zero. Furthermore, the effect of reducing the pion mass by approximately a factor $\sqrt{(0.025/0.040)} \approx 0.79$ seems to be negligible.

In conclusion, these results can already be taken as a hint that the $U_A(1)$ anomaly is not restored at the transition temperature. Of course, the large mass ~ 1 GeV prevents a stronger statement. Accordingly, we present the results based on our runs A12, B12 and C12 in the following section aiming at the chiral limit. The most important observation of this section is certainly the very weak mass dependence.

5.5.4. Towards the Chiral Limit

Our runs at pion masses below 500 MeV (A12, B10, B12, C12) form the basis for our investigations of properties towards the chiral limit. Unfortunately, not always large statistics from the existing tmfT configurations are available for the determination of screening masses. Therefore, the necessary fits are affected by rather large uncertainties. We have found that applying the cosh-relation given in equation (5.28) to our data with fit ranges from an optimisation of χ^2/dof leads to mass values which are systematically about 10% larger than the results based on the long distance behaviour of the local effective masses, equation (5.31). We attribute this to the rather large error bars due to small statistics. This implies that the cosh-fit appears to be reliable even in z -ranges where the description by a single exponential decay is no longer valid. For this reason, we have resorted to determine the screening masses from fits of a constant to the tails of the local effective masses. Figure 5.18 gives an example for our run A12. The left hand panel shows the fitted constant whereas the right hand side presents the application of

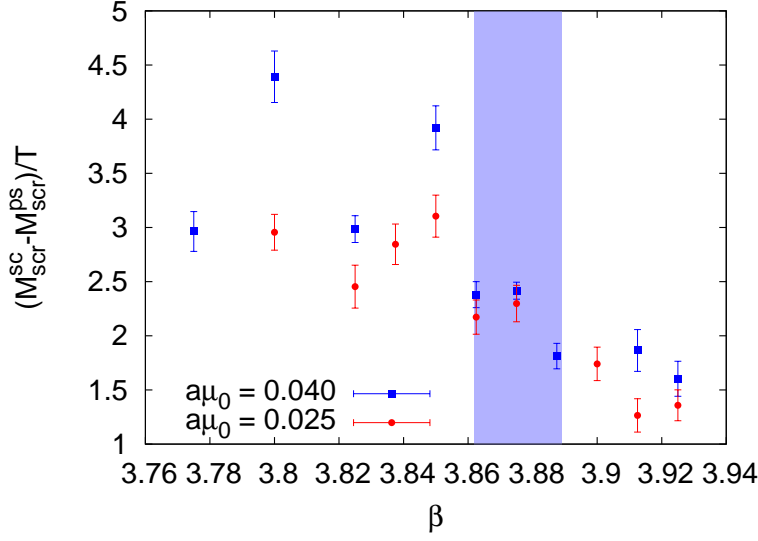


Figure 5.17.: Difference of scalar and pseudo-scalar flavour multiplet screening masses for $a\mu_0 = 0.025$ and $a\mu_0 = 0.04$ on a $16^3 \times 8$ lattice.

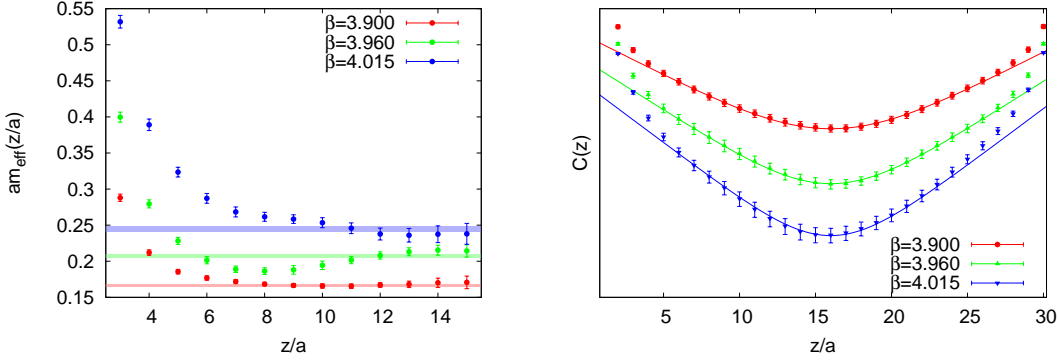


Figure 5.18.: Comparison of local effective masses and correlators for three values of the lattice coupling in run A12.

the fit result to the cosh-behaviour (with an additionally determined prefactor for the cosh).

All fits are collected in appendix D.4. Nevertheless, the possibly large intrinsic uncertainties from the available data samples — also reflected by poor values of χ^2 for some of the screening masses — must be considered before drawing strong conclusions from those results. We give an example for scalar and pseudo-scalar charged screening masses in figure 5.19, left. Especially the large fluctuations of the scalar mass indicate the problematic situation for the fitting procedure. Note that a firm determination of the scalar mass has not been possible in all cases.

The right hand side of figure 5.19 shows the pseudo-scalar screening mass for the two runs B10 and B12. In the (pseudo-)critical region, these masses are expected to show an increase which we indeed observe. From comparison of the B10 and B12 data, it is also clear that the discretisation errors are smaller than the combined statistical and

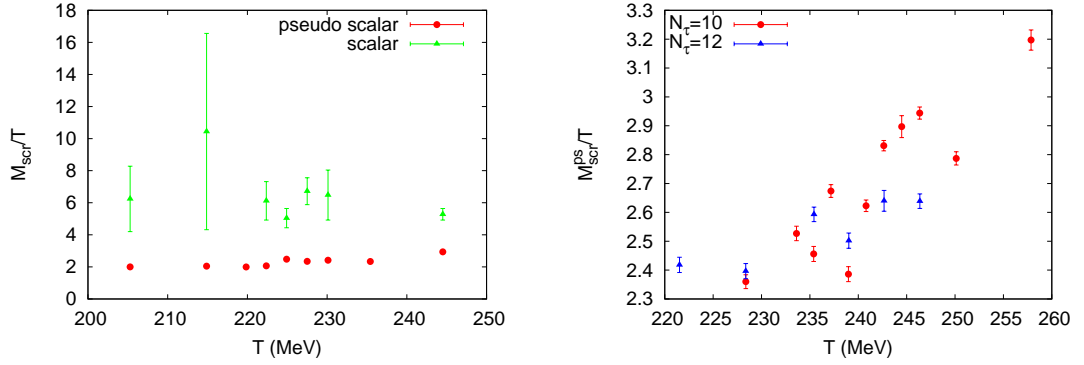


Figure 5.19.: Screening masses for different runs. We have neglected the uncertainty in T from the scale setting for these plots. Left: Charged scalar and pseudo-scalar masses for A12. Right: Charged pseudo-scalar mass for B10 and B12.

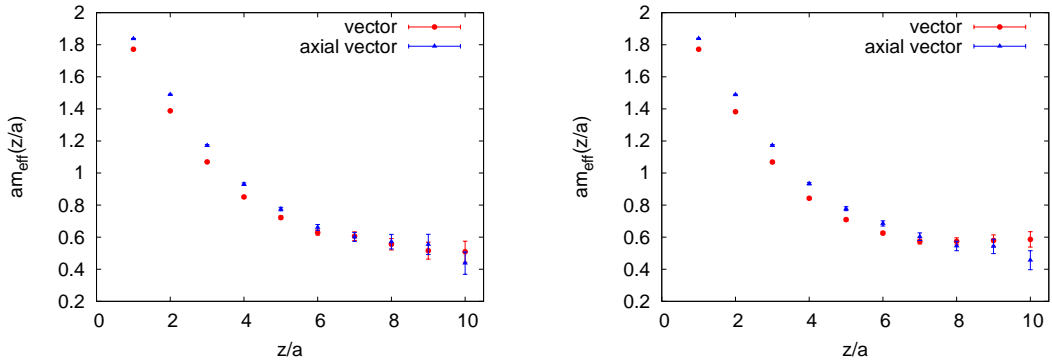


Figure 5.20.: Comparison of local effective masses for the vector and axial vector channels. Left: A12, $\beta = 3.960$. Right: B12, $\beta = 4.000$.

systematic errors. For the following we concentrate on the scalar and pseudo-scalar masses which are important to quantify the axial anomaly. For the vector and axial vector channels, we find degeneracy close to and above T_c , see figure 5.20 for examples at β -values close to β_c for A12 and B12.

The splitting of the pseudo-scalar and scalar screening masses from runs A12, B12 and C12 is shown in figure 5.21, left. Not surprisingly, the results are very noisy. However, comparing to figure 5.17 the splitting seems to be slightly enhanced for the smaller masses even though the lattice spacing is different. In order to get more stable results, we consider the integrated susceptibilities for the screening correlators as defined in equation (5.34). For those quantities no fits are needed. Hence the main source of uncertainty for the screening masses is discarded. Consequently, the splitting of the scalar and pseudo-scalar susceptibilities as shown in figure 5.21, right, gives a much more coherent picture than the mass splitting does.

For both the splitting of screening masses and susceptibilities, we have determined the value in the transition region. For this purpose we have used the pseudo-critical temperatures related to $\sigma_{\psi\psi}^2$, as collected in table 5.3. In figure 5.21, this is indicated by the correspondingly shaded areas. The result is shown in figure 5.22. Whereas all

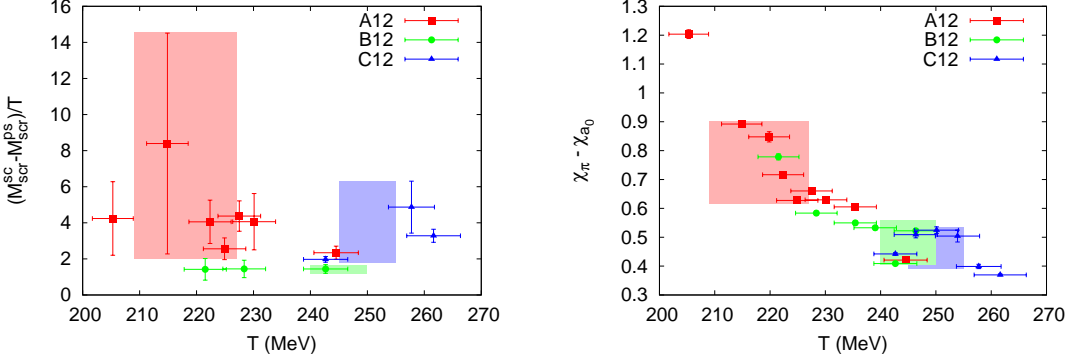


Figure 5.21.: Strength of the anomaly as a function of temperature determined from the splitting of screening masses (left) and their susceptibilities (right) for runs A12, B12, C12.

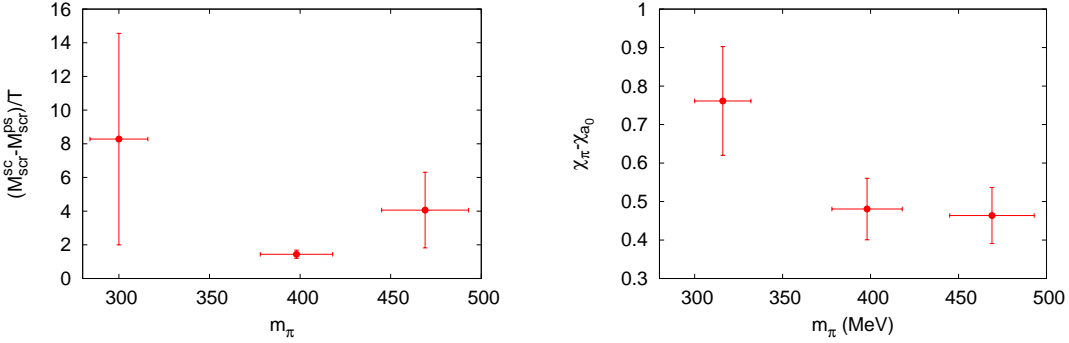


Figure 5.22.: Strength of the anomaly as a function of pion mass determined from the splitting of screening masses (left) and their susceptibilities (right).

that can be read off from the mass splittings is that they seem to be more or less consistent within error bars, the splitting from the susceptibilities exhibits an increase towards smaller pion masses. This is an important observation indicating that the axial anomaly might not be negligible in the chiral limit.

Concentrating on the susceptibilities, we accompany our previous plots by the ratio χ_{π}/χ_{a_0} which approaches 1 for vanishing anomaly. Figure 5.23, left, presents the ratio for all of our runs. The data for B10 are more scattered than those for the runs at $N_{\tau} = 12$. The conclusions for $N_{\tau} = 12$ are the same as those from figure 5.21. Furthermore, the lattice spacing dependence judged by runs B10 and B12 again appears to be small compared to other uncertainties. Note however, that an extrapolation to vanishing anomaly — i. e. unit ratio — in the continuum limit is not excluded as can be estimated from figure 5.23, right. Especially, the B10 point has too large errors to pose a strong constraint on the extrapolation.

The remaining question is whether our numbers for the $U_A(1)$ splitting have to be considered large or small. There is no unique answer and different studies have proposed one interpretation or the other, see e. g. [150] and [187] respectively. Chandrasekharan and Mehta have found in their model study that the anomaly has to be quite strong in order to change the nature of the transition from first to second order [172], possibly

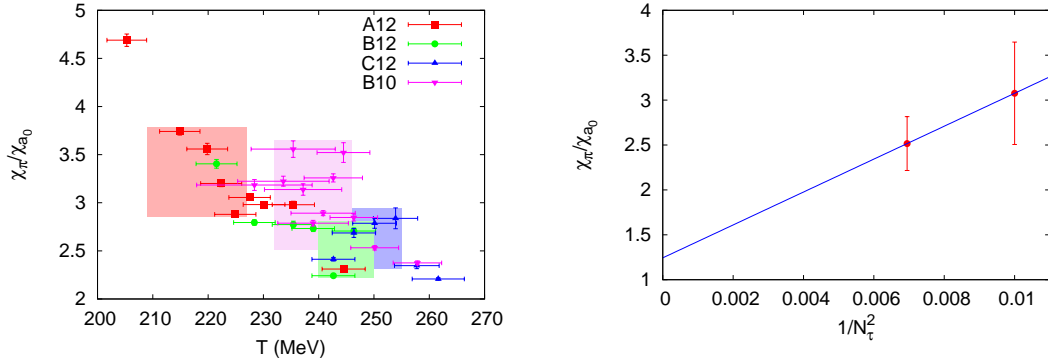


Figure 5.23.: Ratio of the pseudo-scalar and scalar susceptibilities. Left: Temperature dependence for all available pion masses. Right: Lattice spacing dependence for the intermediate pion mass (runs B10 and B12).

larger than in QCD. However, as they argue themselves, the strength of the anomaly is calculated from non-critical scales so that a direct comparison to QCD is not admissible. Altogether, we interpret our findings, in particular the rising behaviour towards smaller pion masses, such that the anomaly might not be negligible in the chiral limit.

5.6. Summary and Discussion

In this chapter we have presented the first simulations employing maximally twisted mass fermions at finite temperature that aim to extract physical results. For all necessary zero temperature information we can rely on ETMC [24]. Given their results, we have interpolated critical hopping parameters, lattice spacings and pion masses in order to set up scans in the lattice coupling β at maximal twist. These β scans have been performed at $N_\tau = 12$ for three pion masses in the range $300 \lesssim m_\pi \lesssim 500$ MeV. For the intermediate pion mass we have additionally simulated at $N_\tau = 10$ which allows to estimate that cutoff effects are smaller than our combined statistical and scale setting errors. Altogether, we have designed a framework based on zero-temperature input from ETMC that allows to perform $N_f = 2$ finite temperature simulations towards the chiral limit with maximally twisted mass fermions.

It has to be mentioned that our values for the pseudo-critical temperatures are somewhat above those of comparable simulations with clover improved fermions by the QCDSF/DIK collaboration [79, 80]. The source for this discrepancy remains unknown but could be connected to remaining discretisation effects and uncertainties in the scale setting. Note that there is already a difference by about 10 % in the Sommer parameter r_0 from ETMC and QCDSF. In any case, the corresponding chiral extrapolations lead to comparable results for the chiral critical temperature within errors. Furthermore, the quality of signals for the pseudo-critical point seems to be comparable between the clover study and our twisted mass simulations.

We have shown a first application of studies based on universal scaling for maximally twisted mass fermions. Our results indicate that the scaling window is not reached before $m_\pi \lesssim 300$ MeV. Therefore, in order to uniquely determine the nature of the two flavour chiral transition clearly much lighter pion masses are needed. Our data cannot

discriminate the different scenarios for the transition in the chiral limit. However, we find that the scaling description with $O(4)$ exponents causes less tension within our data than other assumptions. The corresponding extrapolation yields a chiral critical temperature $T_c = 154(38)$ MeV.

The apparent preference for the second order transition can also be found in our study of screening properties. The determination of screening masses themselves has proven to be very error-prone due to small data sets. But the splittings of the integrated correlators might indicate that the strength of the anomaly is not negligible, even increasing towards the chiral limit.

6. Including Strange and Charm Quarks

In this chapter, we discuss the inclusion of heavier quark flavours. Relevant for the QCD thermal transition is in particular the strange quark with a mass that is comparable to the transition temperature. But also effects in thermal QCD caused by the charm quark have been of some interest recently [188].

For twisted mass QCD the extension by two more flavours at once is natural as the theory is formulated in terms of flavour doublets. Simply adding a copy of the action for up and down quarks, equation (3.21), is not sufficient since a degeneracy of strange and charm masses is not acceptable. However, the possibility to include a mass splitting for the doublet partners has been known for some time [189].

Based on the existing zero temperature work by ETMC [24, 190, 191] we are in the position to set up simulation runs at finite temperature with this so-called $N_f = 2+1+1$ twisted mass QCD. There are no dynamical simulations at finite temperature to report on yet. However, in the following section, we collect the action and information available from ETMC. In section 6.2 we then discuss the perspectives for finite temperature simulations by looking at the behaviour of the free pressure and giving a possible set of parameters.

6.1. Twisted Mass Action with Four Flavours

If we want to apply the ETMC results at zero temperature, the gauge action has to be Iwasaki improved. This choice is motivated in order to minimise the size of the unphysical first order transition plane in bare parameter space. The extent of this plane imposes a lower bound on the quark mass that can be used with the twisted mass action. The fermion action for the heavy doublet, χ_h , is given by

$$S_h = \sum_x \bar{\chi}_h(x) (1 - \kappa_h D_W[U] + 2i\kappa_h a \mu_\sigma \gamma_5 \tau^1 + 2\kappa_h \mu_\delta \tau^3) \chi_h(x), \quad (6.1)$$

where we employ the same notation as ETMC [24]. The renormalised strange and quark masses are determined by the heavy twisted mass μ_σ and the splitting μ_δ ,

$$(m_{\text{strange}})_R = Z_P^{-1} (\mu_\sigma - Z_P/Z_S \mu_\delta), \quad (6.2a)$$

$$(m_{\text{charm}})_R = Z_P^{-1} (\mu_\sigma + Z_P/Z_S \mu_\delta). \quad (6.2b)$$

Note that at tree-level $\mu_\sigma = (m_{\text{strange}} + m_{\text{charm}})/2$ and $\mu_\delta = (m_{\text{charm}} - m_{\text{strange}})/2$. Cichy and Luschevskaya have investigated $\mathcal{O}(a)$ -improvement at tree-level [192] and found everything in accordance with the theoretical expectation. However, they suspect that cutoff effects introduced by the large charm mass might be quite severe and depend crucially on the chosen improvement condition for the critical hopping parameter.

ETMC have fixed the heavy hopping parameter κ_h by the same condition as the light one, κ_l ,

$$\kappa_h = \kappa_l = \kappa_c(\beta, \mu_l), \quad (6.3)$$

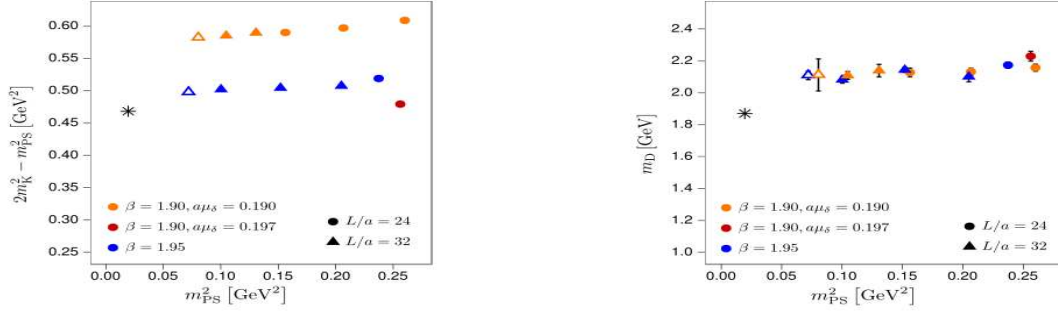


Figure 6.1.: Tuning of strange and charm quark mass. (from [24])

i. e. both parameters are tuned to the same critical value by means of the PCAC relation, equation (3.36). Unlike the two flavour case, one has to take into account the non-trivial dependence on the light quark mass μ_l .

ETMC adjust strange and charm quark masses via the quantities $2m_K^2 - m_{PS}^2$ and m_D . The D mesons are bound states of a charm quark and a light, up or down, partner so that their mass is indicative for the charm quark mass. According to leading order chiral perturbation theory, the ratio $2m_K^2 - m_{PS}^2 \sim m_{\text{strange}}$ is sensitive to the strange quark mass, cf. (2.26) and (2.27). Figure 6.1, which has been taken from ETMC [24], illustrates this procedure. As can be seen from the figure, the accuracy of the adjustment differs among their data sets where the one at $\beta = 1.95$ gives the best agreement for the whole range of pion masses.

Finally, the reported lattice spacings are [24, 191]

$$a(\beta = 1.90) = 0.086 \text{ fm} , \quad (6.4a)$$

$$a(\beta = 1.95) = 0.078 \text{ fm} , \quad (6.4b)$$

$$a(\beta = 2.10) = 0.060 \text{ fm} . \quad (6.4c)$$

6.2. Four Flavours at Finite Temperature

In order to get an idea of cutoff effects for $N_f = 2 + 1 + 1$, one can repeat the calculation of the free pressure, see section 4.2. We explain the adjustment of that calculation for the mass non-degenerate case in the following section 6.2.1. A possible setup for non-perturbative simulations is then proposed in section 6.2.2.

6.2.1. Cutoff Effects for the Non-Interacting Pressure

To calculate the free pressure, we need to deal with the fermion determinant. However, since the fermion matrix for the mass split doublet is no longer diagonal in flavour space the evaluation of $\ln Z = \ln \text{Det } M_F$ is more complicated.

The fermion matrix for the heavy doublet can be written as

$$M_h = M_W + ia\mu_\sigma \gamma_5 \tau^1 + a\mu_\delta \tau^3 \quad (6.5)$$

using the parametrisation in which the quark mass m_0 appears rather than the hopping parameter. M_W is the standard Wilson part of the matrix. The fermion determinant

can then be expressed as

$$\text{Det } M_h = \text{Det} \begin{pmatrix} M_W + a\mu_\delta & ia\mu_\sigma\gamma_5 \\ ia\mu_\sigma\gamma_5 & M_W - a\mu_\delta \end{pmatrix}, \quad (6.6)$$

where the right hand side explicitly shows the flavour structure. Evaluation of equation (6.6) involves some non-trivial steps as explained by Frezzotti and Rossi [189]. Following their solution, we can compute the flavour determinant straightforwardly and rewrite the remaining part in spinor space using the explicit form of the Wilson fermion matrix in momentum space,

$$M_W - M_W^\dagger = 2i\bar{p}_\mu\gamma_\mu, \quad (6.7)$$

so that one gets

$$\text{Det } M_h = (|M_W|^2 + (a\mu_\sigma)^2 - (a\mu_\delta)^2)^{N_s} \text{Det} \left(1 + \frac{2i\bar{p}_\mu\gamma_\mu a\mu_\delta}{|M_W|^2 - (a\mu_\delta)^2 + (a\mu_\sigma)^2} \right). \quad (6.8)$$

The latter part can be expanded in powers of $a\mu_\delta$ using

$$\text{Det} (1 + 2a\mu_\delta B) = e^{\text{Tr} (\log(1+2a\mu_\delta B))} \quad (6.9)$$

with

$$B = \frac{i\bar{p}_\mu\gamma_\mu}{|M_W|^2 - (a\mu_\delta)^2 + (a\mu_\sigma)^2}. \quad (6.10)$$

Finally, the determinant can be expressed as

$$\begin{aligned} \text{Det } M_h &= (|M_W|^2 + (a\mu_\sigma)^2 - (a\mu_\delta)^2)^{N_s} \\ &\cdot \left(1 + 4a^2\mu_\delta^2 \frac{\bar{p}^2}{(|M_W|^2 + (a\mu_\sigma)^2 - (a\mu_\delta)^2)^2} \right)^{N_s/2}. \end{aligned} \quad (6.11)$$

The pressure for a mass non-degenerate doublet is accordingly given by

$$p = \frac{1}{2} N_s N_c \int \frac{d^3p}{(2\pi)^3} \frac{1}{N_\tau} \sum_{n=0}^{N_\tau-1} \ln \left((|M_W|^2 + (a\mu_\sigma)^2 - (a\mu_\delta)^2)^2 + 4a^2\mu_\delta^2 \bar{p}^2 \right) \quad (6.12)$$

if the proper vacuum subtraction is taken into account.

This relation can be used to numerically integrate the free pressure to all orders of the lattice spacing or to perform the analytical expansion for small $1/N_\tau$ in the sense of [143]. The needed dispersion relation follows from the argument of the logarithm as this is essentially the diagonalised inverse fermion matrix. As needed, two branches can be identified, that correspond to the strange and charm dispersion relation, respectively,

$$E^\pm = E_{(0)}^\pm + aE_{(1)}^\pm + a^2E_{(2)}^\pm + \dots \quad (6.13)$$

At maximal twist, to $\mathcal{O}(a^0)$ and for $\mathbf{p} = 0$, this is simply

$$E_{(0)}^+ = \mu_\sigma + \mu_\delta = m_{\text{charm}}, \quad (6.14a)$$

$$E_{(0)}^- = \mu_\sigma - \mu_\delta = m_{\text{strange}}. \quad (6.14b)$$

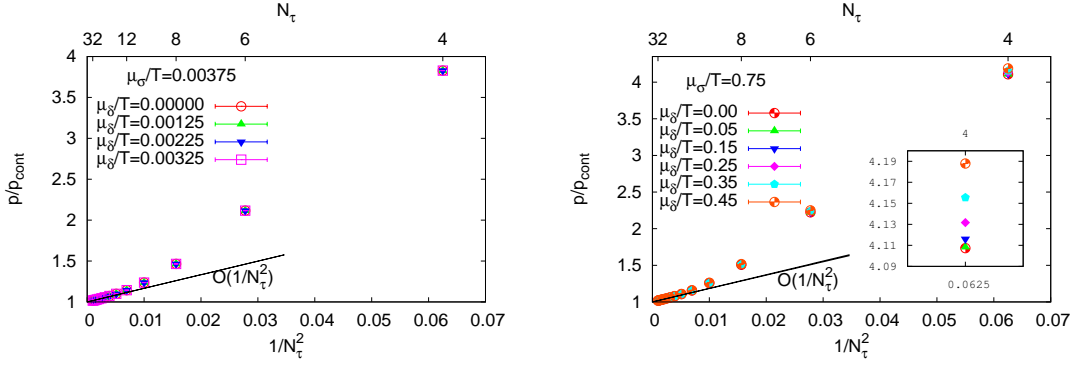


Figure 6.2.: Free pressure normalised to the continuum value for a twisted mass quark doublet with different mass splittings. Left: Light $\mu_\sigma/T = 0.00375$. Right: Heavier $\mu_\sigma/T = 0.75$.

For the following, we concentrate on maximal twist to simplify notation. The dispersion relation to the first orders in the lattice spacing is then determined by

$$E_{(0)}^\pm = \sqrt{\mathbf{p}^2 + (\mu_\sigma \pm \mu_\delta)^2}, \quad (6.15a)$$

$$E_{(1)}^\pm = 0, \quad (6.15b)$$

$$E_{(2)}^\pm = -\frac{1}{2E_{(0)}^\pm} \left(\frac{1}{12} (E_{(0)}^\pm)^4 + \frac{1}{3} \sum_j p_j^4 - \frac{1}{4} \mathbf{p}^4 + \frac{1}{2} \mathbf{p}^2 (E_{(0)}^\pm)^2 \right) \pm \frac{\mu_\delta}{8E_{(0)}^\pm \mu_\sigma} \left((E_{(0)}^\pm)^2 - \mathbf{p}^2 \right)^2. \quad (6.15c)$$

The pressure for a mass split quark doublet at maximal twist, resulting from numerical integration, is plotted together with the analytical $\mathcal{O}(1/N_\tau^2)$ prediction in figure 6.2. A light average quark mass, $\mu_\sigma/T = 0.00375$, is shown on the left, a heavier one, $\mu_\sigma/T = 0.75$, on the right. As can be seen, additional cutoff effects due to the splitting are mostly negligible. Only in the heavier example and for the coarsest lattice, some deviations can be identified. This is in accord with the leading corrections for the $\mathcal{O}(a^2)$ artefacts from μ_δ with $\mathbf{p} = 0$, which are proportional to $m_q^2 \mu_\delta$. These corrections are very small so that they are not visible for the analytical prediction shown in figure 6.2.

6.2.2. Simulation Setup

It is now important to formulate sets of parameters for possible simulations with $N_f = 2 + 1 + 1$ maximally twisted mass fermions. Since the critical hopping parameter has to be considered a function of both the coupling β and the light quark mass μ_l , an interpolation for a scan in β is affected by larger uncertainties than in the two flavour case. For a first exploratory study it is thus preferable to work at one of the β values used by ETMC only and perform scans in μ_l . Choosing $\beta = 1.95$, the tuning to the physical strange and charm masses is more accurate. One then has [24]

$$a\mu_\sigma = 0.170 \quad \text{and} \quad a\mu_\delta = 0.135 \quad (6.16)$$

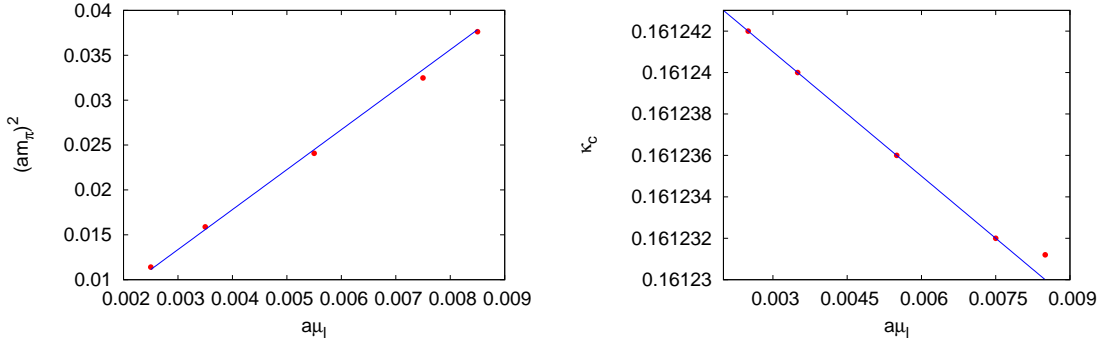


Figure 6.3.: Light quark mass dependence for pion mass (left) and critical hopping parameter (right) at $\beta = 1.90$. Linear fits are shown.

$a\mu_l$	m_π (MeV)	κ_c
0.00250	268(3)	0.161242
0.00275	281(3)	0.161241
0.00300	293(3)	0.161241
0.00325	305(3)	0.161240
0.00350	317(3)	0.161249
0.00375	328(3)	0.161239
0.00400	339(3)	0.161239
0.00425	349(3)	0.161238

Table 6.1.: Pion mass and critical hopping parameter for several values of the light quark mass μ_l as determined from our fits to the ETMC data at $\beta = 1.95$ [24].

with $a = 0.07775(39)$ fm, where the lattice spacing is determined by ETMC from the combined data at $\beta = 1.90$ and 1.95 .

For such a mass scan, only interpolations for the pion mass and the critical hopping parameter as functions of μ_l are needed. As is shown in figure 6.3, linear interpolation is sufficient for the range of quark masses under consideration. The fits shown correspond to linear functions,

$$\kappa_c(\mu_l, \beta = 1.95) = b_\kappa - m_\kappa a\mu_l, \quad (6.17a)$$

$$(am_\pi)^2(\mu_l, \beta = 1.95) = c_\pi a\mu_l, \quad (6.17b)$$

with $b_\kappa = 0.161247$, $m_\kappa = -0.002$ and $c_\pi = 4.45(6)$.

With the above information, it is possible to identify promising simulation points. Table 6.1 gives an overview of possible pion masses and critical hopping parameters for a range of light quark masses. At the chosen value, $\beta = 1.95$, a lattice of size $N_\tau = 12$ corresponds to a temperature $T = 212(1)$ MeV so that, judging from the $T_c(m_\pi)$ for $N_f = 2$, one might expect to find the thermal transition in the accessible range of pion masses.

Finally, we suggest $N_\sigma = 32$ or 36 . With $N_\sigma = 36$, the aspect ratio would be 3 and $m_\pi L \gtrsim 3.8$ so that finite size artefacts should be under control. Given the necessary computing time, the proposed simulations could be performed with the existing public twisted mass code [129].

7. Conclusions and Research Perspectives

This thesis provides the first application of twisted mass lattice QCD to thermal systems of strongly interacting matter. We have worked out the properties of these lattice fermions at finite temperature and demonstrated their applicability to thermal QCD by investigating the two-flavour thermal transition. Finally, we have also argued for the extension to the case of $N_f = 2 + 1 + 1$.

After a summary of known properties of QCD in the continuum we have introduced the lattice framework spending particular interest on twisted mass fermions and their known features. The most prominent reason to use twisted mass fermions is their automatic $\mathcal{O}(a)$ -improvement at maximal twist. We have begun the presentation of our results with chapter 4 where we study properties of the lattice fermions with twisted mass at finite temperature. The roots of that chapter's contents date back to the time before this thesis. However, crucial results and insights have been obtained as part of this work. On the one hand this concerns the non-trivial phase diagram of twisted mass fermions in bare parameter phase space. The bulk transitions already present in the vacuum are accompanied by the thermal transition which appears in form of a conical surface that wraps around the chiral critical line of hopping parameters. We have revealed this structure, which had originally been motivated by Creutz, by means of numerical simulations and comparison to chiral perturbation theory predictions for lines of constant pion mass. On the other hand, we also discuss our investigations of the pressure in the weakly interacting limit in chapter 4. The main contribution by this work has been the analytical calculation of $\mathcal{O}(a)$ and $\mathcal{O}(a^2)$ effects for the free pressure at a finite mass. By comparison of these results to the numerically integrated lattice pressure it has become clear that a^2 -scaling is not present before $N_\tau \gtrsim 10$. These findings are supplemented by the $\mathcal{O}(g^2)$ corrections obtained from numerical integration which show qualitatively comparable behaviour. Interesting to note is furthermore that the differences between the fermion discretisations to leading orders in the lattice spacing seem to be rather small.

In chapter 5 we turn to the physics of the thermal transition for $N_f = 2$. We have performed simulations for three pion masses in the range $300 \text{ MeV} \leq m_\pi \leq 500 \text{ MeV}$. The scale setting and tuning to maximal twist have been achieved by interpolation of ETMC data. This procedure saves a vast amount of computing time, of course. Signal extraction from the different observables — real part of the Polyakov loop, chiral condensate and plaquette — has proven to be rather difficult. We attribute these difficulties to the crossover nature of the transition in our mass range. However, beyond the level of single observables, i. e. when comparing several signals at a time, we have strong confidence in the reliability of our (pseudo-)critical temperatures. For future projects, our experience with signals of Wilson type fermions strongly recommends to study several observables from the beginning and not to perform too large leaps at once

when changing parameters such as the pion mass or lattice spacing.

Given our values for the pseudo-critical temperature, we have tried to extrapolate to the chiral limit based on the scaling formula (5.10). An unambiguous discrimination of the nature of the chiral transition from the difference in the critical exponents has not been possible. This is not too much of a surprise since this kind of analysis has proven to be difficult in earlier studies with different types of lattice fermions as well. In the end, the critical exponents are too close in order to draw definite conclusions on a firm ground. However, our data seem to prefer the $O(4)$ scenario if we compare our temperatures to other results. We then get a chiral critical temperature $T_c = 154(38)$ MeV. The task for future work will be to decrease the uncertainty of that number. On the one hand, one needs to reduce the sources of uncertainty for the pseudo-critical temperatures at finite pion mass. Besides the determination of the critical couplings themselves this particularly requires an improved scale setting. This can be achieved by dedicated zero-temperature runs at the critical couplings so that the interpolation of ETMC input is no longer needed. On the other hand one needs to include lighter pion masses into the study since this leads to a stronger constraint of the fits. Indeed, by inspection of figure 5.10, $m_\pi \approx 200$ MeV might be necessary to discriminate the different scenarios. For twisted mass fermions this pion mass seems to be very ambitious today. However, given the ongoing increase in computing power, simulating pions at 200 MeV is not completely out of bounds.

A complementary approach to the chiral limit is opened by the magnetic equation of state, (5.5), which does not necessarily need a priori information of critical points. In principle, a fit to a number of free parameters, including the chiral critical coupling, is sufficient. Our inspection of this route has shown that we need to include leading orders of scaling violations. Accordingly, our masses are still to be considered large with respect to the regime of critical scaling. Concluding our study of the magnetic equation of state, we find again consistency with the $O(4)$ scenario. Finally, one would like to judge from the quality of the fits if the $O(4)$ scenario is truly realised and other possibilities are ruled out. However, keeping in mind that one also has to consider the Ising universality class with exponents that differ by less than 20 % from the $O(4)$ exponents, a final statement would need an unprecedented level of accuracy. Nevertheless, this kind of scaling study has appealing features and might even be generalised so to consider leading order coefficients for the expansion in finite chemical potential (see [193]). In order to improve this part of our work it is highly recommended to enlarge the range of temperatures scanned for a fixed pion mass so that one maps out a larger section of the scaling function. Moreover, for approaching the continuum limit and assessing cutoff effects one should eventually apply the scaling study to the renormalised chiral condensate. Since the necessary information might not be available from ETMC, this also introduces the need for dedicated zero-temperature simulations as already suggested before with respect to an improved scale setting.

Our study of the strength of the anomaly has applied screening observables, i. e. both screening masses and the corresponding susceptibilities. The bottom line of this study supplements our previous findings. The anomaly seems to be important at the critical point and thus the $O(4)$ scenario is favoured. Note however, that no measure for the relative strength of the anomaly is available. What we can say is that the anomaly towards the chiral limit even rises. Thus it is hard to think of it as being heavily suppressed near T_c . Whether this trend of a rising anomaly sustains, should also be

investigated with smaller pion masses further lattice spacings.

Concluding our $N_f = 2$ scans, we stress that our pioneering study of thermal QCD with twisted mass fermions has shown that this fermion formulation is indeed suited for this kind of investigations. The explicit breaking of chiral symmetry is, of course, a severe problem which however comes with the advantage of a firm theoretical understanding of the continuum limit. This is very different from staggered fermions which have been predominantly applied up to the present. We think that our physical results are quite reasonable for the first application of a new type of fermions. We find a chiral critical temperature in the expected range and observe behaviour which can be explained by a second order transition of the $O(4)$ universality class in the chiral limit. Very promising is also that cutoff effects seem to be of an acceptable size, cf. figure 5.9, i. e. almost negligible for our current uncertainties and still small for future work with possibly reduced error bars.

Chapter 6 contains our suggestion for the application of $N_f = 2 + 1 + 1$ maximally twisted mass fermions to thermal QCD. This setup is ultimately required for addressing the physical point. Our calculation of the free pressure indicates that additional cutoff effects due to the mass splitting might be rather unimportant for simulations and that thus the observed behaviour might be comparable to the $N_f = 2$ case without further complications.

Overall, in this thesis we provide an extensive study of twisted mass fermions at finite temperature. Work on thermal lattice QCD with Wilson type fermions is very important in order to solidate or revise the results obtained with staggered fermions. This is in particular true as more and more lattice results are used for comparison with heavy ion collisions and as an input to e. g. hydrodynamical descriptions of the QGP. The quality of our results is comparable to current work using clover improved Wilson fermions and our experience reported in this thesis will allow to continue and apply twisted mass QCD to a number of physical questions at finite temperature and eventually even finite chemical potential.

A. Notations and Conventions

A.1. Natural Units

We apply so-called natural units throughout this thesis, i. e. we set

$$\hbar = c = k_B = 1 , \quad (\text{A.1})$$

where all physical quantities are given by some power of energy, usually in MeV, according to their mass dimension. This unit system can be related to the standard SI system by introducing the corresponding values of the constants as quoted e. g. in [39],

$$\hbar = 1.054\,571\,628(53) \cdot 10^{-34} \text{ J s} , \quad (\text{A.2a})$$

$$c = 299\,792\,458 \text{ m s}^{-1} , \quad (\text{A.2b})$$

$$k_B = 1.380\,6504(24) \text{ J K}^{-1} . \quad (\text{A.2c})$$

The only exception from natural units are lattice spacings which are usually given in ‘fm’. Calculating forth and back can be achieved with [39]

$$\hbar c = 197.3269631(49) \text{ MeV fm} . \quad (\text{A.3})$$

A.2. Dirac Matrices and Euclidean Spacetime

The explicit choice of Dirac γ -matrices is not important for this thesis. However, we want to stress the difference between the matrices in Euclidean and Minkowski spacetime. In Minkowski spacetime, following [32], the metric is given by

$$(g_{\mu\nu}) = \begin{pmatrix} 1 & 0 & 0 & 0 \\ 0 & -1 & 0 & 0 \\ 0 & 0 & -1 & 0 \\ 0 & 0 & 0 & -1 \end{pmatrix} \quad (\text{A.4})$$

and the Dirac matrices fulfil

$$\{\gamma_\mu, \gamma_\nu\} = 2g_{\mu\nu} , \quad (\text{A.5})$$

with $\{A, B\} = AB + BA$. Finally, γ_5 is defined via

$$\gamma_5 = i\gamma^0\gamma^1\gamma^2\gamma^3 . \quad (\text{A.6})$$

Performing the Wick rotation $\tau = -it$, we have the Euclidean four-dimensional vector $x_E = (x_1, x_2, x_3, x_4)$ from the Minkowski vector $x_M = (x^0, x^1, x^2, x^3)$ so that

$$|x_E|^2 = (x_E)_\mu (x_E)_\mu = -|x_M|^2 = -(x_M)_\mu (x_M)^\mu . \quad (\text{A.7})$$

The corresponding metric is simply

$$(\delta_{\mu\nu}) = \begin{pmatrix} 1 & 0 & 0 & 0 \\ 0 & 1 & 0 & 0 \\ 0 & 0 & 1 & 0 \\ 0 & 0 & 0 & 1 \end{pmatrix} \quad (\text{A.8})$$

and we have

$$\{\gamma_\mu, \gamma_\nu\} = 2\delta_{\mu\nu} \quad (\text{A.9})$$

for the Dirac matrices. The Euclidean γ_5 is given by

$$\gamma_5 = \gamma_1\gamma_2\gamma_3\gamma_4. \quad (\text{A.10})$$

B. Thermal Transitions in the Bare Phase Diagram

Table B.1 collects the resulting thermal transitions, i. e. the location in (κ, μ_0) -space, from Gaussian fits to signals in our data along with the quantity that gives the best signal. For more details, see the published work [29].

β	κ_t	μ_t	$\kappa_c(T = 0)$	OBSERVABLE
3.75	0.1656(8)	0.005	0.1660	$\chi(P)$
3.75	0.1677(24)	0.005		$ \pi ^2$
3.75	0.1657(5)	0.007		$\chi(P)$
3.75	0.1675(4)	0.007		$\chi(\text{Re}(L))$
3.75	0.16574(24)	0.008		$ \pi ^2$
3.75	0.1658(4)	0.010		$\chi(P)$
3.775	0.1645(1)	0.005		$\chi(P)$
3.8	0.16361(4)	0.005	0.164111	$ \pi ^2$
3.8	0.16621(5)	0.005		$\chi(\text{Re}(L))$
3.9	0.1597(3)	0.005	0.160856	$\chi(\text{Re}(L))$
3.95(10)	0.17	0.005		$\chi(\text{Re}(L))$
4.50(5)	0.0001	0		
4.45(5)	0.05	0		
4.43(5)	0.1	0		

Table B.1.: List of identified thermal transitions, κ_t and — for the β -values discussed here — the observables from which they are extracted. The values of κ_c at zero temperature from ETMC [91] have been added where they are known (as published in [29]).

C. Calculations in the Non-Interacting Limit

C.1. Integrals for the Free Pressure

In order to analytically evaluate the free pressure for lattice fermions from equation (4.4) in analogy to [143], arriving at equation (4.6), one has to solve the finite sum over Matsubara modes ω_n . This is done by means of contour integration as depicted in figure C.1. For infinite Matsubara sums in the continuum a similar procedure is well documented in textbooks [34], for the finite sum on the lattice we are not aware of any earlier application but by Rothe and Kaste [194]. By mapping the discrete sum to an integral along the unit circle they provide an identity for meromorphic functions $g(z)$ that are bounded for $|z| \rightarrow \infty$ and free of singularities for $|z| = 1$,

$$\frac{1}{N_\tau} \sum_{n=-N_\tau/2}^{N_\tau/2-1} g\left(e^{i(\omega_n+i\mu)}\right) = \sum_z \frac{\text{res}\left(\frac{1}{z}g(z)\right)}{e^{N_\tau\mu}z^{N_\tau} + 1}, \quad (\text{C.1})$$

where $\omega_n = (2n + 1)\pi/N_\tau$, $\mu \in \mathbb{R}$ and N_τ even.

With the method above, applied to the derivative of the pressure with respect to $\omega = \sinh(aE)$, one can get equation (4.6) for the pressure [143] and rewrite it for dimensionless integration variables, $y = p/T$,

$$\frac{p}{T^4} = \frac{N_c}{2\pi^3} \int_{\mathbb{R}^3} d^3y \ln\left(1 + e^{-\varepsilon(\mathbf{y}, m/T)}\right), \quad (\text{C.2})$$

where

$$\varepsilon(\mathbf{y}, m/T) = E(\mathbf{p}, m)/T. \quad (\text{C.3})$$

Note that the integration range for the spatial momenta has been extended from $[-\pi/2N_\tau, \pi/2N_\tau]$ to \mathbb{R} . This is allowed for calculations of the power series in $1/N_\tau$ since any further corrections are exponentially suppressed $\sim e^{-\pi N_\tau}$. The advantage of the new integration range is that one can now substitute the Cartesian coordinates by spherical ones. This allows to solve the occurring integrals analytically if $m = 0$ or at least facilitates the numerical integration drastically because of a reduction to one dimension.

In order to expand equation (4.6) or equation (C.2) one needs to identify the contributions of the lattice dispersion relation in powers of the lattice spacing,

$$E(\mathbf{p}) = E_{(0)} + aE_{(1)} + a^2E_{(2)} + \dots. \quad (\text{C.4})$$

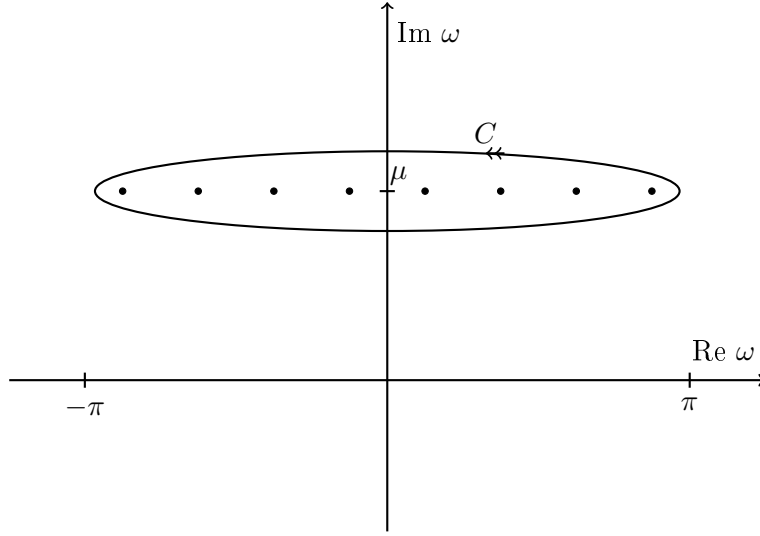


Figure C.1.: Contour integration for finite Matsubara sum on the lattice. In this case we have considered the possibility of a non-vanishing value for the chemical potential μ .

The dispersion relation is obtained from the zeroes of the inverse Euclidean propagator, $S_F^{-1}(\mathbf{p}, p_4 = iE)$, so that for Wilson type fermions one gets

$$E_{(0)} = \sqrt{\mathbf{p}^2 + m_q^2}, \quad (\text{C.5a})$$

$$E_{(1)} = -\frac{m_0}{2} \frac{m_q^2}{\sqrt{\mathbf{p}^2 + m_q^2}}, \quad (\text{C.5b})$$

$$E_{(2)} = -\frac{1}{2\sqrt{\mathbf{p}^2 + m_q^2}} \left(\frac{1}{3}\mathbf{p}^4 + \frac{1}{3}\sum_j p_j^4 + \frac{2}{3}\mathbf{p}^2 m_q^2 + \frac{m_q^4}{12} m_q^4 - m_0^2 m_q^2 + \frac{m_0^2}{4} \frac{m_q^4}{\mathbf{p}^2 + m_q^2} \right). \quad (\text{C.5c})$$

Simplifications and improvement are apparent for maximal twist, i.e. for vanishing untwisted quark mass component $m_0 = 0$. For clover improved fermions m_q has to be replaced by the accordingly shifted quark mass to remove the $\mathcal{O}(a)$ terms, of course.

The only term that breaks rotational invariance to this order of the lattice spacing is the one proportional to $\sum_j p_j^4$ in $E_{(2)}$. All other terms are independent of the angles of spherical coordinates.

The expansion of $E = E_{(0)} + aE_{(1)} + a^2E_{(2)} + \dots$ corresponds to an expansion of the dimensionless function

$$\varepsilon = \varepsilon_{(0)} + \frac{1}{N_\tau} \varepsilon_{(1)} + \frac{1}{N_\tau^2} \varepsilon_{(2)} + \dots \quad (\text{C.6})$$

so that one gets the contributions to the pressure as already stated in section 4.2.1 order

by order from expanding the logarithm of equation (C.2),

$$\frac{p^{(a^0)}(m)}{T^4} = \frac{2N_c}{\pi^2} \int_0^\infty dy y^2 \ln \left(1 + e^{-\varepsilon_{(0)}(y, m/T)} \right) , \quad (\text{C.7a})$$

$$\frac{p^{(a^1)}(m)}{T^4} = -\frac{2N_c}{\pi^2 N_\tau} \int_0^\infty dy y^2 \frac{\varepsilon_{(1)}(y, m/T)}{1 + e^{\varepsilon_{(0)}(y, m/T)}} , \quad (\text{C.7b})$$

$$\begin{aligned} \frac{p^{(a^2)}(m)}{T^4} &= \frac{N_c}{\pi^2 N_\tau^2} \int_0^\infty dy y^2 \frac{\varepsilon_{(1)}^2(y, m/T) e^{\varepsilon_{(0)}(y, m/T)}}{\left(1 + e^{\varepsilon_{(0)}(y, m/T)} \right)^2} \\ &\quad - \frac{N_c}{\pi^2 N_\tau^2} \int_0^\infty dy \int_0^\pi d\vartheta y^2 \sin(\vartheta) \frac{\varepsilon_{(2)}(y, \vartheta, m/T)}{1 + e^{\varepsilon_{(0)}(y, m/T)}} . \end{aligned} \quad (\text{C.7c})$$

The improvement of the pressure is thus directly linked to the improvement of the dispersion relation as the pressure contribution linear in the lattice spacing vanishes if the linear contribution to the dispersion relation is zero. The ϑ -dependence of $\varepsilon_{(2)}$ poses no problem since

$$\int_0^\pi d\vartheta \sin(\vartheta) f(y) \sum_j y_j^4 = 3 \int_{-1}^1 du f(y) u^4 y^4 = \frac{6}{5} y^4 f(y) . \quad (\text{C.8})$$

Thus all integrals can be solved by one-dimensional numerical integration. For vanishing mass, one finds analytic solutions,

$$\frac{p^{(a^0)}(0)}{T^4} = N_c \frac{7}{2} \frac{\pi^2}{90} , \quad (\text{C.9a})$$

$$\frac{p^{(a^1)}(0)}{T^4} = 0 , \quad (\text{C.9b})$$

$$\frac{p^{(a^2)}(0)}{T^4} = \frac{248}{147} \frac{p^{(a^0)}(0)}{T^4} . \quad (\text{C.9c})$$

C.2. Free Lattice Screening Masses

The purpose of this section is to give reasoning for the determination of the free screening mass on the lattice from equation (5.35). For the sake of simplicity, we start with staggered fermions and explain the necessary modifications for Wilson type fermions in the end. The staggered fermion propagator is given by

$$S(p) = a \frac{-i\vec{p} + am_0}{\vec{p}^2 + a^2 m_0^2} . \quad (\text{C.10})$$

Of special importance is the denominator

$$D(p) = \vec{p}^2 + a^2 m_0^2 . \quad (\text{C.11})$$

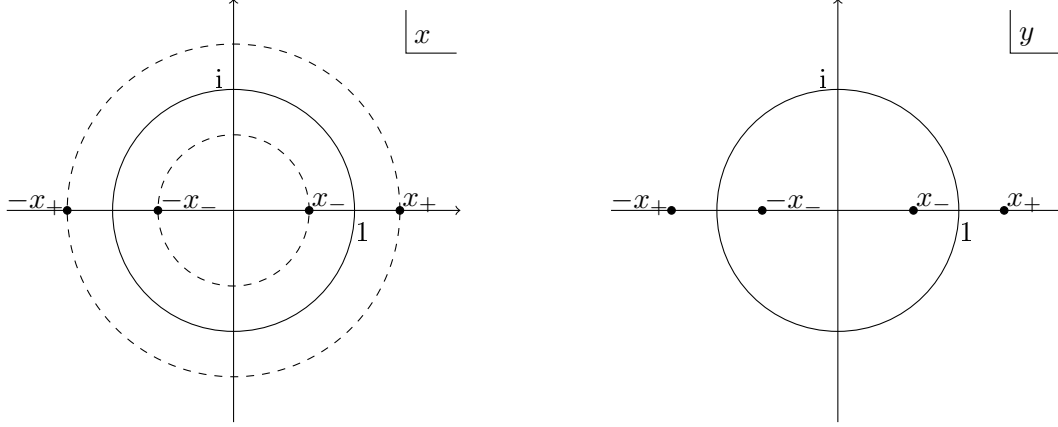


Figure C.2.: Integration contours for the x_- (left) and y_- (right) integration. The poles of the x -integration $\pm yx_{\pm}$ lie on the dashed circles rotated from the indicated positions by the phase factor $y \in \partial D_1(0)$.

Two more shorthand notations that will be convenient from now on are

$$A^2(p_{\perp}, p_4) = \bar{p}_1^2 + \bar{p}_2^2 + \sin^2(ap_4) + a^2 m_0^2, \quad (\text{C.12})$$

$$\tilde{F}(q_3, p_3, p_{\perp}, p_4) = \sin(ap_3) \sin(ap_3 - aq_3) + A^2(p_{\perp}, p_4), \quad (\text{C.13})$$

where we will usually suppress the reference to $p_{\perp} = (p_1, p_2)$ and p_4 . The sum over the Matsubara modes which we denote by \sum_{p_4} will be left for evaluation till later. Hence, the following expression can be constructed from the free propagator for the pseudo-scalar correlator,

$$C_{\pi^{\pm}}(z) = \frac{8N_c}{aN_{\tau}} a^2 \sum_{p_4} \int_{-\pi/a}^{\pi/a} \frac{dq_3}{2\pi} e^{iq_3 z} \int_{\text{BZ}} \frac{d^3 p}{(2\pi)^3} \frac{\sum_{j=1}^3 \bar{p}_j \overline{(p - q_3 \hat{3})}_j + \sin^2(ap_4) + a^2 m_0^2}{D(p)D(p - q_3 \hat{3})}. \quad (\text{C.14})$$

Now we can transform the variables as

$$x = e^{iaq_3}, \quad y = e^{iap_3} \quad (\text{C.15})$$

switching to closed contours of integration along $\partial D_1(0)$.

As functions of x and y we have

$$D(p+q) \rightarrow -\frac{1}{4x^2 y^2} (x - yx_-)(x + yx_-)(x - yx_+)(x + yx_+), \quad (\text{C.16})$$

$$D(p) \rightarrow -\frac{1}{4y^2} (y - x_-)(y + x_-)(y - x_+)(y + x_+), \quad (\text{C.17})$$

$$\tilde{F}(p, q) \rightarrow F(x, y^2) = A^2 - \frac{1}{4} \left(\frac{y^2}{x} - x - \frac{1}{x} + \frac{x}{y^2} \right). \quad (\text{C.18})$$

x_{\pm} are the positive roots as obtained from

$$x_{\pm}^2 = 1 + 2A^2 \pm 2A\sqrt{1 + A^2}. \quad (\text{C.19})$$

It is important to note that

$$x_-^2 < 1 + 2A^2 - 2A\sqrt{A^2} = 1 \quad (\text{C.20a})$$

$$|x_+^2| = |1 + 2A^2 + 2A\sqrt{1 + A^2}| > 1 \quad (\text{C.20b})$$

since A is strictly positive. Furthermore, x_-^2 can be shown to be positive because assuming otherwise, we have

$$\begin{aligned} x_-^2 < 0 &\Leftrightarrow 1 + 2A^2 - 2A\sqrt{1 + A^2} < 0 \\ &\Leftrightarrow 1 + 2A^2 < 2A\sqrt{1 + A^2} \\ &\Rightarrow 1 + 4A^2 + 4A^4 < 4A^2 + 4A^4 \\ &\Leftrightarrow 1 < 0 \quad \zeta. \end{aligned} \quad (\text{C.21})$$

Because we really look at both roots, we are free to define x_- to be positive. After all this gives a pole structure where $x = \pm yx_-$ are within $\partial D_1(0)$ and have thus to be considered for the sum of residues for the x -integration. Evaluating the x - and y -integrals, the correlator can be expressed as

$$\begin{aligned} C_{\pi^\pm}(z) = \frac{8N_c}{aN_\tau} \sum_{p_4} \int_{\text{BZ}} \frac{d^2 p_\perp}{(2\pi)^2} &\left\{ \frac{8F(x_-^2, x_-^2)(x_-)^{2z/a}}{(x_- - x_+)^2(x_- + x_+)^2} \right. \\ &\left. + \frac{8F(-x_-^2, x_-^2)(x_-)^{z/a}(-x_-)^{z/a}}{(x_- - x_+)^2(x_- + x_+)^2} \right\} \end{aligned} \quad (\text{C.22})$$

where the term in the second line vanishes because $F(-x_-^2, x_-^2) = 0$. On the other hand $F(x_-^2, x_-^2) = 2A^2$, thus one finally gets

$$C_{\pi^\pm}(z) = \frac{8N_c}{aN_\tau} \sum_{p_4} \int_{\text{BZ}} \frac{d^2 p_\perp}{(2\pi)^2} \frac{(x_-)^{2z/a}}{1 + A^2}. \quad (\text{C.23})$$

The z -dependence can now be rewritten as

$$(x_-^2)^{z/a} = \exp(z/a \ln(x_-^2)) = \exp(-2 \sinh^{-1}(A)z/a). \quad (\text{C.24})$$

Therefore up to the p_\perp -integration, there is an exponential decay for each Matsubara mode. The p_\perp -dependence of the exponent can be expressed in a power series so that for arbitrarily large z this dependence is exponentially suppressed and it is sufficient to look at $p_\perp = 0$. Furthermore, since the Matsubara modes give contributions to the bare quark mass as $am_0 + \sin(ap_4)$, the exponential decay is governed by the smallest possible values $p_4 = \pm\pi T$ only. After all, the final result is

$$M_{\text{scr}} = 2 \sinh^{-1}(A(p_\perp = 0, p_4 = \pm\pi T)) \quad (\text{C.25})$$

which is the same screening mass as defined by equation (5.35) for staggered fermions.

The difference for Wilson type fermions is that their denominator D really is a function of $p/2$ due to the Wilson term. Thus it can be written as

$$D(p - q) = 4(1 + M(p_\perp, p_4)) (\sin^2(ap_3/2 - aq/2) + A_W^2(p_\perp, p_4)) \quad (\text{C.26})$$

where $M(p_\perp, p_4) = \frac{1}{2}\hat{p}_\perp^2 + am_0 + 2\sin^2(ap_4/2)$. The definition of A_W for Wilson fermions has to be

$$A_W^2(p_\perp, p_4) = \frac{\bar{p}_\perp^2 + M^2(p_\perp, p_4) + a^2\mu_0^2 + \sin^2(ap_4)}{4(1 + M(p_\perp, p_4))}. \quad (\text{C.27})$$

Using

$$x = e^{iaq_3/2}, \quad y = e^{iap_3/2}, \quad (\text{C.28})$$

the same integration contours and pole structure as before for staggered fermions are obtained when making use of the periodicity of the integrand, i. e. when employing

$$\int_{-\pi/a}^{\pi/a} dq \dots = \frac{1}{2} \int_{-2\pi/a}^{2\pi/a} dq \dots. \quad (\text{C.29})$$

The only remaining difference is a factor of 2 in the exponential z -dependence:

$$C_{\pi^\pm}(z) \sim e^{2z/a \ln x_-^2}. \quad (\text{C.30})$$

This is exactly the relation that is needed to reproduce the definition from equation (5.35),

$$\begin{aligned} (aM_{\text{scr}})_W &= -2 \ln \left(1 + 2A_W^2 - 2A_W \sqrt{1 + A_W^2} \right) \Big|_{p_\perp=0, p_4=\pm\pi T} \\ &= 4 \sinh^{-1}(A_W(p_\perp = 0, p_4 = \pm\pi T)). \end{aligned} \quad (\text{C.31})$$

D. Simulation Details

D.1. Interpolation of κ_c

Our interpolation of κ_c is done by the Padé

$$\kappa_c(\beta) = \frac{1 + a_1\beta + a_2\beta^2}{b_0 + b_1\beta + b_2\beta^2} \quad (\text{D.1})$$

with

$$a_1 = -0.6657552988487317 , \quad (\text{D.2a})$$

$$a_2 = 0.11369888737867674 , \quad (\text{D.2b})$$

$$b_0 = 7.644906897056625 , \quad (\text{D.2c})$$

$$b_1 = -5.022518375934722 , \quad (\text{D.2d})$$

$$b_2 = 0.8395272298528993 . \quad (\text{D.2e})$$

The values of κ_c from ETMC are listed in table D.1.

β	κ_c
3.75	0.1660
3.8	0.164111
3.9	0.160856
4.05	0.157010
4.2	0.154073

Table D.1.: Values of $\kappa_c(\beta)$ from ETMC [23], $\kappa_c(\beta = 3.75)$ is known from personal communication with K. Jansen.

D.2. Monte-Carlo Data

Figures D.1, D.2 and D.3 supplement figure 5.7. Runs A12, B12 and C12@($\beta = 4.060$) have been performed on the HLRN cluster in Berlin, runs B10 and all other points of C12 on the APEnext in Rome. The runs do not share the same algorithmic parameters such as trajectory length or number of integration steps in the leapfrog integrator. In particular, the trajectory length was 1 on the HLRN cluster and 0.5 on the APE. The statistics that the different simulation points have reached are summarised in table D.2.

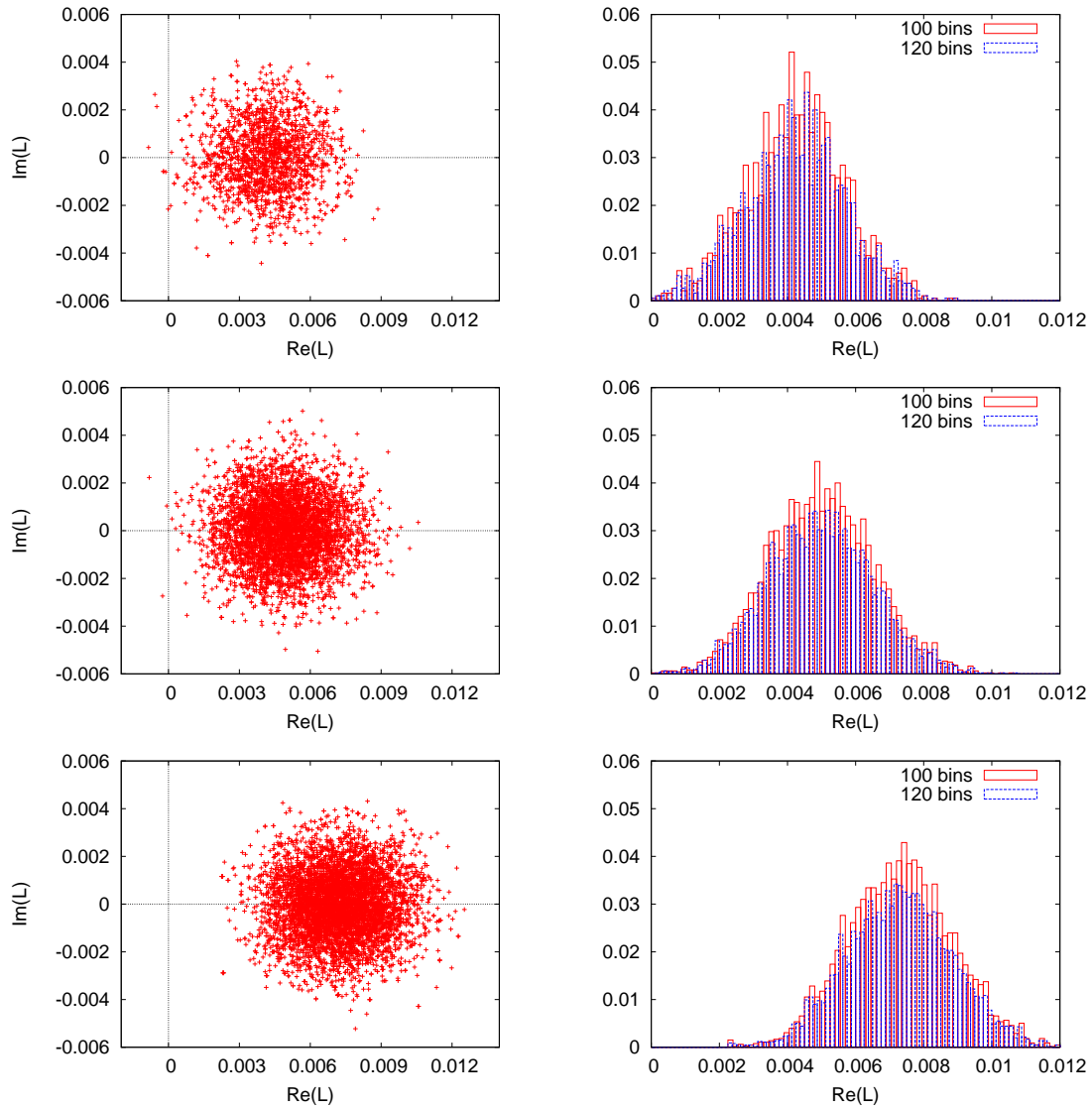


Figure D.1.: Scatter plots for $\text{Im}(L)$ vs. $\text{Re}(L)$ (left) and histograms for $\text{Re}(L)$ (right) from run B10. From top to bottom we show the according plots for $\beta = 3.850, 3.885$ and 3.940 .

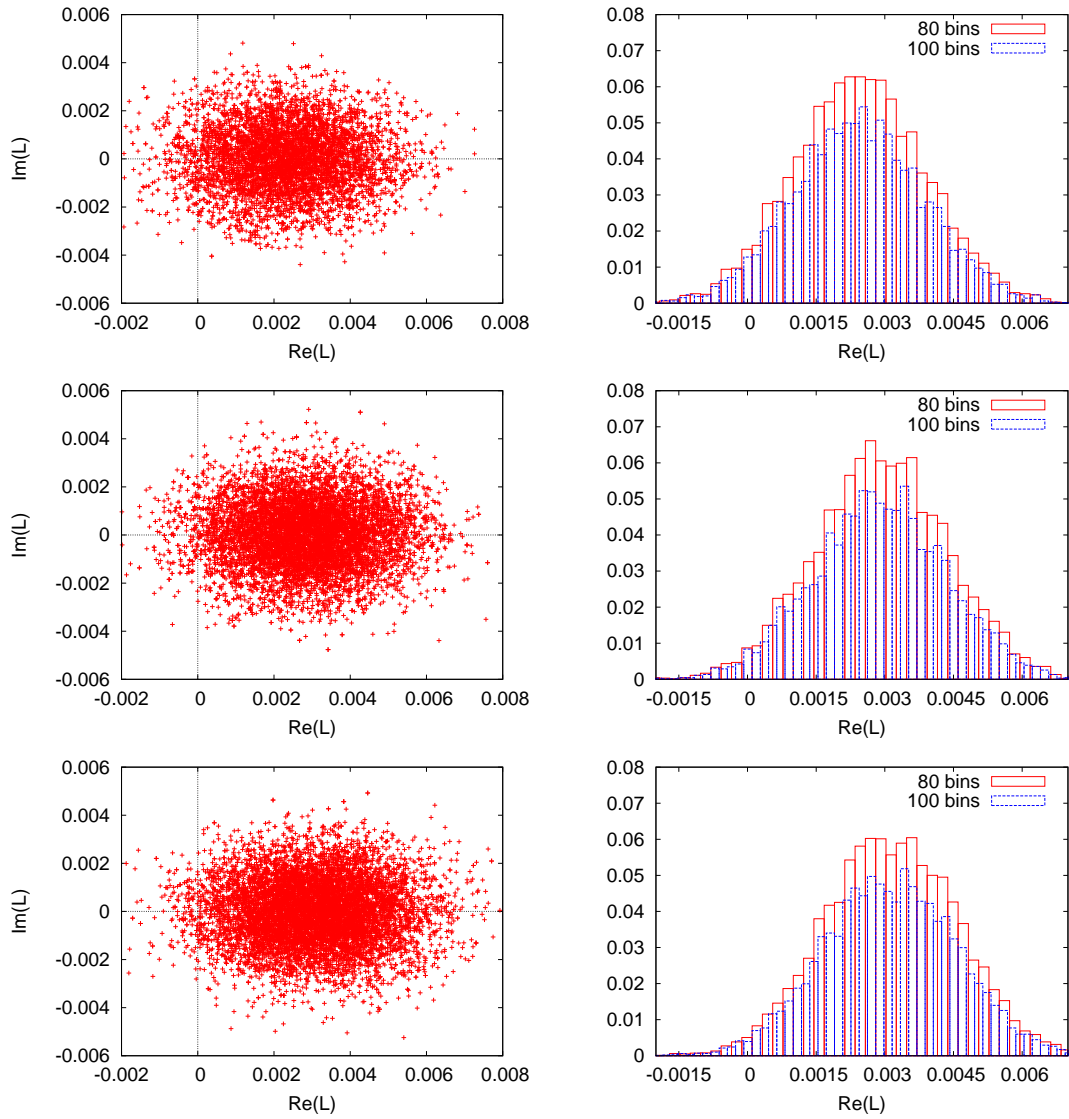


Figure D.2.: Scatter plots for $\text{Im}(L)$ vs. $\text{Re}(L)$ (left) and histograms for $\text{Re}(L)$ (right) from run B12. From top to bottom we show the according plots for $\beta = 3.995, 4.015$ and 4.025 .

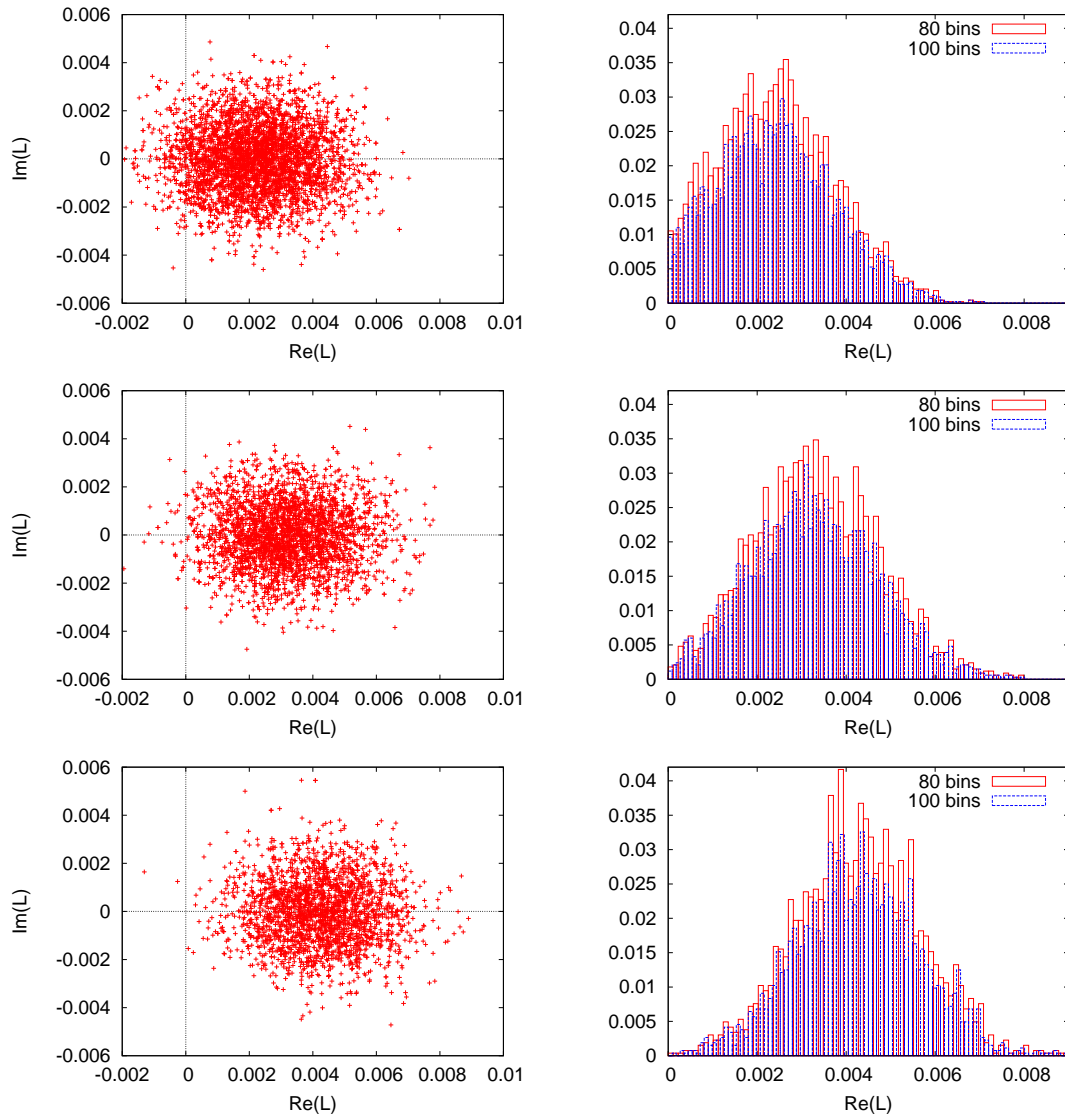


Figure D.3.: Scatter plots for $\text{Im}(L)$ vs. $\text{Re}(L)$ (left) and histograms for $\text{Re}(L)$ (right) from run C12. From top to bottom we show the according plots for $\beta = 4.020, 4.040$ and 4.070 .

A12		B10		B12		C12	
β	STAT	β	STAT	β	STAT	β	STAT
3.9000	3747	3.8500	1900	3.9500	2783	4.0100	4040
3.9300	3447	3.8650	1950	3.9700	3268	4.0200	4520
3.9450	4339	3.8700	4400	3.9900	5089	4.0300	5640
3.9525	5461	3.8750	2100	3.9950	6486	4.0400	3480
3.9600	5516	3.8800	4058	4.0000	6298	4.0500	4640
3.9675	6612	3.8850	4900	4.0100	6403	4.0600	5523
3.9750	4005	3.8900	6289	4.0125	10139	4.0700	2790
3.9900	4296	3.8950	2950	4.0150	8950		
4.0150	2060	3.9000	4473	4.0175	11673		
		3.9100	5750	4.0200	10003		
		3.9300	6550	4.0250	9878		
				4.0300	5245		
				4.0400	5350		

Table D.2.: Statistics for gauge observables from our simulations. Note that trajectory length differs between the runs.

D.3. Gaussian Fits

In this section, we collect the fits to Gaussians,

$$f(\beta) = A \exp\left(-\frac{(\beta - \beta_{\text{peak}})^2}{2\sigma^2}\right), \quad (\text{D.3})$$

for the critical regions of our observables and show them together with the data. Note that in the following tables we give the fitted peak position β_{peak} with the according error. This determines the central value for the critical coupling β_c . Our error estimate for β_c is then obtained from the total width of the identified fit region in order to have a reliable value, see table 5.3. We also include some exemplary plots in which the uncertainty assigned to β_c is visualised by the range for the Gaussian function.

D.3.1. Run A12

QUANTITY	β_{peak}	A	σ	χ^2/dof
$\chi_{\text{Re}(L)}$	3.9604(31)	$1.986(34) \cdot 10^{-6}$	0.049(17)	0.524514
$\sigma^2(\overline{\psi\psi})$	3.9400(96)	$2.65(34) \cdot 10^{-4}$	0.030(15)	0.208793
χ_P	3.9590(17)	$6.71(63) \cdot 10^{-8}$	0.0164(79)	(three point fit)
$\tau_{\text{int}}(P)$	3.9562(193)	15.2(4.4)	0.036(45)	0.146516
$\tau_{\text{int}}(\text{Re}(L))$	3.9651(90)	4.6(1.2)	0.029(12)	0.083121
$\tau_{\text{int}}(\overline{\psi\psi})$	3.9601(47)	2.43(62)	0.018(11)	0.148487

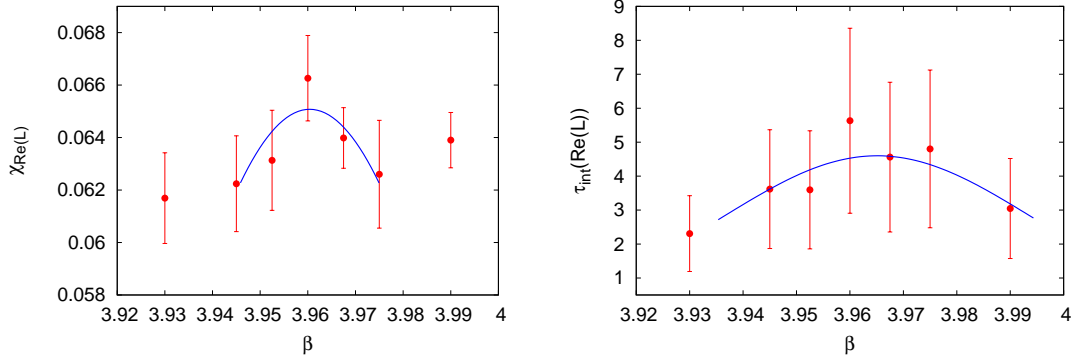


Figure D.4.: Signals of $\text{Re}(L)$ from run A12. Susceptibility (left) and integrated autocorrelation time (right).

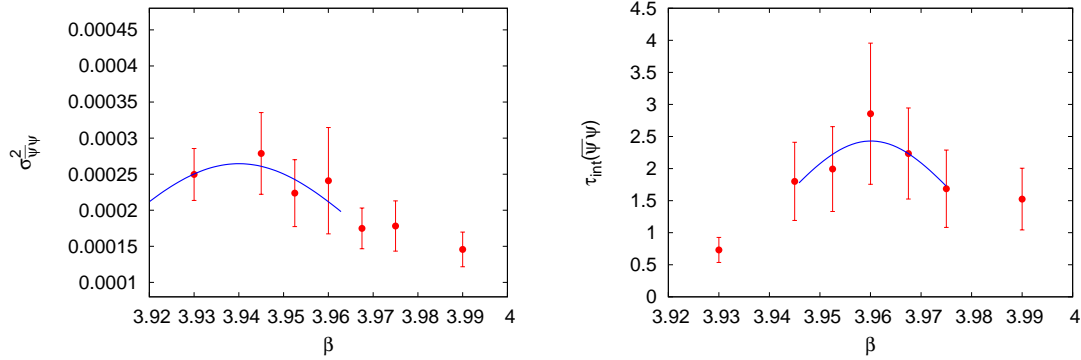


Figure D.5.: Signals of $\langle\overline{\psi}\psi\rangle$ from run A12. Variance (left) and integrated autocorrelation time (right).

D.3.2. Run B10

QUANTITY	β_{peak}	A	σ	χ^2/dof
$\chi_{\text{Re}(L)}$	3.8931(49)	$2.432(58) \cdot 10^{-6}$	0.037(14)	1.35185
$\sigma^2(\overline{\psi}\psi)$	3.8804(4)	$4.54(496) \cdot 10^{-4}$	0.0038(4)	(three point fit)
χ_P	3.8807(34)	$7.85(29) \cdot 10^{-8}$	0.038(16)	0.978101
$\tau_{\text{int}}(P)$	3.8807(6)	33(19)	0.033(91)	(three point fit)
$\tau_{\text{int}}(\text{Re}(L))$	3.8898(68)	9.9(1.8)	0.0158(54)	2.24444

D.3.3. Run B12

QUANTITY	β_{peak}	A	σ	χ^2/dof
$\chi_{\text{Re}(L)}$	4.02053(86)	$2.115(34) \cdot 10^{-6}$	0.050(25)	0.454302
$\sigma^2(\overline{\psi}\psi)$	4.0150(11)	$1.36(17) \cdot 10^{-4}$	0.0072(27)	0.0235771
χ_P	4.0140(13)	$5.08(17) \cdot 10^{-8}$	0.0125(41)	0.0464607
$\tau_{\text{int}}(P)$	4.0147(49)	7.2(2.1)	0.0089(66)	0.395145
$\tau_{\text{int}}(\text{Re}(L))$	4.0060(16)	9.3(4.2)	0.0056(27)	0.0772021
$\tau_{\text{int}}(\overline{\psi}\psi)$	4.0176(48)	7.7(1.4)	0.014(14)	0.814068

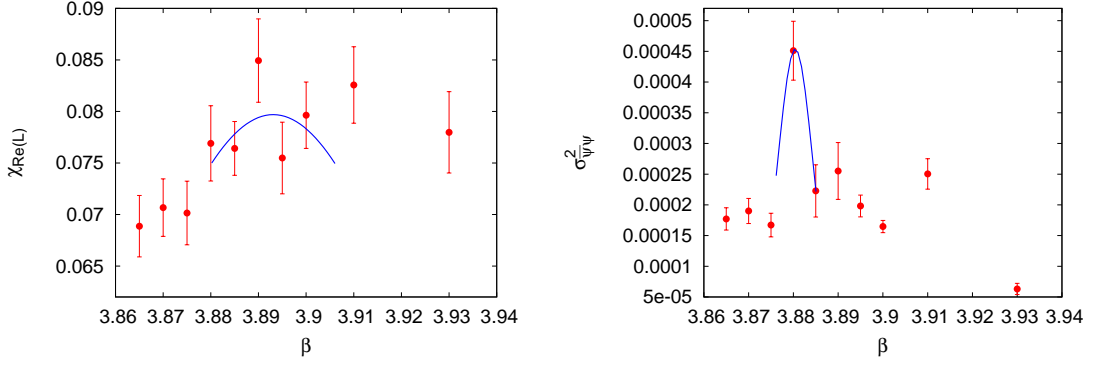


Figure D.6.: Run B10. Left: Susceptibility of $\text{Re}(L)$. Right: Variance of $\langle \overline{\psi\psi} \rangle$.

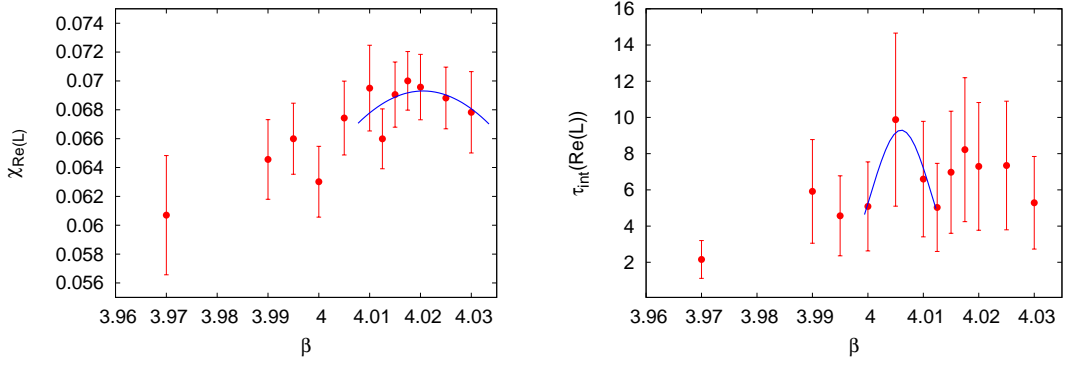


Figure D.7.: Signals of $\text{Re}(L)$ from run B12. Susceptibility (left) and integrated autocorrelation time (right).

D.3.4. Run C12

QUANTITY	β_{peak}	A	σ	χ^2/dof
$\chi_{\text{Re}(L)}$	4.0432(60)	$2.136(56) \cdot 10^{-6}$	0.074(38)	0.110543
$\sigma^2(\overline{\psi\psi})$	4.0298(11)	$1.48(16) \cdot 10^{-4}$	0.0164(16)	0.189259
χ_P	4.0268(42)	$4.70(16) \cdot 10^{-8}$	0.056(19)	0.49604
$\tau_{\text{int}}(P)$	4.0262(47)	12(5)	0.017(6)	0.212751
$\tau_{\text{int}}(\text{Re}(L))$	4.0312(110)	13(4)	0.028(12)	0.22671

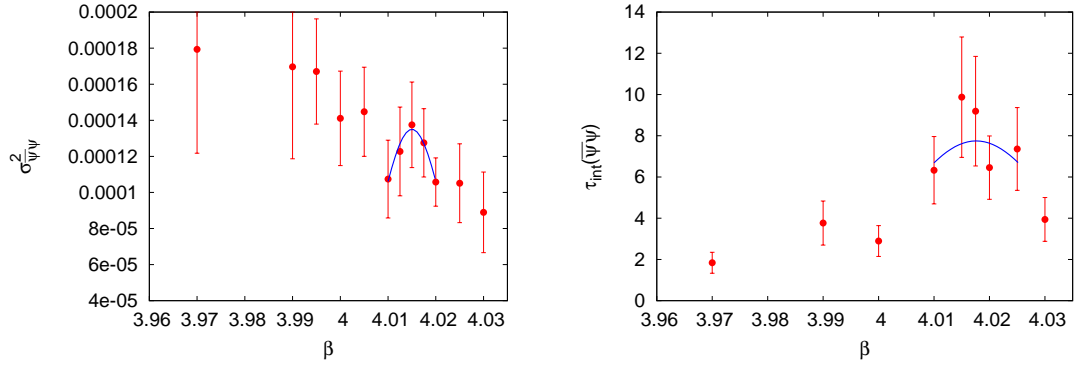


Figure D.8.: Signals of $\langle \bar{\psi}\psi \rangle$ from run B12. Variance (left) and integrated autocorrelation time (right).

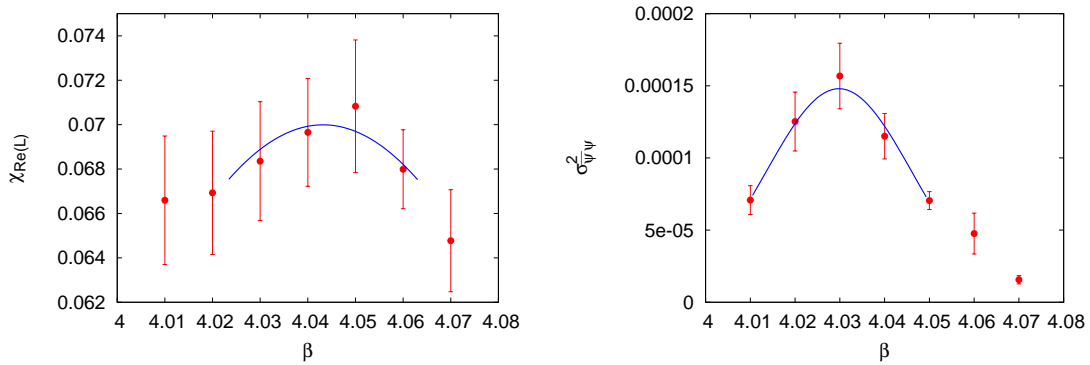


Figure D.9.: Run C12. Left: Susceptibility of $\text{Re}(L)$. Right: Variance of $\langle \bar{\psi}\psi \rangle$.

D.4. Results of Screening Mass Fits

The fit results are based on the local effective mass, cf. equation (5.31). Pseudo-scalar and scalar screening masses refer to the charged flavour multiplet channel. Determination of the scalar mass has not always been possible. The number of available correlators from individual configurations is given in table D.3.

A12		B10		B12		C12	
β	#data	β	#data	β	#data	β	#data
3.9000	653	3.8500	360	3.9500	261	4.0100	464
3.9300	678	3.8650	345	3.9700	299	4.0200	512
3.9450	738	3.8700	545	3.9900	349	4.0300	624
3.9525	530	3.8750	380	4.0000	576	4.0500	524
3.9600	744	3.8800	574	4.0100	391	4.0600	1430
3.9675	1316	3.8850	640	4.0200	450		
3.9750	925	3.8900	778				
3.9900	1017	3.8950	445				
4.0150	438	3.9000	567				
		3.9100	725				
		3.9300	805				

Table D.3.: Number of correlators from individual configuration available for the screening mass fits.

D.4.1. Run A12

Pseudo-scalar screening mass from A12				Scalar screening mass from A12			
β	aM_{scr}	χ^2/dof	RANGE	β	aM_{scr}	χ^2/dof	RANGE
3.9000	0.1667(16)	0.18	[10,15]	3.9000	0.52(17)	0.17	[8,11]
3.9300	0.1704(16)	0.80	[10,15]	3.9300	0.87(51)	0.02	[8,9]
3.9450	0.1662(35)	0.71	[10,15]	3.9450			
3.9525	0.1721(25)	1.09	[10,15]	3.9525	0.51(10)	0.04	[8,13]
3.9600	0.2067(24)	1.82	[10,15]	3.9600	0.42(05)	1.08	[8,10]
3.9675	0.1955(19)	0.11	[10,15]	3.9675	0.56(07)	0.41	[8,10]
3.9750	0.2015(21)	0.80	[10,15]	3.9750	0.54(13)	0.21	[8,12]
3.9900	0.1949(34)	1.50	[10,15]	3.9900			
4.0150	0.2448(40)	1.06	[10,15]	4.0150	0.44(03)	0.32	[8,13]

D.4.2. Run B10

Pseudo-scalar screening mass from B10

β	aM_{scr}	χ^2/dof	RANGE
3.8500	0.2360(24)	0.91	[8,15]
3.8650	0.2527(25)	2.07	[8,15]
3.8700	0.2456(26)	1.98	[10,15]
3.8750	0.2674(22)	0.85	[8,15]
3.8800	0.2386(26)	1.01	[10,15]
3.8850	0.2623(20)	2.49	[8,15]
3.8900	0.2831(18)	1.34	[8,15]
3.8950	0.2897(38)	0.75	[10,15]
3.9000	0.2944(21)	1.67	[10,15]
3.9100	0.2787(23)	2.61	[8,15]
3.9300	0.3197(35)	7.08	[10,15]

D.4.3. Run B12

Pseudo-scalar screening mass from B12

β	aM_{scr}	χ^2/dof	RANGE
3.9500	0.2015(22)	0.63	[10,15]
3.9700	0.1997(22)	0.23	[8,15]
3.9900	0.2161(21)	0.97	[9,15]
4.0000	0.2085(22)	1.38	[8,15]
4.0100	0.2200(30)	2.14	[10,15]
4.0200	0.2199(21)	3.32	[8,15]

Scalar screening mass from B12

β	aM_{scr}	χ^2/dof	RANGE
3.9500	0.32(5)	0.15	[10,15]
3.9700	0.32(4)	0.51	[8,15]
3.9900			
4.0000			
4.0100	0.34(2)	0.90	[10,15]
4.0200			

D.4.4. Run C12

Pseudo-scalar screening mass from C12

β	aM_{scr}	χ^2/dof	RANGE
4.0100	0.2435(18)	4.03	[10,15]
4.0200	0.2093(19)	2.07	[9,15]
4.0300	0.2378(21)	0.98	[10,15]
4.0500	0.2742(30)	1.34	[10,15]
4.0600	0.2742(30)	5.36	[10,15]

Scalar screening mass from C12

β	aM_{scr}	χ^2/dof	RANGE
4.0100	0.408(13)	0.28	[8,11]
4.0200			
4.0300			
4.0500	0.680(120)	0.13	[8,11]
4.0600	0.540(030)	0.52	[8,11]

Bibliography

- [1] H. D. Politzer, “Reliable Perturbative Results For Strong Interactions?,” *Phys. Rev. Lett.* **30** (1973) 1346–1349.
- [2] D. J. Gross and F. Wilczek, “Ultraviolet Behavior of Non-Abelian Gauge Theories,” *Phys. Rev. Lett.* **30** (1973) 1343–1346.
- [3] D. H. Perkins, *Introduction to High Energy Physics*. Cambridge University Press, Cambridge, UK, 4th ed., 2000.
- [4] A. Linde, “Infrared Problem in Thermodynamics of the Yang-Mills Gas,” *Phys. Lett.* **B96** (1980) 289.
- [5] K. Fukushima and T. Hatsuda, “The phase diagram of dense QCD,” *Rept. Prog. Phys.* **74** (2011) 014001, [arXiv:1005.4814 \[hep-ph\]](#).
- [6] K. G. Wilson, “Confinement of Quarks,” *Phys. Rev.* **D10** (1974) 2445–2459.
- [7] M. Creutz, L. Jacobs, and C. Rebbi, “Experiments with a Gauge Invariant Ising System,” *Phys. Rev. Lett.* **42** (1979) 1390.
- [8] M. Creutz, “Confinement and the Critical Dimensionality of Space-Time,” *Phys. Rev. Lett.* **43** (1979) 553–556.
- [9] M. Creutz, “Monte Carlo Study of Quantized SU(2) Gauge Theory,” *Phys. Rev.* **D21** (1980) 2308–2315.
- [10] P. de Forcrand, “Simulating QCD at finite density,” *PoS Lat2009* (2009) 010, [arXiv:1005.0539 \[hep-lat\]](#).
- [11] J. B. Kogut and L. Susskind, “Hamiltonian Formulation of Wilson’s Lattice Gauge Theories,” *Phys. Rev.* **D11** (1975) 395.
- [12] K. Kanaya, “Finite Temperature QCD on the Lattice – Status 2010,” *PoS Lat2010* (2010) 012, [arXiv:1012.4247 \[hep-lat\]](#).
- [13] S. Gupta, “QCD at finite density,” *PoS Lat2010* (2010) 007, [arXiv:1101.0109 \[hep-lat\]](#).
- [14] K. Jansen, “Lattice QCD: a critical status report,” *PoS Lat2008* (2008) 010, [arXiv:0810.5634 \[hep-lat\]](#).
- [15] M. Creutz, “Why rooting fails,” *PoS Lat2007* (2007) 007, [arXiv:0708.1295 \[hep-lat\]](#).
- [16] A. Kronfeld, “Lattice gauge theory with staggered fermions: How, where, and why (not),” *PoS Lat2007* (2007) 016, [arXiv:0711.0699 \[hep-lat\]](#).

- [17] Y. Aoki, G. Endrodi, Z. Fodor, S. D. Katz, and K. K. Szabo, “The Order of the quantum chromodynamics transition predicted by the standard model of particle physics,” *Nature* **443** (2006) 675–678, [arXiv:hep-lat/0611014](#) [[hep-lat](#)].
- [18] P. de Forcrand and O. Philipsen, “The Chiral critical line of $N(f) = 2+1$ QCD at zero and non-zero baryon density,” *JHEP* **0701** (2007) 077, [arXiv:hep-lat/0607017](#) [[hep-lat](#)].
- [19] **Wuppertal-Budapest** Collaboration, S. Borsanyi *et al.*, “Is there still any T_c mystery in lattice QCD? Results with physical masses in the continuum limit III,” *JHEP* **1009** (2010) 073, [arXiv:1005.3508](#) [[hep-lat](#)].
- [20] M. Cheng *et al.*, “Equation of State for physical quark masses,” *Phys. Rev.* **D81** (2010) 054504, [arXiv:0911.2215](#) [[hep-lat](#)].
- [21] **Wuppertal-Budapest** Collaboration, S. Borsanyi *et al.*, “ $N_f=2+1$ flavour equation of state,” *PoS Lat2010* (2010) 171, [arXiv:1011.4229](#) [[hep-lat](#)].
- [22] G. Boyd *et al.*, “Thermodynamics of SU(3) lattice gauge theory,” *Nucl. Phys.* **B469** (1996) 419–444, [arXiv:hep-lat/9602007](#) [[hep-lat](#)].
- [23] **ETM** Collaboration, R. Baron *et al.*, “Light Meson Physics from Maximally Twisted Mass Lattice QCD,” *JHEP* **1008** (2010) 097, [arXiv:0911.5061](#) [[hep-lat](#)].
- [24] **ETM** Collaboration, R. Baron *et al.*, “Light hadrons from lattice QCD with light (u,d), strange and charm dynamical quarks,” *JHEP* **1006** (2010) 111, [arXiv:1004.5284](#) [[hep-lat](#)].
- [25] E.-M. Ilgenfritz *et al.*, “Twisted mass QCD thermodynamics: First results on apeNEXT,” *PoS Lat2006* (2006) 140, [arXiv:hep-lat/0610112](#).
- [26] **tmfT** Collaboration, E.-M. Ilgenfritz, O. Philipsen, L. Zeidlewicz, *et al.*, “Twisted mass QCD at finite temperature,” *PoS Lat2007* (2007) 238, [arXiv:0710.0569](#) [[hep-lat](#)].
- [27] **tmfT** Collaboration, E.-M. Ilgenfritz, O. Philipsen, L. Zeidlewicz, *et al.*, “The finite-temperature phase structure of lattice QCD with twisted-mass Wilson fermions,” *PoS Lat2008* (2008) 206, [arXiv:0809.5228](#) [[hep-lat](#)].
- [28] **tmfT** Collaboration, M. Müller-Preußker, O. Philipsen, L. Zeidlewicz, *et al.*, “On the phase structure of lattice QCD with twisted-mass Wilson fermions at non-zero temperature,” *PoS Lat2009* (2009) 266, [arXiv:0912.0919](#) [[hep-lat](#)].
- [29] **tmfT** Collaboration, E.-M. Ilgenfritz, O. Philipsen, L. Zeidlewicz, *et al.*, “Phase structure of thermal lattice QCD with $N_f=2$ twisted mass Wilson fermions,” *Phys. Rev.* **D80** (2009) 094502, [arXiv:0905.3112](#) [[hep-lat](#)].
- [30] **tmfT** Collaboration, F. Burger, O. Philipsen, L. Zeidlewicz, *et al.*, “Thermal transition temperature from twisted mass QCD,” *PoS Lat2010* (2010) 220, [arXiv:1009.3758](#) [[hep-lat](#)].

-
- [31] O. Philipsen and L. Zeidlewicz, “Cutoff effects of Wilson fermions on the QCD equation of state to $O(g^2)$,” *Phys. Rev.* **D81** (2010) 077501, [arXiv:0812.1177 \[hep-lat\]](#).
- [32] M. E. Peskin and D. V. Schroeder, *An Introduction to quantum field theory*. Addison-Wesley, Reading, USA, 1995.
- [33] L. H. Ryder, *Quantum Field Theory*. Cambridge University Press, Cambridge, UK, 1985.
- [34] J. I. Kapusta and C. Gale, *Finite-temperature field theory: Principles and applications*. Cambridge University Press, Cambridge, UK, 2006.
- [35] J. Ellis, “Searching for Particle Physics Beyond the Standard Model at the LHC and Elsewhere,” [arXiv:1102.5009 \[hep-ph\]](#). Talk presented at the 11th conference on “Frontiers of Fundamental Physics”, Paris, July 2010.
- [36] M. Gell-Mann, “A Schematic Model of Baryons and Mesons,” *Phys. Lett.* **8** (1964) 214–215.
- [37] G. Zweig, “An SU(3) model for strong interaction symmetry and its breaking.”. CERN-TH 401, CERN-TH 412. In Lichtenberg, D. B. (Ed.), Rosen, S. P. (Ed.): *Developments In The Quark Theory Of Hadrons*, Vol. 1, Nonantum, Mass., Hadronic Press, 1980.
- [38] C.-N. Yang and R. L. Mills, “Conservation of Isotopic Spin and Isotopic Gauge Invariance,” *Phys. Rev.* **96** (1954) 191–195.
- [39] **Particle Data Group** Collaboration, K. Nakamura *et al.*, “Review of particle physics,” *J. Phys. G* **G37** (2010) 075021.
- [40] J. Gasser and H. Leutwyler, “Quark Masses,” *Phys. Rept.* **87** (1982) 77–169.
- [41] D. Pisarski, R. and F. Wilczek, “Remarks on the Chiral Phase Transition in Chromodynamics,” *Phys. Rev.* **D29** (1984) 338–341.
- [42] E. V. Shuryak, *The QCD Vacuum, Hadrons and Superdense Matter*. World Scientific, Singapore, 2nd ed., 2004.
- [43] S. R. Sharpe, “Applications of chiral perturbation theory to lattice QCD,” [arXiv:hep-lat/0607016](#). Lectures given at ILFTN Workshop on “Perspectives in Lattice QCD”, Nara, Japan, 2005.
- [44] J. C. Collins and M. J. Perry, “Superdense Matter: Neutrons Or Asymptotically Free Quarks?,” *Phys. Rev. Lett.* **34** (1975) 1353.
- [45] K. Kajantie, M. Laine, K. Rummukainen, and Y. Schröder, “The Pressure of hot QCD up to $g_6 \ln(1/g)$,” *Phys. Rev.* **D67** (2003) 105008, [arXiv:hep-ph/0211321 \[hep-ph\]](#).
- [46] O. Philipsen, D. Bielecki, and Y. Schröder, “Screened perturbation theory for 3d Yang-Mills theory and the magnetic modes of hot QCD,” *PoS QCD-TNT09* (2009) 052, [arXiv:0911.3595 \[hep-ph\]](#).

- [47] N. Su, “QCD Thermodynamics at Intermediate Coupling,” [arXiv:1012.3377 \[hep-ph\]](#). To appear in the proceedings of “Quark Confinement and the Hadron Spectrum IX”, Madrid, Spain, 2010.
- [48] P. Braun-Munzinger and J. Stachel, “The quest for the quark-gluon plasma,” *Nature* **448** (2007) 302–309.
- [49] P. Braun-Munzinger and J. Wambach, “Colloquium: Phase diagram of strongly interacting matter,” *Rev. Mod. Phys.* **81** (2009) 1031–1050.
- [50] F. Gelis, “Color Glass Condensate and Glasma,” *Nucl. Phys.* **A854** (2011) 10–17, [arXiv:1009.0093 \[hep-ph\]](#). In: Proceedings of the RIKEN BNL Research Center Workshop on “Saturation, the Color Glass Condensate and Glasma: What Have we Learned from RHIC?”, Volume 98. May 2010.
- [51] P. Braun-Munzinger, K. Redlich, and J. Stachel, “Particle production in heavy ion collisions,” [arXiv:nucl-th/0304013 \[nucl-th\]](#). Published in Quark Gluon Plasma 3, eds. R. C. Hwa and Xin-Nian Wang, World Scientific Publishing, Singapore 2004.
- [52] P. Braun-Munzinger, J. Stachel, and C. Wetterich, “Chemical freezeout and the QCD phase transition temperature,” *Phys.Lett.* **B596** (2004) 61–69, [arXiv:nucl-th/0311005 \[nucl-th\]](#).
- [53] L. D. McLerran and R. D. Pisarski, “Phases of cold, dense quarks at large $N(c)$,” *Nucl.Phys.* **A796** (2007) 83–100, [arXiv:0706.2191 \[hep-ph\]](#).
- [54] A. Andronic *et al.*, “Hadron Production in Ultra-relativistic Nuclear Collisions: Quarkyonic Matter and a Triple Point in the Phase Diagram of QCD,” *Nucl. Phys.* **A837** (2010) 65–86, [arXiv:0911.4806 \[hep-ph\]](#).
- [55] I. Montvay and G. Münster, *Quantum fields on a lattice*. Cambridge University Press (Cambridge monographs on mathematical physics), Cambridge, UK, 1994.
- [56] H. J. Rothe, *Lattice gauge theories: An Introduction*. World Scientific, New Jersey, USA, 3rd ed., 2005.
- [57] T. DeGrand and C. Detar, *Lattice methods for quantum chromodynamics*. World Scientific, New Jersey, USA, 2006.
- [58] C. Gattringer and C. Lang, “Quantum chromodynamics on the lattice,” *Lect. Notes Phys.* **788** (2010) 1–211.
- [59] O. Philipsen, “Lattice QCD at non-zero temperature and baryon density,” [arXiv:1009.4089 \[hep-lat\]](#). Lectures at the Summer School on “Modern perspectives in lattice QCD”, Les Houches, France, 3-28 August 2009.
- [60] BMW Collaboration, S. Dürr *et al.*, “Ab-Initio Determination of Light Hadron Masses,” *Science* **322** (2008) 1224–1227, [arXiv:0906.3599 \[hep-lat\]](#).
- [61] C. Hoelbling, “Light hadron spectroscopy and pseudoscalar decay constants,” *PoS Lat2010* (2010) 011, [arXiv:1102.0410 \[hep-lat\]](#).

-
- [62] S. Capitani, “Lattice perturbation theory,” *Phys. Rept.* **382** (2003) 113–302, [arXiv:hep-lat/0211036](#) [hep-lat].
- [63] K. Symanzik, “Continuum Limit and Improved Action in Lattice Theories, 1.,2.,” *Nucl. Phys.* **B226** (1983) 187–204, 205–227.
- [64] M. Lüscher and P. Weisz, “On-Shell Improved Lattice Gauge Theories,” *Commun. Math. Phys.* **97** (1985) 59.
- [65] M. Lüscher and P. Weisz, “Computation of the Action for On-Shell Improved Lattice Gauge Theories at Weak Coupling,” *Phys. Lett.* **B158** (1985) 250.
- [66] Y. Iwasaki, “Renormalization Group Analysis of Lattice Theories and Improved Lattice Action. 1. Two-Dimensional Nonlinear O(N) Sigma Model.” UTHEP-117, 1983.
- [67] Y. Iwasaki, “Renormalization Group Analysis of Lattice Theories and Improved Lattice Action. 2. Four-Dimensional Nonabelian SU(N) Gauge Model.” UTHEP-118, 1983.
- [68] H. B. Nielsen and M. Ninomiya, “Absence of Neutrinos on a Lattice. 1. Proof by Homotopy Theory,” *Nucl. Phys.* **B185** (1981) 20.
- [69] H. B. Nielsen and M. Ninomiya, “Absence of Neutrinos on a Lattice. 2. Intuitive Topological Proof,” *Nucl. Phys.* **B193** (1981) 173.
- [70] B. Sheikholeslami and R. Wohlert, “Improved Continuum Limit Lattice Action for QCD with Wilson Fermions,” *Nucl. Phys.* **B259** (1985) 572.
- [71] R. Wohlert, “Improved Continuum Limit Lattice Action for Quarks.” DESY 87/069, 1987.
- [72] M. Lüscher, S. Sint, R. Sommer, and P. Weisz, “Chiral symmetry and O(a) improvement in lattice QCD,” *Nucl. Phys.* **B478** (1996) 365–400, [arXiv:hep-lat/9605038](#).
- [73] M. Lüscher and P. Weisz, “O(a) improvement of the axial current in lattice QCD to one-loop order of perturbation theory,” *Nucl. Phys.* **B479** (1996) 429–458, [arXiv:hep-lat/9606016](#).
- [74] S. Sint and P. Weisz, “Further results on O(a) improved lattice QCD to one-loop order of perturbation theory,” *Nucl. Phys.* **B502** (1997) 251–268, [arXiv:hep-lat/9704001](#).
- [75] **Alpha** Collaboration, K. Jansen and R. Sommer, “O(alpha) improvement of lattice QCD with two flavors of Wilson quarks,” *Nucl. Phys.* **B530** (1998) 185–203, [arXiv:hep-lat/9803017](#).
- [76] **WHOT-QCD** Collaboration, S. Ejiri *et al.*, “Scaling behavior of chiral phase transition in two-flavor QCD with improved Wilson quarks at finite density,” *PoS Lat2010* (2010) 181, [arXiv:1101.5582](#) [hep-lat].

- [77] B. Brandt, O. Philipsen, H. Wittig, and L. Zeidlewicz, “Towards the $N_f = 2$ deconfinement transition temperature with $O(a)$ improved Wilson fermions,” *PoS Lat2010* (2010) 172, [arXiv:1008.2143 \[hep-lat\]](#).
- [78] B. Brandt, O. Philipsen, H. Wittig, and L. Zeidlewicz, “Towards the $N_f=2$ deconfinement transition temperature with $O(a)$ improved Wilson fermions: An update,” [arXiv:1011.6172 \[hep-lat\]](#). To appear in the proceedings of “Quark Confinement and the Hadron Spectrum IX”, Madrid, Spain, 2010.
- [79] **QCDSF-DIK** Collaboration, V. G. Bornyakov *et al.*, “Probing the finite temperature phase transition with $N(f) = 2$ nonperturbatively improved Wilson fermions,” *Phys. Rev.* **D82** (2010) 014504, [arXiv:0910.2392 \[hep-lat\]](#).
- [80] **QCDSF-DIK** Collaboration, V. G. Bornyakov *et al.*, “Finite temperature phase transition with two flavors of improved Wilson fermions,” *PoS Lat2010* (2010) 170, [arXiv:1102.4461 \[hep-lat\]](#).
- [81] R. Frezzotti, P. A. Grassi, S. Sint, and P. Weisz, “A Local formulation of lattice QCD without unphysical fermion zero modes,” *Nucl. Phys. Proc. Suppl.* **83** (2000) 941–946, [arXiv:hep-lat/9909003 \[hep-lat\]](#).
- [82] **Alpha** Collaboration, R. Frezzotti, P. A. Grassi, S. Sint, and P. Weisz, “Lattice QCD with a chirally twisted mass term,” *JHEP* **0108** (2001) 058, [arXiv:hep-lat/0101001 \[hep-lat\]](#).
- [83] R. Frezzotti and G. C. Rossi, “Chirally improving Wilson fermions. 1. $O(a)$ improvement,” *JHEP* **0408** (2004) 007, [arXiv:hep-lat/0306014 \[hep-lat\]](#).
- [84] A. Shindler, “Twisted mass lattice QCD,” *Phys. Rept.* **461** (2008) 37–110, [arXiv:0707.4093 \[hep-lat\]](#).
- [85] R. Frezzotti, G. Martinelli, M. Papinutto, and G. C. Rossi, “Reducing cutoff effects in maximally twisted lattice QCD close to the chiral limit,” *JHEP* **0604** (2006) 038, [arXiv:hep-lat/0503034 \[hep-lat\]](#).
- [86] **ETM** Collaboration, P. Boucaud *et al.*, “Dynamical Twisted Mass Fermions with Light Quarks: Simulation and Analysis Details,” *Comput. Phys. Commun.* **179** (2008) 695–715, [arXiv:0803.0224 \[hep-lat\]](#).
- [87] **XLF** Collaboration, K. Jansen, M. Papinutto, A. Shindler, C. Urbach, and I. Wetzorke, “Quenched scaling of Wilson twisted mass fermions,” *JHEP* **09** (2005) 071, [arXiv:hep-lat/0507010](#).
- [88] **XLF** Collaboration, K. Jansen, M. Papinutto, A. Shindler, C. Urbach, and I. Wetzorke, “Light quarks with twisted mass fermions,” *Phys. Lett.* **B619** (2005) 184–191, [arXiv:hep-lat/0503031](#).
- [89] K. Jansen, M. Papinutto, A. Shindler, I. Wetzorke, and C. Urbach, “Scaling test of quenched Wilson twisted mass QCD at maximal twist,” *PoS Lat2005* (2006) 231, [arXiv:hep-lat/0509194 \[hep-lat\]](#).

-
- [90] **tmfT** Collaboration, E.-M. Ilgenfritz, O. Philipsen, L. Zeidlewicz, *et al.*, “On the phase structure of lattice QCD with twisted-mass Wilson fermions at non-zero temperature,” *PoS Lat2009* (2009) 206, [arXiv:0912.0919 \[hep-lat\]](#).
- [91] **ETM** Collaboration, C. Urbach, “Lattice QCD with two light Wilson quarks and maximally twisted mass,” *PoS Lat2007* (2007) 022, [arXiv:0710.1517 \[hep-lat\]](#).
- [92] **ETM** Collaboration, P. Dimopoulos, R. Frezzotti, C. Michael, G. C. Rossi, and C. Urbach, “ $O(a^2)$ cutoff effects in lattice Wilson fermion simulations,” *Phys. Rev. D* **81** (2010) 034509, [arXiv:0908.0451 \[hep-lat\]](#).
- [93] F. Farchioni *et al.*, “Twisted mass quarks and the phase structure of lattice QCD,” *Eur. Phys. J. C* **39** (2005) 421–433, [arXiv:hep-lat/0406039 \[hep-lat\]](#).
- [94] F. Farchioni *et al.*, “Exploring the phase structure of lattice QCD with twisted mass quarks,” *Nucl. Phys. Proc. Suppl.* **140** (2005) 240–245, [arXiv:hep-lat/0409098 \[hep-lat\]](#).
- [95] F. Farchioni *et al.*, “The Phase structure of lattice QCD with Wilson quarks and renormalization group improved gluons,” *Eur. Phys. J. C* **42** (2005) 73–87, [arXiv:hep-lat/0410031 \[hep-lat\]](#).
- [96] F. Farchioni *et al.*, “Dynamical twisted mass fermions,” *PoS Lat2005* (2006) 072, [arXiv:hep-lat/0509131 \[hep-lat\]](#).
- [97] F. Farchioni *et al.*, “Numerical simulations with two flavors of twisted-mass Wilson quarks and DBW2 gauge action,” *Eur. Phys. J. C* **47** (2006) 453–472, [arXiv:hep-lat/0512017 \[hep-lat\]](#).
- [98] F. Farchioni *et al.*, “Lattice spacing dependence of the first order phase transition for dynamical twisted mass fermions,” *Phys. Lett. B* **624** (2005) 324–333, [arXiv:hep-lat/0506025 \[hep-lat\]](#).
- [99] S. Aoki, “New Phase Structure for Lattice QCD with Wilson Fermions,” *Phys. Rev. D* **30** (1984) 2653.
- [100] S. Aoki, T. Kaneda, A. Ukawa, and T. Umemura, “Finite temperature phase structure of lattice QCD with the Wilson quark action for two and four flavors,” *Nucl. Phys. Proc. Suppl.* **53** (1997) 438–441, [arXiv:hep-lat/9612010 \[hep-lat\]](#).
- [101] S. Sharpe and R. Singleton, “Spontaneous flavor and parity breaking with Wilson fermions,” *Phys. Rev. D* **58** (1998) 074501, [arXiv:hep-lat/9804028 \[hep-lat\]](#).
- [102] G. Münster, “On the phase structure of twisted mass lattice QCD,” *JHEP* **09** (2004) 035, [arXiv:hep-lat/0407006](#).
- [103] Y. Aoki, Z. Fodor, S. D. Katz, and K. K. Szabo, “The QCD transition temperature: Results with physical masses in the continuum limit,” *Phys. Lett. B* **643** (2006) 46–54, [arXiv:hep-lat/0609068 \[hep-lat\]](#).

- [104] Y. Aoki *et al.*, “The QCD transition temperature: results with physical masses in the continuum limit II.,” *JHEP* **0906** (2009) 088, [arXiv:0903.4155 \[hep-lat\]](#).
- [105] S. Ejiri *et al.*, “On the magnetic equation of state in (2+1)-flavor QCD,” *Phys. Rev.* **D80** (2009) 094505, [arXiv:0909.5122 \[hep-lat\]](#).
- [106] **HotQCD** Collaboration, A. Bazavov and P. Petreczky, “Deconfinement and chiral transition with the highly improved staggered quark (HISQ) action,” *J. Phys. Conf. Ser.* **230** (2010) 012014, [arXiv:1005.1131 \[hep-lat\]](#).
- [107] M. Creutz, “Comments on staggered fermions / Panel discussion,” *PoS Confinement8* (2008) 016, [arXiv:0810.4526 \[hep-lat\]](#).
- [108] G. Rossi and M. Testa, “A 0-dimensional counter-example to rooting?,” *Phys. Lett.* **B688** (2010) 248–249, [arXiv:1005.3672 \[hep-lat\]](#).
- [109] **HotQCD** Collaboration, A. Bazavov and P. Petreczky, “Taste symmetry and QCD thermodynamics with improved staggered fermions,” *PoS Lat2010* (2010) 169, [arXiv:1012.1257 \[hep-lat\]](#).
- [110] P. H. Ginsparg and K. G. Wilson, “A Remnant of Chiral Symmetry on the Lattice,” *Phys. Rev.* **D25** (1982) 2649.
- [111] H. Neuberger, “Exactly massless quarks on the lattice,” *Phys. Lett.* **B417** (1998) 141–144, [arXiv:hep-lat/9707022 \[hep-lat\]](#).
- [112] H. Neuberger, “A Practical Implementation of the Overlap Dirac Operator,” *Phys. Rev. Lett.* **81** (1998) 4060–4062, [arXiv:hep-lat/9806025 \[hep-lat\]](#).
- [113] D. B. Kaplan, “A method for simulating chiral fermions on the lattice,” *Phys. Lett.* **B288** (1992) 342–347, [arXiv:hep-lat/9206013 \[hep-lat\]](#).
- [114] Y. Shamir, “Chiral fermions from lattice boundaries,” *Nucl. Phys.* **B406** (1993) 90–106, [arXiv:hep-lat/9303005](#).
- [115] P. Chen *et al.*, “The Finite temperature QCD phase transition with domain wall fermions,” *Phys. Rev.* **D64** (2001) 014503, [arXiv:hep-lat/0006010 \[hep-lat\]](#).
- [116] M. Cheng *et al.*, “The finite temperature QCD using 2 + 1 flavors of domain wall fermions at $N(t) = 8$,” *Phys. Rev.* **D81** (2010) 054510, [arXiv:0911.3450 \[hep-lat\]](#).
- [117] **JLQCD** Collaboration, Cossu *et al.*, “Light meson form factors in $N_f=2+1$ QCD with dynamical overlap quarks,” *PoS Lat2010* (2010) 146, [arXiv:1012.0137 \[hep-lat\]](#).
- [118] L. H. Karsten, “Lattice Fermions in Euclidean Space-Time,” *Phys. Lett.* **B104** (1981) 315.
- [119] F. Wilczek, “On Lattice Fermions,” *Phys. Rev. Lett.* **59** (1987) 2397.
- [120] M. Creutz, “Four-dimensional graphene and chiral fermions,” *JHEP* **04** (2008) 017, [arXiv:0712.1201 \[hep-lat\]](#).

-
- [121] A. Borici, “Creutz fermions on an orthogonal lattice,” *Phys. Rev.* **D78** (2008) 074504, [arXiv:0712.4401 \[hep-lat\]](#).
- [122] K. Cichy, J. Gonzalez Lopez, and A. Kujawa, “A comparison of the cut-off effects for Twisted Mass, Overlap and Creutz fermions at tree-level of Perturbation Theory,” *Acta Phys. Polon.* **B39** (2008) 3463, [arXiv:0811.0572 \[hep-lat\]](#).
- [123] K. Cichy, J. Gonzalez Lopez, K. Jansen, A. Kujawa, and A. Shindler, “Twisted Mass, Overlap and Creutz Fermions: Cut-off Effects at Tree-level of Perturbation Theory,” *Nucl. Phys.* **B800** (2008) 94–108, [arXiv:0802.3637 \[hep-lat\]](#).
- [124] P. F. Bedaque, M. I. Buchoff, B. C. Tiburzi, and A. Walker-Loud, “Broken Symmetries from Minimally Doubled Fermions,” *Phys. Lett.* **B662** (2008) 449–455, [arXiv:0801.3361 \[hep-lat\]](#).
- [125] S. Capitani, M. Creutz, J. Weber, and H. Wittig, “Minimally doubled fermions and their renormalization,” *PoS Lat2010* (2010) 093, [arXiv:1010.0110 \[hep-lat\]](#).
- [126] S. Capitani, M. Creutz, J. Weber, and H. Wittig, “Renormalization of minimally doubled fermions,” *JHEP* **09** (2010) 027, [arXiv:1006.2009 \[hep-lat\]](#).
- [127] S. Duane, A. D. Kennedy, J. Pendleton, and D. Roweth, “Hybrid Monte Carlo,” *Phys. Lett.* **B195** (1987) 216–222.
- [128] C. Urbach, K. Jansen, A. Shindler, and U. Wenger, “HMC algorithm with multiple time scale integration and mass preconditioning,” *Comput. Phys. Commun.* **174** (2006) 87–98, [arXiv:hep-lat/0506011 \[hep-lat\]](#).
- [129] K. Jansen and C. Urbach, “tmLQCD: A Program suite to simulate Wilson Twisted mass Lattice QCD,” *Comput. Phys. Commun.* **180** (2009) 2717–2738, [arXiv:0905.3331 \[hep-lat\]](#).
- [130] A. D. Sokal, “Monte Carlo methods in statistical mechanics: Foundations and New Algorithms,”. Lectures given at the Troisième Cycle de la Physique en Suisse Romande, Lausanne, Switzerland, June 15-29, 1989. Updated 1996.
- [131] B. A. Berg, *Introduction to Markov Chain Monte Carlo Simulations and their Statistical Analysis*. World Scientific, Singapore, 2004.
- [132] **Alpha** Collaboration, U. Wolff, “Monte Carlo errors with less errors,” *Comput. Phys. Commun.* **156** (2004) 143–153, [arXiv:hep-lat/0306017 \[hep-lat\]](#).
- [133] M. Lüscher, “Volume Dependence of the Energy Spectrum in Massive Quantum Field Theories. 1. Stable Particle States,” *Commun. Math. Phys.* **104** (1986) 177.
- [134] L. Zeidlewicz, *Gitterregularisierte QCD mit chiral verdrehtem Massenterm bei endlichen Temperaturen*. Westfälische Wilhelms-Universität Münster, 2008. Diploma thesis.
- [135] M. Creutz, “Wilson fermions at finite temperature,” [arXiv:hep-lat/9608024](#).

- [136] S. Aoki, A. Ukawa, and T. Umemura, “Finite temperature phase structure of lattice QCD with Wilson quark action,” *Phys. Rev. Lett.* **76** (1996) 873–876, [arXiv:hep-lat/9508008](#).
- [137] S. Aoki, “Phase structure of lattice QCD with Wilson fermion at finite temperature,” *Nucl. Phys. Proc. Suppl.* **60A** (1998) 206–219, [arXiv:hep-lat/9707020](#) [[hep-lat](#)].
- [138] M. Creutz, “Effective potentials, thermodynamics, and twisted mass quarks,” *Phys. Rev.* **D76** (2007) 054501, [arXiv:0706.1207](#) [[hep-lat](#)].
- [139] S. Sharpe and J. Wu, “Twisted mass chiral perturbation theory at next-to-leading order,” *Phys. Rev.* **D71** (2005) 074501, [arXiv:hep-lat/0411021](#).
- [140] **qq+q** Collaboration, F. Farchioni, I. Montvay, and E. Scholz, “Quark mass dependence of pseudoscalar masses and decay constants on a lattice,” *Eur. Phys. J.* **C37** (2004) 197–204, [arXiv:hep-lat/0403014](#).
- [141] **ETM** Collaboration, P. Boucaud *et al.*, “Dynamical twisted mass fermions with light quarks,” *Phys. Lett.* **B650** (2007) 304–311, [arXiv:hep-lat/0701012](#).
- [142] **XLF** Collaboration, K. Jansen, A. Shindler, C. Urbach, and I. Wetzorke, “Scaling test for Wilson twisted mass QCD,” *Phys. Lett.* **B586** (2004) 432–438, [arXiv:hep-lat/0312013](#).
- [143] P. Hegde, F. Karsch, E. Laermann, and S. Shcheredin, “Lattice cut-off effects and their reduction in studies of QCD thermodynamics at non-zero temperature and chemical potential,” *Eur. Phys. J.* **C55** (2008) 423–437, [arXiv:0801.4883](#) [[hep-lat](#)].
- [144] U. M. Heller, F. Karsch, and B. Sturm, “Improved staggered fermion actions for QCD thermodynamics,” *Phys. Rev.* **D60** (1999) 114502, [arXiv:hep-lat/9901010](#).
- [145] F. Karsch, E. Laermann, and A. Peikert, “The pressure in 2, 2+1 and 3 flavour QCD,” *Phys. Lett.* **B478** (2000) 447–455, [arXiv:hep-lat/0002003](#).
- [146] T. Hahn, “CUBA: A library for multidimensional numerical integration,” *Comput. Phys. Commun.* **168** (2005) 78–95, [arXiv:hep-ph/0404043](#).
- [147] J. I. Kapusta, “Quantum Chromodynamics at High Temperature,” *Nucl. Phys.* **B148** (1979) 461–498.
- [148] O. Philipsen, “Towards a determination of the chiral critical surface of QCD,” *PoS CPOD2009* (2009) 026, [arXiv:0910.0785](#) [[hep-ph](#)].
- [149] F. Karsch and E. Laermann, “Susceptibilities, the specific heat and a cumulant in two flavor QCD,” *Phys. Rev.* **D50** (1994) 6954–6962, [arXiv:hep-lat/9406008](#).
- [150] C. W. Bernard *et al.*, “Which chiral symmetry is restored in high temperature QCD?,” *Phys. Rev. Lett.* **78** (1997) 598–601, [arXiv:hep-lat/9611031](#).

-
- [151] Y. Iwasaki, K. Kanaya, S. Kaya, and T. Yoshie, “Scaling of chiral order parameter in two-flavor QCD,” *Phys. Rev. Lett.* **78** (1997) 179–182, [arXiv:hep-lat/9609022](#).
- [152] **JLQCD** Collaboration, S. Aoki *et al.*, “Scaling study of the two-flavor chiral phase transition with the Kogut-Susskind quark action in lattice QCD,” *Phys. Rev.* **D57** (1998) 3910–3922, [arXiv:hep-lat/9710048](#).
- [153] **CP-PACS** Collaboration, A. Ali Khan *et al.*, “Phase structure and critical temperature of two flavor QCD with renormalization group improved gauge action and clover improved Wilson quark action,” *Phys. Rev.* **D63** (2001) 034502, [arXiv:hep-lat/0008011](#).
- [154] M. D’Elia, A. Di Giacomo, and C. Pica, “Two flavor QCD and confinement,” *Phys. Rev.* **D72** (2005) 114510, [arXiv:hep-lat/0503030](#).
- [155] G. Cossu, M. D’Elia, A. Di Giacomo, and C. Pica, “Two flavor QCD and confinement - II,” [arXiv:0706.4470 \[hep-lat\]](#).
- [156] C. Bonati, G. Cossu, M. D’Elia, A. Di Giacomo, and C. Pica, “A test of first order scaling in $N_f = 2$ QCD: a progress report,” *PoS Lat2008* (2008) 204, [arXiv:0901.3231 \[hep-lat\]](#).
- [157] F. Parisen Toldin, A. Pelissetto, and E. Vicari, “The 3-D $O(4)$ universality class and the phase transition in two-flavor QCD,” *JHEP* **07** (2003) 029, [arXiv:hep-ph/0305264](#).
- [158] F. Burger, O. Philipsen, L. Zeidlewicz, *et al.*, “The thermal QCD transition with two flavours of twisted mass fermions,” [arXiv:1102.4530 \[hep-lat\]](#).
- [159] M. E. Fisher, “The Theory of Equilibrium Critical Phenomena,” *Rep. Prog. Phys.* **30** (1967) 615.
- [160] A. Pelissetto and E. Vicari, “Critical phenomena and renormalization group theory,” *Phys.Rept.* **368** (2002) 549–727, [arXiv:cond-mat/0012164 \[cond-mat\]](#).
- [161] F. Karsch, “Scaling of pseudocritical couplings in two flavor QCD,” *Phys. Rev.* **D49** (1994) 3791–3794, [arXiv:hep-lat/9309022 \[hep-lat\]](#).
- [162] K. Kanaya and S. Kaya, “Critical exponents of a three dimensional $O(4)$ spin model,” *Phys. Rev.* **D51** (1995) 2404–2410, [arXiv:hep-lat/9409001 \[hep-lat\]](#).
- [163] F. Schwabl, *Statistische Mechanik*. Springer, Berlin, 2nd ed., 2004.
- [164] D. Toussaint, “Scaling functions for $O(4)$ in three dimensions,” *Phys. Rev.* **D55** (1997) 362–366, [arXiv:hep-lat/9607084](#).
- [165] J. Engels and T. Mendes, “Goldstone-mode effects and scaling function for the three-dimensional $O(4)$ model,” *Nucl. Phys.* **B572** (2000) 289–304, [arXiv:hep-lat/9911028](#).
- [166] M. E. Fisher and A. N. Berker, “Scaling for first-order transitions in thermodynamic and finite systems,” *Phys. Rev.* **B26** (1982) 2507–2513.

- [167] C. DeTar, “QCD Thermodynamics on the Lattice: Recent Results,” [arXiv:1101.0208](https://arxiv.org/abs/1101.0208) [hep-lat]. To appear in Proceedings of the Kyoto workshop on Thermal Quantum Field Theory and its Application, August 28-30, 2010, Soryushiron Kenkyu (Study of Particle Theory).
- [168] L. D. McLerran and B. Svetitsky, “Quark Liberation at High Temperature: A Monte Carlo Study of SU(2) Gauge Theory,” *Phys. Rev.* **D24** (1981) 450.
- [169] T. Williams, C. Kelley, *et al.*, “gnuplot 4.4. An Interactive Plotting Program.” <http://www.gnuplot.info>, 2010.
- [170] W. Press, S. Teukolsky, W. Vetterling, and B. Flannery, *Numerical Recipes. The Art of Scientific Computing*. Cambridge University Press, Cambridge, UK, third ed., 2007.
- [171] M. Cheng *et al.*, “The transition temperature in QCD,” *Phys. Rev.* **D74** (2006) 054507, [arXiv:hep-lat/0608013](https://arxiv.org/abs/hep-lat/0608013).
- [172] S. Chandrasekharan and A. C. Mehta, “Effects of the anomaly on the two-flavor QCD chiral phase transition,” *Phys. Rev. Lett.* **99** (2007) 142004, [arXiv:0705.0617](https://arxiv.org/abs/0705.0617) [hep-lat].
- [173] G. V. Dunne and A. Kovner, “ $U_A(1)$ Anomaly at high temperature: the scalar-pseudoscalar splitting in QCD,” *Phys. Rev.* **D82** (2010) 065014, [arXiv:1004.1075](https://arxiv.org/abs/1004.1075) [hep-ph].
- [174] P. Vranas, “The finite temperature QCD phase transition with domain wall fermions,” *Nucl. Phys. Proc. Suppl.* **83** (2000) 414–416, [arXiv:hep-lat/9911002](https://arxiv.org/abs/hep-lat/9911002).
- [175] R. Gavai, S. Gupta, and R. Lacaze, “Quenched QCD at finite temperature with chiral fermions,” *Phys. Rev.* **D65** (2002) 094504, [arXiv:hep-lat/0107022](https://arxiv.org/abs/hep-lat/0107022).
- [176] C. DeTar and J. Kogut, “The Hadronic Spectrum of the Quark Plasma,” *Phys. Rev. Lett.* **59** (1987) 399.
- [177] S. Wissel, E. Laermann, S. Shcheredin, S. Datta, and F. Karsch, “Meson correlation functions at high temperatures,” *PoS Lat2005* (2006) 164, [arXiv:hep-lat/0510031](https://arxiv.org/abs/hep-lat/0510031).
- [178] **RBC-Bielefeld** Collaboration, S. Mukherjee, “Screening masses of mesons in 2+1 flavour QCD,” *PoS Lat2007* (2007) 210, [arXiv:0710.0963](https://arxiv.org/abs/0710.0963) [hep-lat].
- [179] S. Mukherjee, “Screening of light mesons and charmonia at high temperature,” *Nucl. Phys.* **A820** (2009) 283c–286c, [arXiv:0810.2906](https://arxiv.org/abs/0810.2906) [hep-lat].
- [180] M. Cheng *et al.*, “Meson screening masses from lattice QCD with two light and the strange quark,” *Eur. Phys. J.* **C71** (2010) 1564, [arXiv:1010.1216](https://arxiv.org/abs/1010.1216) [hep-lat].
- [181] D. Banerjee, R. Gavai, and S. Gupta, “The scalar does not decay at finite temperatures,” *PoS Lat2010* (2010) 168, [arXiv:1011.0310](https://arxiv.org/abs/1011.0310) [hep-lat].

-
- [182] D. Banerjee, R. Gavai, and S. Gupta, “Quasi-static probes of the QCD plasma,” [arXiv:1102.4465 \[hep-lat\]](#).
- [183] V. L. Eletsky and B. L. Ioffe, “On Temperature Dependence of Correlators of Hadronic Currents,” *Sov. J. Nucl. Phys.* **48** (1988) 384.
- [184] W. Florkowski and B. L. Friman, “Spatial dependence of the finite temperature meson correlation function,” *Z. Phys.* **A347** (1994) 271–276.
- [185] M. Laine and M. Vepsalainen, “Mesonic correlation lengths in high-temperature QCD,” *JHEP* **02** (2004) 004, [arXiv:hep-ph/0311268](#).
- [186] W. M. Alberico, A. Beraudo, A. Czerska, P. Czerski, and A. Molinari, “Meson screening masses in the interacting QCD plasma,” *Nucl. Phys.* **A792** (2007) 152–169, [arXiv:hep-ph/0703298](#).
- [187] S. Chandrasekharan *et al.*, “Anomalous chiral symmetry breaking above the QCD phase transition,” *Phys. Rev. Lett.* **82** (1999) 2463–2466, [arXiv:hep-lat/9807018](#).
- [188] **Wuppertal-Budapest** Collaboration, S. Borsanyi *et al.*, “The QCD equation of state with dynamical quarks,” *JHEP* **11** (2010) 077, [arXiv:1007.2580 \[hep-lat\]](#).
- [189] R. Frezzotti and G. C. Rossi, “Twisted mass lattice QCD with mass nondegenerate quarks,” *Nucl. Phys. Proc. Suppl.* **128** (2004) 193–202, [arXiv:hep-lat/0311008 \[hep-lat\]](#).
- [190] T. Chiarappa *et al.*, “Numerical simulation of QCD with u, d, s and c quarks in the twisted-mass Wilson formulation,” *Eur. Phys. J.* **C50** (2007) 373–383, [arXiv:hep-lat/0606011 \[hep-lat\]](#).
- [191] **ETM** Collaboration, R. Baron *et al.*, “Light hadrons from $N_f=2+1+1$ dynamical twisted mass fermions,” *PoS Lat2010* (2010) 123, [arXiv:1101.0518 \[hep-lat\]](#).
- [192] K. Cichy and E. V. Luschevskaya, “ $N_f = 2 + 1 + 1$ flavours of twisted mass quarks: cut-off effects at tree-level of perturbation theory,” [arXiv:1012.5047 \[hep-lat\]](#).
- [193] O. Kaczmarek *et al.*, “Phase boundary for the chiral transition in $(2+1)$ -flavor QCD at small values of the chemical potential,” *Phys. Rev.* **D83** (2011) 014504, [arXiv:1011.3130 \[hep-lat\]](#).
- [194] P. Kaste and H. J. Rothe, “Lattice artifacts in the non-Abelian Debye screening mass in one loop order,” *Phys. Rev.* **D56** (1997) 6804–6815, [arXiv:hep-lat/9704014 \[hep-lat\]](#).

Danksagung

„No book is written in a vacuum.“

Der obenstehende Satz leitet das Vorwort von Th. DeGrand und C. DeTar zu ihrem Buch über Gitter-QCD [57] ein und ist natürlich umso wahrer für eine Arbeit, die sich mit QCD bei endlichen Temperaturen beschäftigt. Deshalb unternehme ich hier den Versuch, all jenen für ihre Unterstützung zu danken, die mich während der letzten Jahre begleitet haben und ohne die mein Arbeitsalltag aber auch meine Arbeit selbst sicherlich andere gewesen wären.

An erster Stelle ist ohne Zweifel Owe Philipsen zu nennen, bei dem ich diese Arbeit durchführen konnte und bei dem ich mich für die jahrelange Betreuung hiermit herzlich bedanke. Viele anregende Diskussionen haben diese Arbeit entscheidend geformt. Darüberhinaus möchte ich die Mitglieder unserer „twisted mass finite temperature“ Kollaboration nennen, die insbesondere in unseren Kollaborationsbesprechungen¹ durch ihre Vielzahl an Diskussionsbeiträgen zur Verbesserung meiner Arbeit beigetragen haben. Hervorheben möchte ich ganz besonders Maria Paola Lombardo, die immer mit besonders viel Geduld auf meine Fragen eingegangen ist, *grazie mille per il paziente aiuto e i molti preziosi consigli*.

Den Entwurf dieser Arbeit in verschiedenen Stufen, bzw. Teile davon, haben dankenswerter Weise Basti Brandt, Nina Gausmann, Janine Hütig, Steo Lottini, Christopher Pinke und Anja Teuber gelesen. Vielen Dank für die Korrekturen und Anregungen. Alle verbleibenden Tippfehler und eventuelle Ungenauigkeiten habe ich natürlich erst nach Eurer Korrektur verschuldet.

Der gesamten Arbeitsgruppe Philipsen — zuerst in Münster, später in Frankfurt — danke ich für die beständig gute Atmosphäre, die immer ein angenehmes und zugleich produktives Arbeiten ermöglicht hat. Anja Teuber und Janine Hütig danke ich für die gemeinsamen Bürozeiten. Anja schulde ich große Anerkennung, weil sie mir zuliebe sogar bisweilen Kaffee getrunken hat. Dankeschön auch an Janines immer gut gefüllte Keksdose. Basti Brandt danke ich als virtuellem weiteren Büro-Kollegen², insbesondere für die sehr vielen gewinnbringenden Diskussionen.

Christopher Pinke und Steo Lottini danke ich dafür, dass ich in Frankfurt nicht alleine wohnen musste. Es war sehr angenehm mit Euch. *In particolare, grazie Steo per la cucina italiana*.

Zu guter Letzt bleibt, meiner Familie Dank auszusprechen, obgleich das kaum angemessen möglich ist. Eure Unterstützung kann ich gar nicht hoch genug bewerten. Das letzte Dankeschön gebührt Julia, die immer für mich da ist und entscheidend dazu beigetragen hat, dass ich alle Probleme und Hindernisse habe überwinden können.

¹Insofern danke ich natürlich auch Skype.

²Und damit danke ich ICQ und wiederum Skype...

Lebenslauf

Dipl.-Phys. Lars Zeidlewicz

14. April 2011

Cheruskerring 91
48147 Münster

zeidlewicz@th.physik.uni-frankfurt.de
0251/2877372

Persönliche Angaben

Geburtsdatum 5. November 1982
Geburtsort Rheine

Familienstand ledig

Promotionsstudium

seit 04/2008 Promotionsarbeit bei Professor Dr. O. Philipsen

05/2010-05/2011 Wissenschaftlicher Mitarbeiter am
Institut für Theoretische Physik
Goethe-Universität Frankfurt

06/2008-04/2010 Wissenschaftlicher Mitarbeiter am
Institut für Theoretische Physik
Westfälische Wilhelms-Universität Münster

04/2008 - 05/2008 Wissenschaftliche Hilfskraft am
Institut für Theoretische Physik
Westfälische Wilhelms-Universität Münster

Diplomstudium

- 10/2002-02/2008 Studium der Physik an der
Westfälischen Wilhelms-Universität Münster
- 02/2008 Erwerb des Diploms in Physik
- Wahlfächer: Kern- und Teilchenphysik
Nichtlineare Physik
- Note: mit Auszeichnung (1,0)
- Diplomarbeit zum Thema:
Gitterregularisierte QCD mit chiral verdrehtem Massenterm
bei endlichen Temperaturen
Betreuer: Professor Dr. O. Philipsen
- 10/2005 - 02/2008 Studentische Hilfskraft am
Institut für Theoretische Physik
(Übungsgruppenbetreuung)
- 10/2004 Vordiplom Physik
Note: sehr gut (1,5)

Schulzeit

- 1993-2002 Arnold-Janssen-Gymnasium
48485 Neuenkirchen
- 06/2002 Abitur mit Note 1,0
- 08/1999-11/1999 Gastschüleraufenthalt in Kanada (Windsor, ON)
- 1989-1993 Canisius-Grundschule
48429 Rheine